



Faculté des Sciences  
Institut de Physique des Hautes Energies

# Determination of the Flavour of Beauty Mesons in LHCb and Contribution to the Development of the LHCb Vertex Locator

Thèse de Doctorat

présentée à la Faculté des Sciences  
de l'Université de Lausanne  
pour l'obtention du grade de docteur ès sciences

par

**Olivier Dormond**

Physicien diplômé de l'Université de Lausanne

Jury

Prof. François Marillier, président du jury  
Prof. Aurelio Bay, directeur de thèse  
Prof. Olivier Schneider, expert interne  
Dr. Paula Collins, expert externe

Lausanne, 2003

# Imprimatur

Vu le rapport présenté par le jury d'examen, composé de

Président	Monsieur Prof.	François <b>Marillier</b>
Directeur de thèse	Monsieur Prof.	Aurélio <b>Bay</b>
Rapporteur		
Experts	Monsieur Prof.	Olivier <b>Schneider</b>
	Madame Dr	Paula <b>Collins</b>

le Conseil de Faculté autorise l'impression de la thèse de

**Monsieur Olivier Dormond**

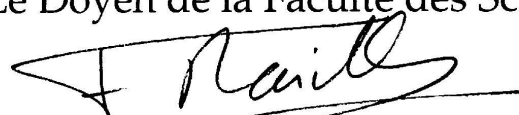
Physicien diplômé de l'Université de Lausanne

intitulée

**Determination of the Flavour of Beauty Mesons in LHCb  
and Contribution to the Development  
of the LHCb Vertex Locator**

Lausanne, le 22 décembre 2003

pour Le Doyen de la Faculté des Sciences

  
Prof. François Marillier

# Abstract

The LHC accelerator currently under construction at CERN near Geneva will accommodate the LHCb experiment by 2007. LHCb is a single-arm spectrometer designed to make precise measurement of CP violation and rare decays in the b quark sector.

CP violation arises in the Standard Model via the complex phase of the  $3 \times 3$  CKM quark mixing matrix. The unitarity of this matrix will be tested by measuring in several theoretically unrelated ways all angles and all sides of the unitary triangles. These measurements will over-constrain the model and perhaps point out inconsistencies, which could show the way to a more complete model beyond the Standard Model.

The weak interaction, which is responsible for the decay of the b quarks, allows the neutral B mesons to oscillate between B (particle) and  $\bar{B}$  (antiparticle) states. Some of the measurements of the unitary triangles rely on asymmetries between the decay rate of the B and  $\bar{B}$  mesons. For some of these measurements it is crucial to know whether the particle was produced as a B or  $\bar{B}$ .

This thesis presents the techniques used to take this decision, which is called “tagging”. The fact that quarks are always produced together with their own anti-quarks is used to select a particle coming from the decay of the other b/ $\bar{b}$  quark. In the case of  $B_s$  mesons the other  $\bar{s}/s$  quark itself can also be recovered in a charged kaon close to the  $B_s$  meson and used as a signature.

A tagging power of  $6.2 \pm 0.7\%$  is obtained for the  $B_s$  mesons while it reaches  $4.1 \pm 0.6\%$  for the  $B_d$  mesons. Some channel dependencies are observed which are caused by the acceptance and the selection cuts of the signal B, which is correlated to the tagging b, as well as the trigger. The effect of multiple p p interactions was observed and reduces the tagging power by 10% on average.

In addition to the identification of the flavour of B mesons, a precise measurement of their point of production and decay is required. The Vertex Locator is a sub-detector of LHCb dedicated to these measurements.

The second part of this thesis present a summary of the results obtained during several beam tests of LHCb Vertex Locator’s prototypes. The characterisation of

the beam telescope is followed by the description of the testbeam in which it was used.

During these tests, the successful operation of LHC speed electronics was obtained with satisfactory signal shape as well as signal-to-noise ratio. Different silicon sensor technologies were tested to evaluate their efficiency and operational conditions after irradiation, leading to the choice of *n-on-n* silicon sensors for LHCb's VELO detector.

# Résumé

L'accélérateur LHC en cours de construction au CERN près de Genève, accueillera l'expérience LHCb d'ici 2007. LHCb est un spectromètre à bras unique conçu pour réaliser des mesures précises de la violation de CP et des désintégrations rares dans le secteur du quark b.

La violation de CP s'exprime dans le Modèle Standard par la matrice  $3 \times 3$ , de mélange des quarks, CKM, qui possède une phase complexe. L'unitarité de cette matrice sera testée en mesurant, par des méthodes théoriquement indépendantes, tous les angles et tous les côtés des triangles unitaires. Ces mesures surcontraindront le modèle et permettront peut-être d'exhiber des incohérences qui pourraient montrer le chemin vers un modèle plus complet, au delà du Modèle Standard.

L'interaction faible, qui est responsable de la désintégration des quarks b, autorise les mésons B neutres à osciller entre particule et anti-particule. Certaines mesures des triangles unitaires reposent sur l'asymétrie entre le taux de désintégration des mésons B et  $\bar{B}$ . Pour plusieurs de ces mesures, il est indispensable de savoir si la particule fut produite en tant que B ou  $\bar{B}$ .

Cette thèse présente les techniques utilisées pour prendre cette décision, que l'on nomme "marquage". Le fait que les quarks soit toujours produits avec leur propre antiparticule est utilisé afin de sélectionner une signature provenant de la désintégration de l'autre quark b/ $\bar{b}$ . Dans le cas des mésons  $B_s$ , l'autre quark  $\bar{s}/s$  lui-même peut aussi être retrouvé dans un kaon chargé proche du méson B et être utilisé en tant que signature.

Une puissance statistique de marquage de  $6.2 \pm 0.7\%$  est obtenue pour les mésons  $B_s$  tandis qu'elle atteint  $4.1 \pm 0.6\%$  pour les mésons  $B_d$ . Quelques dépendances envers les canaux de désintégration sont observées. Elles sont produites par l'acceptance et les coupures de sélection du B qui constitue le signal, qui est corrélé au quark b utilisé pour le marquage, aussi bien que par le système de déclenchement. L'effet des interactions multiples fut observé et il réduit la puissance de marquage de 10% en moyenne.

En plus de l'identification de la saveur des mésons B, une mesure précise de leur points de production et de désintégration est requise. Le détecteur de Vertex

(VELO) est un sous-détecteur de LHCb dédié à ces mesures.

La deuxième partie de cette thèse présente un résumé des résultats obtenus durant plusieurs faisceaux tests des prototypes de détecteur de Vertex d'LHCb. La caractérisation du télescope de faisceau est suivie de la description des faisceaux tests dans lesquels il fut utilisé

Durant ces tests, il fut possible de faire fonctionner avec succès de l'électronique satisfaisant à la vitesse requise pour le LHC et d'obtenir avec satisfaction la forme du signal ainsi que le rapport signal sur bruit. Différentes technologies de senseur en silicium furent testées afin d'évaluer leur efficacité et leurs conditions opérationnelles après irradiation, conduisant au choix de senseurs en silicium de type  $n$ -sur- $n$  pour le détecteur VELO d'LHCb.

# Résumé destiné à un large public

La physique des hautes énergies a pour but l'étude des constituants fondamentaux de la matière et de leurs interactions. L'étude des lois les plus fondamentales permet la compréhension de phénomènes plus complexes dans d'autres domaines de la physique ou d'autres sciences. Cela rend possible des applications impensables auparavant.

L'essentiel des lois de la physique découlent de quatre forces fondamentales que sont la gravitation, la force électromagnétique et les forces nucléaires forte et faible. Seules les deux premières ont des effets à l'échelle macroscopique, mais toutes contribuent à l'équilibre de la matière et donc à la vie. La physique des hautes énergies permet d'observer ces forces séparément. Les physiciens les étudient en produisant des collisions de particules fondamentales à très haute énergie, par exemple de protons au futur accélérateur LHC au CERN.

Les résultats de ces expériences sont comparés à une théorie des interactions des particules appelée "Modèle Standard". Celle-ci décrit toutes les particules connues et toutes les forces à l'exception de la gravitation. La théorie est donc incomplète. Un des buts du LHC est de trouver des pistes pour la compléter, par exemple par une théorie plus large qui prédirait à haute énergie d'autres résultats que le Modèle Standard ; différences qu'il s'agira de mettre en évidence.

L'expérience LHCb, en préparation au LHC, concentre son étude sur les différences entre la matière et l'antimatière. Cette dernière est une sorte de négatif de la matière ayant (presque) les mêmes propriétés, mais toutes les charges électriques opposées. Pour ce faire, LHCb étudie une particule appelée méson B. Les désintégrations de cette particule sont dues à la force faible et sont très sensibles à la légère différence entre la matière et l'antimatière. Cette différence, appelée violation CP, est un des phénomènes physiques les plus mal compris à ce jour. Elle explique en partie comment la matière a pris le dessus sur l'antimatière aux tout premiers instants de la formation de l'univers.

Au sein de ce travail de thèse, nous avons développé plusieurs techniques permettant de distinguer un méson B de son antiparticule, le méson  $\bar{B}$ . Cette distinction est nécessaire à l'étude de la violation CP. Nous avons aussi participé au développement d'un détecteur de particules constitué de silicium, qui sera une partie du détecteur d'LHCb.





# Remerciements

J'aimerais remercier le Professeur Aurelio Bay de m'avoir permis de réaliser une thèse au sein de l'Institut de Physique des Hautes Énergie de l'Université de Lausanne. Bien que ses rôles de directeur d'institut et de vice-doyen de la Faculté des Sciences lui aient pris beaucoup de temps, il a toujours su me remettre sur le droit chemin lorsque je me laissais aller à mon passe-temps favori, l'informatique.

Je tiens aussi à remercier grandement le Professeur Olivier Schneider qui m'a accompagné durant tout mon travail sur le tagging. J'espère parvenir un jour à comprendre comment il est parvenu à passer autant de temps dans mon bureau malgré un agenda aussi chargé. De même, sa précision et sa perspicacité m'étonneront toujours.

Un grand merci aussi à madame le Docteur Paula Collins avec qui le travail fut des plus agréables. C'est avec le plus grand des plaisirs que j'ai participé à ces quelques testbeams, malgré le stress que peut engendrer le fait d'avoir autant de choses à faire en si peu de temps.

J'aimerais aussi remercier toute l'équipe du VELO ainsi que l'équipe de l'atelier du BSP tout comme les électroniciens du 5ème étage. En particulier: Jan Buytaert, Hans Dijkstra, Raymond Frei, Chris Parkes, Thomas Ruf et David Steele.

Merci aussi à tous les membres de l'IPHE et spécialement aux amateurs d'informatique : Hubert Degaudenzi et Christian Jacoby. Merci également à Erika Lüthi et Monique Romaniszin ainsi qu'à Marianne Chave qui contribuent très largement au bon fonctionnement et à la merveilleuse ambiance de l'institut.

Un grand merci à Patrick Koppenburg qui m'as bien souvent inspiré lors de la réalisation de ce document. Je ne sais combien de temps il m'aurait fallu sans sa thèse à portée de main.

Un immense merci à mon collègue et néanmoins ami, Frédéric Ronga, avec qui j'ai passé ces dix dernières années à étudier la physique et qui m'a supporté dans notre bureau commun. Merci également à Laurent Locatelli qui m'a tenu compagnie alors que Frédéric m'avait abandonné pour le Japon.

J'aimerais aussi remercier toute l'IMA Connection pour l'ambiance de midi, les éprouvantes parties de détente ainsi que tous ces apéros! En particulier : Gregely, Arigo, Allal et les Bordures.

Enfin, merci beaucoup à mes parents et à ma soeur qui mon soutenu durant toutes ces années. Merci aussi à Tania qui me supporte depuis un bon moment et qui a survécu à cette fin de thèse.

# Contents

<b>Abstract</b>	<b>I</b>
<b>Résumé</b>	<b>III</b>
<b>Résumé destiné à un large public</b>	<b>V</b>
<b>Remerciements</b>	<b>VII</b>
<b>1 Introduction</b>	<b>1</b>
1.1 Fundamental Physics . . . . .	1
1.2 Particles . . . . .	2
1.2.1 The atom . . . . .	2
1.2.2 The nucleus . . . . .	3
1.2.3 The quarks . . . . .	3
1.2.4 The fundamental particles . . . . .	4
1.2.5 Matter . . . . .	5
1.2.6 Anti-matter . . . . .	5
1.2.7 The mesons . . . . .	6
1.3 Interactions . . . . .	6
1.3.1 Gravity . . . . .	7
1.3.2 Electromagnetism . . . . .	7
1.3.3 Strong force . . . . .	8
1.3.4 Weak force . . . . .	9
1.4 The Standard Model and beyond . . . . .	10
1.5 Symmetries . . . . .	11
1.5.1 P parity transformation . . . . .	11
1.5.2 C charge conjugation . . . . .	12
1.5.3 CP symmetry . . . . .	12
1.6 Flavour tagging . . . . .	13
1.7 CERN and the LHC accelerator . . . . .	13
1.8 The LHCb experiment . . . . .	15

1.8.1	An example of detector, the Vertex Locator of LHCb . . . . .	15
1.8.2	Description of the LHCb experiment . . . . .	16
1.8.3	Trigger and data acquisition . . . . .	17
1.8.4	Simulations . . . . .	17
<b>2</b>	<b>Theoretical Overview</b>	<b>19</b>
2.1	The Standard Model . . . . .	20
2.1.1	Leptonic Electroweak Standard Model . . . . .	20
2.1.2	Hadronic extension . . . . .	23
2.1.3	The quark couplings . . . . .	23
2.2	CP violation . . . . .	25
2.2.1	CKM matrix and unitary triangles . . . . .	26
2.2.2	Measurements of the unitary triangles . . . . .	26
2.2.3	CP phenomenology . . . . .	27
2.3	Flavour tagging . . . . .	31
<b>3</b>	<b>The LHCb Experiment</b>	<b>33</b>
3.1	Large Hadron Collider . . . . .	33
3.1.1	Protons beams and their collisions . . . . .	34
3.1.2	b quarks and the LHC . . . . .	35
3.2	The LHCb detector . . . . .	36
3.2.1	The VELO . . . . .	37
3.2.2	The RICH . . . . .	40
3.2.3	The magnet . . . . .	40
3.2.4	The tracker . . . . .	41
3.2.5	The calorimeters . . . . .	43
3.2.6	The muon detector . . . . .	44
3.3	The LHCb trigger . . . . .	44
3.4	Monte Carlo and analysis programme . . . . .	46
3.4.1	Generation & simulation . . . . .	48
3.4.2	Reconstruction & analysis . . . . .	48
<b>4</b>	<b>Flavour tagging</b>	<b>51</b>
4.1	Flavour tagging signatures . . . . .	52
4.2	Tagging power characterisation . . . . .	53
4.3	Limiting factors . . . . .	54
4.4	Tagger selection criteria . . . . .	56
4.4.1	Particle identification . . . . .	57
4.4.2	Opposite-side muon tagger . . . . .	58
4.4.3	Opposite-side electron tagger . . . . .	60
4.4.4	Opposite-side kaon tagger . . . . .	62

4.4.5	Opposite-side vertex charge . . . . .	64
4.4.6	Same-side kaon tagger . . . . .	65
4.4.7	Multiple tags selection . . . . .	65
4.5	Triggers effects . . . . .	66
4.5.1	Effects of the triggers on the muon tagging . . . . .	67
4.5.2	Effects of the triggers on the electron tagging . . . . .	68
4.5.3	Effects of the triggers on the opposite-side kaon tagging . . . . .	68
4.5.4	Effects of the triggers on the vertex charge tagging . . . . .	69
4.5.5	Global effects of the triggers . . . . .	69
4.6	Multiple interactions . . . . .	70
4.7	Dependency on specific decay channels . . . . .	72
4.8	The flavour tagging software . . . . .	73
4.8.1	Inside look . . . . .	74
4.8.2	Flavour tags . . . . .	75
4.9	Future . . . . .	76
<b>5</b>	<b>Contribution to the VELO</b>	<b>77</b>
5.1	VELO telescope characterisation . . . . .	78
5.1.1	The VELO telescope . . . . .	78
5.1.2	Efficiency measurement . . . . .	79
5.1.3	Resolution measurements . . . . .	79
5.1.4	Measurement of charge sharing . . . . .	82
5.2	Experimental set-up . . . . .	83
5.2.1	Data acquisition system . . . . .	84
5.2.2	The SCT128A read-out chip . . . . .	87
5.2.3	Testbeam event reconstruction . . . . .	89
5.3	SCT128A signal shape study . . . . .	91
5.4	Performance of irradiated sensors . . . . .	94
5.4.1	Sensors description . . . . .	95
5.4.2	Performance measurements . . . . .	98
	<b>Conclusion</b>	<b>105</b>
	<b>A Statistical error on <math>\epsilon_{\text{eff}}</math></b>	<b>107</b>



# List of Figures

1.1	Representation of the atom . . . . .	2
1.2	The nucleus is made of protons and neutrons, which are themselves made of the “up” and “down” quarks [1]. . . . .	3
1.3	Two corks interacting through the water surface coupling. . . . .	8
1.4	The site of the LHC near Geneva . . . . .	14
1.5	Side view of the LHCb detector. Figure from [2]. . . . .	16
2.1	Feymann diagram of the interaction between a quark and a W. . . . .	25
2.2	The main unitary triangle, corresponding to relation 2.24. . . . .	27
2.3	The unitary triangle corresponding to relation 2.25. . . . .	27
3.1	The CERN accelerators facility. . . . .	33
3.2	Section view of the LHC beam pipe. . . . .	34
3.3	Polar distribution of the b- and $\bar{b}$ -hadrons at LHC. . . . .	35
3.4	Side view of the LHCb detector in its latest “light” design. . . . .	36
3.5	3D view of the VELO TDR prototype with 25 stations. . . . .	38
3.6	Cross-section view of the VELO TDR design along the beam axis. . . . .	39
3.7	Schematic view of the $\phi$ and $r$ silicon sensors . . . . .	39
3.8	The LHCb magnet. . . . .	40
3.9	The TT tracking station . . . . .	41
3.10	Front view of an opened tracking station showing the beam pipe in the middle, the inner tracker boxes and then the outer tracker straw tubes on the outside. . . . .	42
3.11	Side view of the muon detector. . . . .	44
3.12	Block diagram of the structure of LHCb’s software. . . . .	47
4.1	Opposite side tagging signatures. Explanations in the text. . . . .	52
4.2	Example of the production mechanism of a same-side tagging signature. . . . .	52

4.3	Log-likelihood distributions for the tagging candidates (muons, electron and kaons, from top to bottom) in reconstructed $B_s^0 \rightarrow D_s^\mp K^\pm$ events. . . . .	57
4.4	Momentum distribution of the true muons in $B_s^0 \rightarrow K^+ K^-$ events from different sources (normalised areas). . . . .	59
4.5	Transverse momentum distribution of the true muons in $B_s^0 \rightarrow K^+ K^-$ events from different sources (normalised areas). . . . .	59
4.6	IP/ $\sigma_{IP}$ distribution of the reconstructed muons in $B_s^0 \rightarrow K^+ K^-$ events from different sources (normalised to the number of generated muons). . . . .	59
4.7	Momentum vs transverse momentum distribution of the true muons in $B_s^0 \rightarrow K^+ K^-$ events (light: $b \rightarrow \mu$ ; dark: $b \rightarrow c \rightarrow \mu$ ). . . . .	59
4.8	$\epsilon_{\text{eff}}$ for muon tagger as a function of the momentum cut for reconstructed and triggered $B_s^0 \rightarrow K^+ K^-$ . . . . .	60
4.9	$\epsilon_{\text{eff}}$ for muon tagger as a function of the transverse momentum cut for reconstructed and triggered $B_s^0 \rightarrow K^+ K^-$ . . . . .	60
4.10	$\epsilon_{\text{eff}}$ for muon tagger as a function of the IP/ $\sigma_{IP}$ cut for reconstructed and triggered $B_s^0 \rightarrow K^+ K^-$ . . . . .	60
4.11	Momentum distribution of the true electrons in $B_s^0 \rightarrow K^+ K^-$ events from different sources (normalised areas). . . . .	61
4.12	Transverse momentum distribution of the true electrons in $B_s^0 \rightarrow K^+ K^-$ events from different sources (normalised areas). . . . .	61
4.13	IP/ $\sigma_{IP}$ distribution of the reconstructed electrons in $B_s^0 \rightarrow K^+ K^-$ events from different sources (normalised to the number of generated electrons). . . . .	61
4.14	Momentum vs transverse momentum distribution of the true electrons in $B_s^0 \rightarrow K^+ K^-$ events (light: $b \rightarrow e$ ; dark: $b \rightarrow c \rightarrow e$ ). . . . .	61
4.15	$\epsilon_{\text{eff}}$ for electron tagger as a function of the momentum cut for reconstructed and triggered $B_s^0 \rightarrow K^+ K^-$ . . . . .	62
4.16	$\epsilon_{\text{eff}}$ for electron tagger as a function of the transverse momentum cut for reconstructed and triggered $B_s^0 \rightarrow K^+ K^-$ . . . . .	62
4.17	$\epsilon_{\text{eff}}$ for electron tagger as a function of the IP/ $\sigma_{IP}$ cut for reconstructed and triggered $B_s^0 \rightarrow K^+ K^-$ . . . . .	62
4.18	Momentum distribution of the true kaons in $B_s^0 \rightarrow K^+ K^-$ events from different sources (normalised areas). . . . .	63
4.19	Transverse momentum distribution of the true kaons in $B_s^0 \rightarrow K^+ K^-$ events from different sources (normalised areas). . . . .	63
4.20	IP/ $\sigma_{IP}$ distribution of the reconstructed kaons in $B_s^0 \rightarrow K^+ K^-$ events from different sources (normalised to the number of generated kaons). . . . .	63



4.21	$\epsilon_{\text{eff}}$ for opposite-side kaon tagger as a function of the momentum cut for reconstructed and triggered $B_s^0 \rightarrow K^+ K^-$ . . . . .	63
4.22	$\epsilon_{\text{eff}}$ for opposite-side kaon tagger as a function of the transverse momentum cut for reconstructed and triggered $B_s^0 \rightarrow K^+ K^-$ . . . . .	63
4.23	$\epsilon_{\text{eff}}$ for opposite-side kaon tagger as a function of the $IP/\sigma_{IP}$ cut for reconstructed and triggered $B_s^0 \rightarrow K^+ K^-$ . . . . .	63
4.24	Main data flow of a tagging job. . . . .	73
5.1	The 1998 test beam telescope . . . . .	78
5.2	The cluster finding efficiency as a function of bias voltages for $R$ and $\phi$ detectors. . . . .	80
5.3	The cluster finding efficiency as measured on the central $R$ and $\phi$ detectors for 60 V and 90 V bias. . . . .	81
5.4	The resolution as a function of the projected angle for the 40 $\mu\text{m}$ and 60 $\mu\text{m}$ pitch regions . . . . .	82
5.5	Schematic view of the data acquisition system used for the VELO testbeams. . . . .	84
5.6	Detector layout used for the SCT128A testbeam. . . . .	84
5.7	Set-up of the detectors used for the silicons testbeams . . . . .	85
5.8	Schematic of the DAQ timing. . . . .	87
5.9	Block diagram of the SCT128A fast readout chip [3]. . . . .	88
5.10	The output of two daisy chained SCT128A chips . . . . .	89
5.11	The Hamamatsu $R$ and $\phi$ sensors on their production wafer . . . . .	90
5.12	The expected time domain response of the SCTA readout chip . . . . .	92
5.13	A beamtest event . . . . .	93
5.14	The most probable signal values as a function of the readout time, separately for the non-irradiated and irradiated regions of the detector. The results of fits to the distributions are superimposed. [4] . . . . .	94
5.15	Strip layout of the Hamamatsu prototype detectors. . . . .	95
5.16	Positions of the instrumented regions of the test detector with the received irradiation dose superimposed. . . . .	96
5.17	The irradiation map of the Micron test sensor . . . . .	97
5.18	Charge collection efficiency of the Hamamatsu prototype as a function of the bias voltage for different radiation doses. . . . .	98
5.19	The cluster extent of the Hamamatsu detector at different voltages . . . . .	100
5.20	Charge collection efficiency of the Micron detector as a function of the bias voltage for different irradiation levels. . . . .	101
5.21	The cluster extent of the Micron detector at different irradiation doses. . . . .	102



# List of Tables

1.1	The three families of fundamental particles . . . . .	4
1.2	The four fundamental interactions. . . . .	10
3.1	Cross sections assumed for the LHC experiments. . . . .	35
4.1	Fractions of weakly decaying b hadron species in $Z \rightarrow b \bar{b}$ decay and in $p\text{-}\bar{p}$ collisions at $\sqrt{s} = 1.8 \text{ TeV}$ . Table from [5]. . . . .	55
4.2	Branching ratio for the dominant decay channels of the main b hadrons. Data from [5]. . . . .	55
4.3	Tagging efficiency for opposite-side muon, electron and kaon tags after various steps of the simulation for $B_{(s)}^0 \rightarrow h^+h^-$ events. . . . .	55
4.4	The list of categories used when combining tags . . . . .	66
4.5	$\mu$ tagging per trigger for $B_{(s)}^0 \rightarrow hh$ . . . . .	67
4.6	$\mu$ tagging per trigger for $B_s^0 \rightarrow (J/\psi(1S) \rightarrow \mu \mu)(\phi(1020) \rightarrow K^+ K^-)$ . . . . .	67
4.7	e tagging per trigger for $B_{(s)}^0 \rightarrow hh$ . . . . .	68
4.8	e tagging per trigger for $B_s^0 \rightarrow (J/\psi(1S) \rightarrow e e)(\phi(1020) \rightarrow K^+ K^-)$ . . . . .	68
4.9	$K_{OS}$ tagging per trigger for $B_{(s)}^0 \rightarrow hh$ . . . . .	69
4.10	Vtx Q tagging per trigger for $B_{(s)}^0 \rightarrow hh$ . . . . .	69
4.11	Sensitivity of the combined tagging to the different trigger levels. . . . .	69
4.12	Frequency of multiple visible interactions. . . . .	70
4.13	Frequency of reconstructed primary vertices. . . . .	70
4.14	Tagging power of the muon as a function of the number of visible interactions (for reconstructed and triggered $B \rightarrow hh$ events). . . . .	70
4.15	Tagging power of the electron as a function of the number of visible interactions (for reconstructed and triggered $B \rightarrow hh$ events). . . . .	70
4.16	Tagging power of the opposite-side kaon, on the left per visible interactions, on the right per reconstructed primary vertices (for reconstructed and triggered $B \rightarrow hh$ events). . . . .	70
4.17	Tagging power of the same-side kaon, on the left per visible interactions, on the right per reconstructed primary vertices (for reconstructed and triggered $B_s^0 \rightarrow D_s^\pm K^\pm$ events). . . . .	71

4.18	Tagging power of the vertex charge, on the left per visible interactions, on the right per reconstructed primary vertices (for reconstructed and triggered $B \rightarrow hh$ events). . . . .	71
4.19	Variation of the combined tagging power for single and multiple visible interaction events (for reconstructed and triggered $B_s^0 \rightarrow D_s^\pm K^\pm$ events). . . . .	71
4.20	Summary of the combined tagging power for different $B_d$ channels (top) and $B_s$ channels (bottom) after L0&L1 and selection. The entries in bold face are combined results of some of the preceding channels. . . . .	72
5.1	The range of readout times for which the overspill fraction is less than 30%. min and max reflect the evolution of the allowed timing due to the variation in the capacity of the strips on the detector and thus the pulse shape. . . . .	94

# Chapter 1

## Introduction

---

The goal of this chapter is to vulgarise my work and its context for an audience made of non-physicists. It covers essentially the basic knowledge needed to understand the rest of this document. Physicists accustomed to high-energy physics may want to skip to Chapter 2.

---

High-energy physics experiments try to collect information about the tiniest constituents of our universe and about their interactions. The term *high-energy* comes from the fact that a high density of energy is needed to create these bricks and the fact they move across the experiment at a speed very close to the speed of light. Because of their speed and their tiny effect on the instrumentation, observing their trajectory and measuring their energy with enough accuracy require large detectors.

The development of such a large experiment implies the need of a lot of manpower in many fields. The LHCb experiment counts about 500 physicists from about 50 institutes and universities around the world. Its development will have taken more than 10 years and it's expected to take data for almost 10 years too. Its construction has just started for a commissioning in 2007.

This chapter will explain why so much effort is put in place. It will start by a description of the world as known by particle physicists: the fundamental building blocks and the forces that govern them. And will end by a description of the LHCb experiment itself.

### 1.1 Fundamental Physics

Experiments like LHCb try to improve our understanding of the bricks our universe is made of and find the “fundamental” constituents.

The *matter*, the set of building blocks, can be defined in many ways depending on the complexity of the physical system they constitute. In high-energy physics only the smallest and simplest systems are considered to be the elementary particles. Physicist want to understand the laws which governs these particles.

Everyone will find matter around him. This matter is made of three different particles and is ruled by four interactions or forces. Actually, the world contains many more fundamental particles but they are not observed in the composition of the commonly available matter because they don't live long enough.

Particles physicists try mainly to produce these short-lived particles because they provide information about the fundamental forces. Producing these particles requires large accelerators like the LHC.

All these fundamental particles and their interactions are described by the so-called *Standard Model*. It was developed during the 20th century and has not changed much since 1974. All the high-energy experiments have tested the predictions of the Standard Model and measured its parameters up to the level which makes it the most precise theory. Up to now, no contradiction have been found but it is known to be an incomplete theory.

## 1.2 Particles

Already in times of Antiquity, man thought that matter can be split in smaller and smaller part up to a limit. This limit was called *atom* from the Greek word meaning "unbreakable".

Dalton<sup>1</sup> showed that atoms can indeed explain chemical reactions in a very simple way. Later on, Mendeleev<sup>2</sup> classified the atoms in its periodic table of the elements. This showed that atoms have a wide variety of chemical properties but they also have a lot of similarities.

### 1.2.1 The atom

In 1911, Rutherford<sup>3</sup> showed that the atom has a structure. Atoms are made of a very hard and tiny central part known as the *nucleus* surrounded by a cloud of *electrons*.

The electrons bear a negative electric charge while the nucleus has a positive charge. The two pieces of the

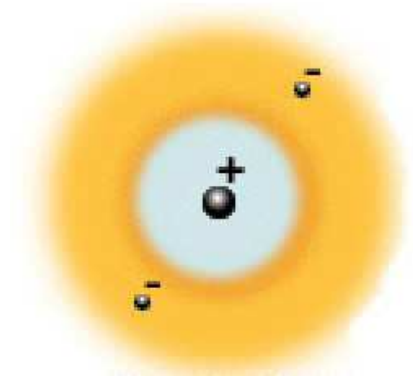


Figure 1.1: *Representation of the atom as a cloud of electrons surrounding a small and hard nucleus [1].*

<sup>1</sup>John Dalton, 1766-1844.

<sup>2</sup>Dmitri Ivanovitch Mendeleev, 1834-1907.

<sup>3</sup>Ernest Lord Rutherford, 1871-1931.

atoms stick together with the help of the electromagnetic force and have a globally neutral electric charge.

It turns out that the number of electrons in an atom explains its chemical properties and its place in the periodic table of the elements.

### 1.2.2 The nucleus

If the electron is still supposed to be a fundamental particle without structure, this is not the case of the nucleus. A closer “look” at the nucleus will reveal a structure made of two kinds of particles, the proton and the neutron. The proton carries a positive charge and the neutron is neutral.

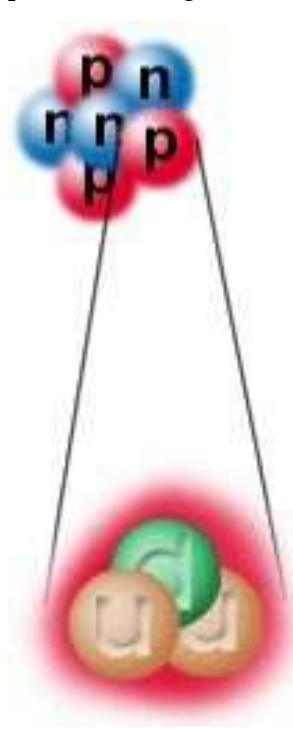


Figure 1.2: *The nucleus is made of protons and neutrons, which are themselves made of the “up” and “down” quarks [1].*

one u and two d quarks. With the addition of the electron and the electron neutrino, we have the fundamental set of particles which build the bulk of everyday life.

The discovery of the proton was the solution to the observed difference in the electric charge of the nucleus, as well as its mass, between the different elements but it raised another question. How can these positive charges stick together in such a small volume? The electric repulsion should make the nucleus explode.

One can notice that the number of neutrons increases faster than the number of protons in the different elements. So they must play a role to keep the nucleus stable. A few models were tested until a good solution was found but the conclusion is that a new force is in action inside the nucleus and it is stronger than the electromagnetic force. For this reason it is called the *strong* interaction.

### 1.2.3 The quarks

While studying the three particles electron, proton and neutron, physicist discovered a plethora of other particles. Finally, Gell-Mann<sup>4</sup> introduced the *quarks* as fundamental particles to put some order in the hundreds of particles known at that time.

The most common quarks are the *up* quark (denoted “u”), which has an electric charge of  $+2/3$ , and the *down* quark (“d”) with a charge of  $-1/3$ . With these fundamental particles we can build a proton by assembling two u quarks and one d quark. Similarly, the neutron is made of

<sup>4</sup>Murray Gell-Mann, 1929-.

### 1.2.4 The fundamental particles

Aside of these four particles eight other particles have been discovered which are believed to be elementary. Table 1.1 lists all the known fundamental particles. They are grouped into families. The quarks in the upper row have the same charge ( $+2/3$ ) and are named, in order: *up*, *charm* and *top*. Similarly the bottom row quarks have a charge of  $-1/3$  and are called: *down*, *strange* and *bottom*.

Leptons	$e^-$	$\mu^-$	$\tau^-$
	$\nu_e$	$\nu_\mu$	$\nu_\tau$
Quarks	u	c	t
	d	s	b

Table 1.1: *The three families of fundamental particles*

The mass of the quarks are not exactly known because the strong interaction does not let us observe the quarks alone; it is thus inferred from the mass of other particles which include both the mass of their constituent quarks and a contribution from the interaction itself.

The proton and neutron have already been described as a triplet of quarks. Other triplets exists and they are all known as *baryons*<sup>5</sup>.

The remaining particles are called *leptons*<sup>6</sup>. They consist of three particles with a charge of  $-1$ : the *electron* “ $e^-$ ”, the *muon* “ $\mu^-$ ” and the the *tau* “ $\tau^-$ ”, and their neutral companions called *neutrinos*: “ $\nu_e$ ”, “ $\nu_\mu$ ” and “ $\nu_\tau$ ”.

The neutrinos are almost massless and interact so rarely that everyone’s body experiences billions of neutrinos produced by the sun passing through it every seconds without noticing it.

Only the lightest family is in general observed because of the law of nature which states that all physical systems seek a state of lowest energy. As stated by the most famous formula of science, Einstein’s<sup>7</sup>  $E = mc^2$ , mass is like energy and if allowed, an heavy particle will decay to a lightest one. Actually, muons are also produced after a high-energy cosmic rays interacts with our atmosphere so they are not as rare as the others.

<sup>5</sup>Baryon comes from a Greek word meaning heavy.

<sup>6</sup>Lepton is the counterpart of baryon and means light in Greek.

<sup>7</sup>Albert Einstein, 1879-1955



### 1.2.5 Matter

All the particles we have already discussed form what we call *matter*. In everyday life, people will only encounter matter made of the particles in the light gray box of Table 1.1.

As mentioned before, high-energy physicists need to study also the less common particles. To produce them, accelerators are used to concentrate a lot of energy in one or two particles and then a collision is produced. During this collision the accumulated energy is released and can create these heavier particles.

When matter is created in this process it is always accompanied by some other particles which differ by the fact that their charge is the opposite of the charge of the matter particle.

### 1.2.6 Anti-matter

This “opposite-charge matter” is what is called *anti-matter*. Anti-matter is the set of twelve *anti-particles* obtained by changing the sign of the charge of the corresponding particle.

The first anti-particle discovered was the anti-electron or positron “ $e^+$ ”. The existence of the positron was predicted by P. A. M. Dirac in 1928. It has the same mass as the electron but its charge is positive instead of negative.

In notation, anti-particles are distinguished from particles either by the sign or by a bar placed above the symbol of the particle. Thus the anti-quarks with a charge of  $-2/3$  are denoted:  $\bar{u}$ ,  $\bar{c}$  and  $\bar{t}$  and the anti-quarks of charge  $+1/3$  are:  $\bar{d}$ ,  $\bar{s}$  and  $\bar{b}$ . The anti-leptons are:  $e^+$ ,  $\mu^+$ ,  $\tau^+$ ,  $\bar{\nu}_e$ ,  $\bar{\nu}_\mu$  and  $\bar{\nu}_\tau$ . The neutrinos, which are neutral, differ from the anti-neutrino by an opposite leptonic number which is an intrinsic property of the leptons.

By using anti-particles, anti-atoms can be assembled (this has been done at CERN). Theoretically, anti-molecules or even bigger construct can be made with anti-atoms but this is very difficult to achieve experimentally. The main problem reside in the fact that when particles and anti-particles meet each-other they will disappear in a flash of energy (usually light). This is just the reverse of the mechanism used to produce them and a striking demonstration of  $E = mc^2$ .

As anti-matter has the same property as matter and can be assembled in the same way, one can imagine a complete anti-universe. In that case what matter and anti-matter are is just a question of convention.

As mentioned above, matter and anti-matter have a hard time coexisting closely but at some larger scale a segregation might have occurred and we might just be living in a bubble of matter while somewhere else bubbles of matter or anti-matter might exist.

Astronomical observations indicate that the visible universe doesn't have such

well isolated bubbles. If a bubble of anti-matter exists somewhere in the universe it must interact with the surrounding matter and we should observe a lot of light coming from these regions. As no observations exist to support this idea, we must conclude that our universe is only made of matter. But in laboratory matter cannot be created alone and cosmologists believe that after the “Big Bang” the number of particles was identical to the number of anti-particles.

So why is today’s universe only made of matter? What is the origin of this asymmetry?

The LHCb experiment, like others, will collect some more informations to try to give an answer to this question. The strategy is to study closely the behaviour of the  $b$  and  $\bar{b}$  quarks. As the quarks can not be observed freely, it’s the lightest particles containing a  $b$  quark which will be studied, the B mesons.

### 1.2.7 The mesons

Nature does not allow two quarks combinations but it allows an assembly a quark and an anti-quark. As a combination of two quarks is lighter than the one of three quarks but still heavier than a lepton, a pair of quark–anti-quark was called a *meson*<sup>8</sup>.

The lightest mesons containing “beauty” quarks are the B mesons. They are the  $B^0$  ( $\bar{b}$  and  $d$ ) and the  $B^+$  ( $\bar{b}$  and  $u$ ) and the corresponding anti-particles, the  $\bar{B}^0$  ( $b$  and  $\bar{d}$ ) and the  $B^-$  ( $b$  and  $\bar{u}$ ).

If the  $u/\bar{u}$  or  $d/\bar{d}$  quark is replaced by another one we obtain even more B mesons<sup>9</sup>.

Actually, these particles are not studied directly because their life last only a few millionth of a millionth of a second, but their decays are the most interesting thing anyway.

All particles made of quarks and/or anti-quarks, that is baryons and mesons, share some properties and are globally known as *hadrons*.

## 1.3 Interactions

Fundamental physics not only cares about the material constituent of our world. Physicists are also very much interested by the forces that govern the fundamental particles. These fundamental forces are often called *interactions* because they really describe how the particles interact with each-others.

---

<sup>8</sup>From the Greek word meaning medium.

<sup>9</sup>B baryons can also be produced when three quarks of which at least one is a  $b$  are assembled together.

Four fundamental forces are known to the physicists: gravity, electromagnetism, strong nuclear force and weak nuclear force. However in quantum mechanics the distinction between matter and interaction is much weaker than what could be imagined from the everyday life.

### 1.3.1 Gravity

The first serious description of gravity was done by Newton<sup>10</sup> which was extended by Einstein into what we accept today as the most correct model, the General Relativity.

The *gravity* is the force which shapes our universe and this is reflected in its mathematical expression which is the geometrical interpretation of General Relativity. Gravity has an influence on matter even on very long distance. It is a long-range force. It is also the weakest of the four fundamental forces but it acts on a huge quantity of matter which makes it the most commonly experienced force (everyone has let something fall at least once in their existence).

Unfortunately only special relativity has a place in the Standard Model. Indeed, gravity is still a distinct theory, which has not yet been unified with the three other interactions.

### 1.3.2 Electromagnetism

The electromagnetic interaction describes how charged particles interact with each others.

Unlike gravity, which is always attractive, the electromagnetic interaction is repulsive when the charges have the same sign and attractive when they are different. Like gravity, the range of the electromagnetic interaction is believed to be infinite.

Electromagnetism is the result of the work of Maxwell<sup>11</sup>, who unified in 1864 electricity and magnetism. At the same time he showed that light is another aspect of the same physical process. Actually visible light is just a very thin band in the energy spectrum of electromagnetic waves. Radio waves, micro-waves, infrared, X-Rays... are other part of the electromagnetic spectrum.

In quantum physics, the interactions are tightly integrated with the particles. Let's try to understand why this is possible.

Imagine a pool filled with water and two corks floating. If you push up and down one of the cork you will notice waves on the surface of water. These waves

---

<sup>10</sup>Sir Isaac Newton, 1643-1727.

<sup>11</sup>James Clerk Maxwell, 1831-1879.

will then move the other cork up and down. As you can see, the water introduces a coupling between the two corks. It makes them interact with each other.

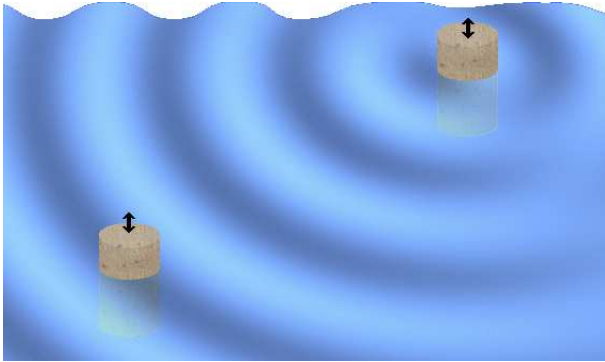


Figure 1.3: *Two corks interacting through the water surface coupling.*

a massless particle) and visible light is just a set of photons with an energy comprised in a small range. The energy carried by a photon of frequency  $\nu$  is given by the Planck formula  $E = h\nu$ .  $h$  is the Planck constant which is very very small.

If you push the cork up and down only once, you will see a single wave propagating on the water. This is the minimum needed to see the other cork react. In electromagnetism this is really the photon — the minimal piece of electromagnetic interaction, also known as a *quantum*.

When you push repetitively on the cork you will see a continuous oscillation of the water. The electromagnetic analogy is a continuous flow of photons.

### 1.3.3 Strong force

Paradoxically, being the strongest of all the interactions, the strong force is the most difficult to examine. The paradox is explained by the very short range of the strong force, which is of the order of the size of a proton ( $\sim 1$  fm).

The strong interactions bind together the quarks in the hadrons and outweigh the electromagnetic interactions inside the nucleus. Without the strong force, the nucleus of any element would explode.

Not all particles are coupled by the strong force. Just as electromagnetism only relates electrically charged particles, the strong force allows only “coloured” particles to interact.

The *colour* is the charge associated to the strong interaction. It is analogous to, but not the same as, colour as perceived by the eye. The colour comes in three fundamental “values”: “red”, “green” and “blue” and the strong force only allows

In electromagnetism, the corks are electric charges and the water is the electromagnetic field. The light is really just an oscillation of this field. It propagates like the waves on the water surface do.

This example suggests that the wave is the important thing when you consider the interaction. In high-energy physics, the vector of any interaction is modelled as a particle like the real ones. For the case of the electromagnetic interaction, this vector particle is the *photon* ( $\gamma$ ,

colour-neutral<sup>12</sup> or “white” objects. Anti-particles get the complementary colour or simply the same colour prefixed by “anti-”.

Only two ways exist to create white or neutral particles: – three particles, e.g. one red, one green and one blue, or – one particle and an anti-particle, e.g. one red and one anti-red (or cyan). The first combination correspond to the baryons and the second one to the mesons.

Only two kinds of particle carry colour, the quarks and the mediators of the strong force which are the *gluons* ( $g$ ). A gluon is a massless particle which exchanges the colour of two particles and is thus doubly coloured. Unlike photons, gluons can interact with each other as they carry colour charges. This particularity implies that the part of the model which takes care of the strong force is more complicated than electro-magnetism.

### 1.3.4 Weak force

The weak force is also a short range interaction and is slightly weaker than the electromagnetic force at typical distance (but it depends on the range). It acts on all particles, like gravity, and in particular on the neutrinos. It’s also the only interaction to which the neutrinos are sensitive. This explains the fact that neutrinos can traverse huge amounts of matter without troubles. Also the presence of neutrinos turns out to be a signature of weak interaction processes.

The weak interaction was observed long before the Standard Model was built. The simplest manifestation of the weak interaction is nuclear beta ( $\beta$ ) decay (one of the three radio-active decays). The  $\beta$ -decay transforms either a neutron into a proton plus an electron and an anti-neutrino or a proton into a neutron plus an anti-electron and a neutrino. The  $\beta$  ray emitted turns out to be either the electron or the positron. The neutrino was indirectly discovered in the  $\beta$  decay because some energy was missing (the neutrino, which carries some energy, is not observed).

The weak interaction is responsible for the instability of the heavy quarks and leptons. It’s also an ingredient of the nuclear energy generated by the sun and hence is at the origin of any life.

The vectors of the weak force are the  $W^\pm$  and the  $Z^0$ , which are hundred times heavier than the proton. They are one of the greatest achievement of the Standard Model, which predicted their existence before they were discovered at the beginning of the eighties at CERN.

---

<sup>12</sup>The additive model, the one used in your TV colour screen, is assumed.

Name	Vector	Intensity
Strong	gluon (g)	20
Weak	$Z^0, W^\pm$	$10^{-7}$
Electromagnetic	photon ( $\gamma$ )	1
Gravitation	graviton	$10^{-36}$

Table 1.2: *The four fundamental interactions.*

The effects of the gravitation are neglected by the Standard Model.

The intensity is given for two proton in a nucleus.

## 1.4 The Standard Model and beyond

The Standard Model was built step by step as the unification of the electromagnetism, the weak force and the strong interaction into a quantum relativistic mathematical model which links these three interactions with the set of 12 particles and their anti-particles.

Despite its success, the Standard Model is still waiting for the discovery of one more particle: the Higgs  $H^0$ . Without this particle, no massive particles should exist, which is definitely not what is observed.

The Large Hadron Collider (LHC) is the accelerator being built at CERN at which four experiments will take place. LHCb is one of these experiments. Of the three other experiments, two are dedicated to the discovery of the Higgs. If it is not observed, the Standard Model will be in deep trouble.

But even if the Higgs would be discovered, good reasons exist to believe that the SM is incomplete:

- Gravity is not part of the Standard Model. The fact that its effects are not observable at the particle level is not a reason to exclude it from the model and many attempts have been made to give a shape to gravity similar to the other three interactions.
- As previously stated, cosmological observations indicate that our universe is made of matter only. The Standard Model cannot really explain these observations.
- The Standard Model contains seventeen free parameters (eight of the nine masses of the quarks and leptons, the three couplings of the interactions, the four parameters of the CKM matrix, the vacuum expectation value of the Higgs field and  $\theta_{\text{QCD}}$ ). This might turn out to be even worse if the neutrinos were massive as seven more parameters must be added [6]. This is unacceptable for a fundamental model. Especially, the very different masses

of the quarks are not explained and they are responsible for one third of the parameters.

- Moreover, the model is based on an arbitrary choice of a symmetry group ( $SU(3) \otimes SU(2) \otimes U(1)$ ).

All these reasons support the idea that the Standard Model is a very good approximation but only for low-energy systems. If the energy available to a reaction becomes higher than what is feasible today, maybe new physics will be observed which points toward a more fundamental model. This is another reason for the creation of the LHC.

Theorists have not waited for some indication of new physics to try to create a more fundamental model. *Supersymmetry* is the most popular extension to the Standard Model.

## 1.5 Symmetries

When the physicist were facing a huge number of particles they tried to find similarities to classify all of them to see more clearly what was behind.

A way to try to understand the laws of nature is to look for *symmetries*. A symmetry is a transformation which doesn't affect the observed physical process or quantity. For instance, measuring the radius of a sphere will give the same value whatever rotation is applied to the sphere. If the sphere is a planet or a star this simple information provides some insight about the law which was responsible for the creation of the planet: gravity should exhibit a spherical symmetry.

The previous definition of symmetries is rather strict and can be used to describe exact symmetries like spatial translation (the laws of physics are the same here and on the moon) as well as rotation (finding the same result for an experiment whichever the direction I'm facing). In some case the transformation applied to the system will result in a slightly different value. In that case the symmetry is said to be *violated*. If the effect is really small, we have an almost perfect symmetry.

Of the many symmetries available in nature, high-energy physicists are mainly interested by two of them which are called P and C. These are the symmetries the LHCb experiment is interested in.

### 1.5.1 P parity transformation

Parity transformation is an operation which reverse all axes of a reference frame. To ease the intuition only one axis can be inverted, which leads to the mirror transformation. In this case, a system is transformed into its image in a mirror,

the axis perpendicular to the mirror being inverted with respect to its original pointing direction.

In our macroscopic world it's hard to distinguish between an image of something real and an image of its reflection in a mirror. But in the microscopic world things are different.

Particles have an intrinsic property called the *spin*, which is roughly a rotation of the particle on itself. This property is not affected by the parity transformation, like a propeller rotating clockwise in real-life will also rotate clockwise in the mirror perpendicular to the rotation axis (but the wind flow will go in the other direction).

The neutrino is a special particle: it always rotate clockwise on itself with respect to its direction of motion. But if you look at it in a mirror, instead of going away from you, it will come closer still rotating clockwise, which means it's rotating counter-clockwise with respect to its direction of motion. As this counter-clockwise neutrino doesn't exist, the original and the image in the mirror can be distinguished.

So far only the weak interaction has been found to violate the parity transformation.

### 1.5.2 C charge conjugation

Charge conjugation simply changes the sign of all the charges of a particle. This turns out to exchange a particle with its antiparticle.

Experiments studying charge conjugation need to compare the behaviour of particles and their antiparticles and see if they are really identical. When a difference is found, we call it an *asymmetry*.

The antineutrino is also special as it always rotates counter-clockwise. This implies that the charge conjugation is also violated by the weak force as a clockwise neutrino can not be charge-conjugated into clockwise antineutrino which does not exist.

### 1.5.3 CP symmetry

We have seen that transforming a neutrino with either P or C we don't get an existing particle. But if both symmetries are applied at the same time a clockwise neutrino will be transformed into a counter-clockwise antineutrino, which does exist.

If CP is a real symmetry for the neutrino, it is not for at least two other particles.

The weak decay of the  $K^0$  and  $\bar{K}^0$  as well as the  $B^0$  and  $\bar{B}^0$  are not identical. The BABAR and Belle experiments have shown that the asymmetry is very large in the case of the B mesons. If the amplitude of the asymmetry is very large, this



may explain why our world is mainly made of matter. This is why the B mesons are of great interest to the physicist.

## 1.6 Flavour tagging

The LHCb experiment will study the differences between the decay of the B mesons and their antiparticle. To make these observations one can not just look at the decay products of the B. The B mesons can decay in many different ways but the  $\bar{B}$  can do the same and some of them are identical. For instance, both the  $B^0$  and the  $\bar{B}^0$  can decay into two pions. The difference is in the rate of such a decay. It can be more frequent with a B than with a  $\bar{B}$ .

In addition to observing the final decay products, one has to find a way to determine if the particle which has produced this decay was a B or a  $\bar{B}$ . This is what *flavour tagging* is all about and it is one of the studies presented in this thesis.

## 1.7 CERN and the LHC accelerator

CERN is the world largest research laboratory in high-energy physics [7]. Born in 1954 at the initiative of 12 European countries, it now counts 20 Member States.

The CERN laboratory provides the accelerators required by the particle physicist, and some infrastructure like computing facilities, R&D labs or stores and workshops.

The high-energy level required by modern experiment can only be obtained by increasing the kinetic energy of particles.

Accelerators are huge machines used to push the speed of particles close to the speed of light. Once the particle has acquired enough energy it will collide with the particle of another beam or a fixed target. At the time of the collision, the kinetic energy can be used to create new particles.

The LEP accelerator applied this technique, colliding electrons against positrons, to observe the heavy particles mediating the weak force, the  $Z^0$  and  $W^\pm$ . If the electron and positron were not accelerated they would not have enough energy to produce any interesting particles but the photon.

The LEP with its 27 kilometres was only the end of a chain of bigger and bigger accelerators. Actually, small accelerators are very common nowadays. Each TV has a small electron accelerator which can deliver electrons with an energy of about 10 kilo-electron-volt (keV). LEP was producing electrons and positrons of 100 GeV (100'000'000 times more!) but this was possible, given the size of the accelerator.

In order to reach the high energy of interest to the physicist the particles must either be accelerated very quickly or for a long time. The second method being the simplest to implement, it's the one mostly used. However, at almost the speed of light this means the particles will cover a very long path. The only solution is to fold this path on itself, thus the circular shape of the LEP.

Just as taking a curve at high-speed is quite difficult if your car is light, it is hard to keep the electron in the accelerator above some energy. But if your car is much heavier this curve can be taken at a higher speed.

The Large Hadron Collider (LHC) [9] will occupy the same place used by the LEP but it will accelerate protons, which are 2000 times heavier than the electrons. The proton will reach an energy of 7 TeV, which is 70 times larger than the electrons of LEP.

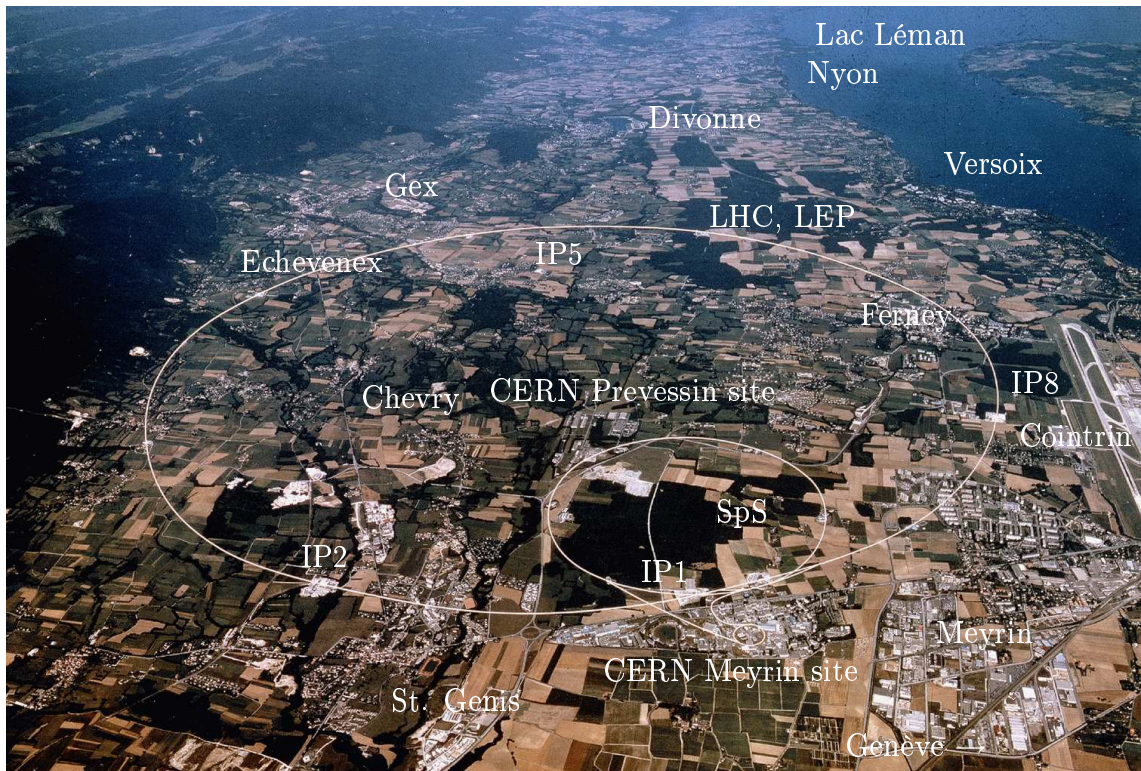


Figure 1.4: *The site of the LHC near Geneva. The “IP” are the points where the two proton beams will interact. The LHCb experiment will be located at IP8. Picture from [8].*

## 1.8 The LHCb experiment

Once the accelerated particles collide and produce new particles, physicists want to observe them. Most of the time the created particles don't live long enough to be observed directly. When these particles die, they *decay* into a set of lighter particles. Subsequent decays can happen until only stable particles are left.

A particle physics experiment will try to observe all these final decay products and then reconstruct the phenomena. The *detector* is the device responsible of the observation.

The detectors use the effects of the interaction of the particles with the matter to observe them. These effects are used in different way to extract some information about the particles. For this reason, an experiment is made of a set of detectors each designed for a special goal.

### 1.8.1 An example of detector, the Vertex Locator of LHCb

In LHCb, the B mesons produced will be able to fly for a few millimetres. This is not enough to be observed but enough to see that their decay products don't come from the position where the two protons collided, the "Interaction Point".

The flight length of the B meson is a key measurement for the physicist as will be discussed later in more detail. For this reason a detector is dedicated to finding precisely where the particles originated. The point of origin of a set of track is called a *vertex*.

LHCb's Vertex Locator (VELO) is made of 21 independent planes of detection. Each of these planes is made of 4 silicon microstrip detectors.

Silicon is a semiconductor material as used in any electronic device. Unlike conductors, which contain electrons free to move as they like, semiconductors keep the electrons bound to the atomic structure. However this binding is much looser than in insulators. To break the binding of an electron in a semiconductor requires just a few electron-volts. This feature make semiconductors perfect to detect charged particles. When particles pass through the silicon they will loose a few kilo-electron-volt and will free thousand electrons along their path. These electrons are amplified and driven to an electric wire, giving birth to an electrical impulse, which can be measured.

This example illustrates the basis of particle detection: to have the particle induce other particles (electrons or photons) in the bulk material of the detector and then collect them.

## 1.8.2 Description of the LHCb experiment

The LHC will host four detectors, two general-purpose detectors, ATLAS and CMS, and two specialised detectors, ALICE and LHCb.

The main goal of the LHCb experiment is to study CP violation in the decay of B mesons [10]. At the LHC, these mesons will mainly be produced along the direction of the accelerator beams. For this reason, LHCb is designed to be able to catch particles at a small angle.

The detector will be made of six sub-detectors with specialised purposes placed one after the other for a total length of 20 meters and a height of 10 meters.

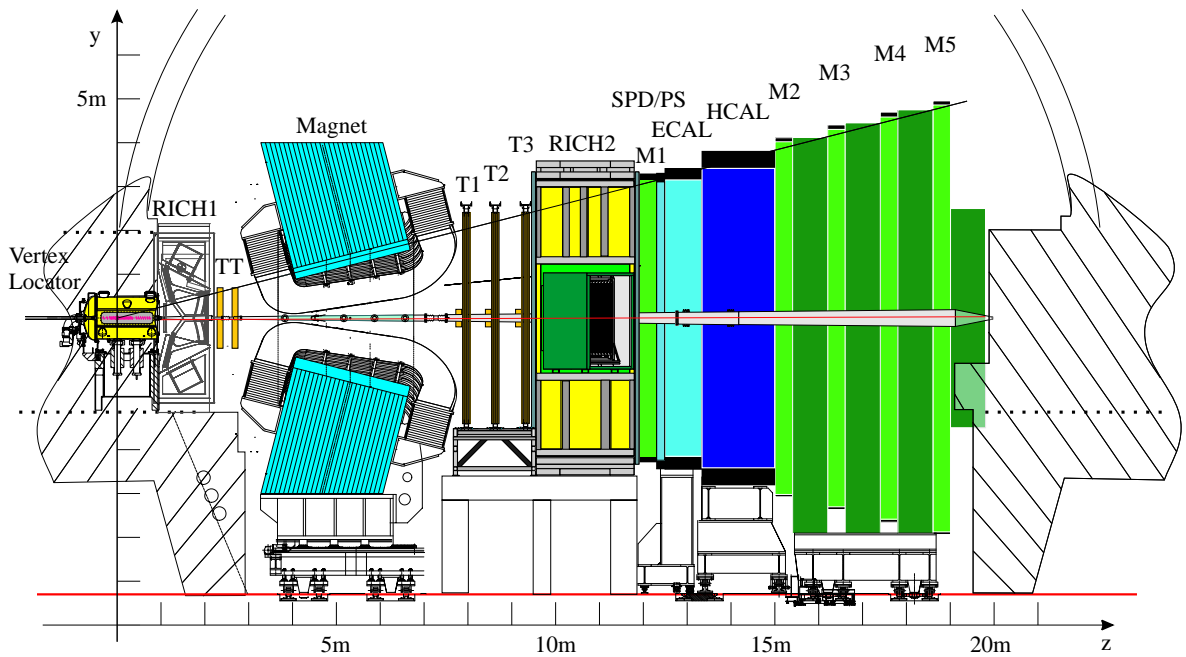


Figure 1.5: *Side view of the LHCb detector. Figure from [2].*

Figure 1.5 shows what the detector will look like from the side. The VELO is on the left and it's where the interaction point is located. After the proton-proton collision, the unstable and short-lived particles will decay before leaving it. Next is the first RICH (Ring Imaging Cherenkov) detector, which specialises in the identification of particles. Immediately after it is the first tracking station (TT). Between the two sets of tracking stations lies the magnet, which will bend the charged particles in order to measure their momentum. After the magnet, three tracking stations are present, which provide seeds for the track reconstruction. Those four detectors provide information used to reconstruct the path followed by each particle. Then comes the second RICH detector followed by the first muon chamber. The electromagnetic calorimeter (ECAL), further down, will stop

photons and electrons and measure their energy. The hadronic calorimeter (HCAL) does the same thing for the hadrons. Finally the detector ends with four muon chambers, which provide tracking information and identification for the muons.

### 1.8.3 Trigger and data acquisition

For every “event” in which a proton–proton collision happens the detectors will produce data which need to be collected, filtered to select only “interesting” events and, in case of a positive decision, stored in a central place. One can easily imagine that such a large detector will produce a lot of data. Indeed this turns out to be a major challenge because the size of the data corresponding to one event multiplied by the event rate could be very large.

The previous generation of large experiments present at LEP were observing an interesting event every few seconds. LHCb will save around 200 events per second, three orders of magnitude the rate of LEP’s experiments. This requires a state of the art data acquisition system specifically designed for the experiment.

Actually, the most difficult task is not the read-out of all the data but the decision to read them. This decision will be taken by what we call the *trigger*, a set of hardware and software algorithms which must decide whether two protons collided and if the resulting particles are interesting.

Forty million times per second two bunches of protons will cross each-other and roughly one time in four a collision will happen. Only 1% of these collisions will produce a B and only a few of them are really of interest to the physicist. To select just these events the LHCb trigger will reconstruct some of the tracks left by the particles in the VELO and look for a secondary vertex, which would be the signature of a possible B meson decay.

Such a reconstruction takes a lot of computing power and time. During the decision process the data are stored locally in the detector electronics.

### 1.8.4 Simulations

Developing such a large experiment takes a lot of time in a long iterative process where possible solutions are tested until the best one is found. Obviously, rebuilding the whole detector many times is not an option. To avoid this problem the detector only exists at first in a virtual world — a simulation. That way changing the geometry, the number of sub-detectors or what technology they use is just a matter of changing a few thousand lines of code in a program which is usually called a “Monte-Carlo” because it makes use of random number generators

Small parts of the detector are also built and tested, and the results compared with the simulation for consistency.

After this phase of Research and Development, which last around 10 years, the detector will be assembled in its cave and it will take data for 10 more years. But the end of the R&D phase doesn't mark the end of the simulation which will enter a new phase. This new phase will last as long as data are still to be analysed. The simulation contains our complete knowledge about the physical processes involved. A way to check that our views are correct is to compare the outcome of the simulation with the output of the real detector. Sometime it's not even possible to measure directly a physical parameter because it's deeply buried inside a complicated phenomenology. In such cases, the only solution is to make a simulation of what would happen for different values of this parameter and compare the result of the simulation with the experimental data.

# Chapter 2

## Theoretical Overview

---

This chapter presents the current model of particle physics as a minimal basis to understand the motivation for the LHCb experiment and why the flavour tagging is needed. The Standard Model is introduced followed by the mixing of the quarks and the CP violation mechanism. The following sections are inspired by [6, 11, 12, 13]

---

The Standard Model (SM) is ubiquitous in the realm of particle physics. No other model has been able to describe with comparable simplicity and precision the experimental results obtained so far.

Physicists still believe that the SM is not the whole story but just a part of the *Grand Unified Theory* (GUT), which still awaits discovery. Despite the fact that no observation exists to support another model beyond the Standard Model, open questions still exist.

In particular, the origin of the fermion masses and mixing as well as the fact that the weak interaction breaks the C, P, CP and T symmetries need to be explained. The weak interaction looks like the key to new physics and this is the main reason to study the weak decays of mesons.

The B-factories [14, 15, 16] have recently observed CP violation in B meson decays and found it larger than in K meson decays. However precise measurements involving high statistics are required to be able to sufficiently constrain the theoretical models and confirm or rule out models beyond the SM.

Fortunately the LHC will be capable of providing such high statistics.

## 2.1 The Standard Model

The Standard Model was developed as a step by step unification of the electromagnetic, weak and strong interaction. To understand the rest of this writeup, only the first step, known as the *Electroweak Standard Model* is required.

The following sections will begin with the construction of the leptonic part of the electroweak Standard Model [17, 18, 19] and then it will be extended to the hadrons.

### 2.1.1 Leptonic Electroweak Standard Model

The model is contained in a *Lagrangian density*  $\mathcal{L}$  which must be invariant under a *gauge group*  $G$  and describes all couplings of the elementary particle *fields*. In addition to these fields, one vector field per generator of  $G$  are required as well as  $N + 1$  scalar fields with  $N > 0$  if vector fields are to be massive.

**The elementary lepton fields:** Twelve fermions must be described. The six leptons  $e, \nu_e, \mu, \nu_\mu, \tau, \nu_\tau$  and their anti-particles. They are grouped by family and helicity. The left-handed states ( $L = \frac{1}{2}(1 - \gamma^5)f$ ) are denoted:

$$L = \begin{pmatrix} e \\ \nu_e \end{pmatrix}_L, \quad \begin{pmatrix} \mu \\ \nu_\mu \end{pmatrix}_L, \quad \begin{pmatrix} \tau \\ \nu_\tau \end{pmatrix}_L$$

and the right-handed one are  $R = \frac{1}{2}(1 + \gamma^5)f = e_R, \mu_R, \tau_R$ . No right-handed neutrino has ever been observed and they are thus not present in the Standard Model.

**The gauge group and its generators:** Experimental results clearly suggest the existence of processes driven by charged and neutral currents. These currents are mediated by the  $W^+, W^-$  and  $Z^0$ . The phenomenology also tells us that the charged current only couples to the left-handed part of the fermion fields. It turns out that  $SU(2)_L$  is the simplest group which can account for such a structure and it has three generators, which will be noted  $W_\mu^i, i \in \{1, 2, 3\}$ . In order to let the right-handed particles interact we need to extend this group. This extension is justified by the neutral current and the electromagnetic interaction, which can be represented by the group  $U(1)$  with its neutral generator  $B_\mu$ . The complete gauge group is then:

$$G = SU(2)_L \otimes U(1). \quad (2.1)$$

Two coupling constants  $g$  and  $g'$  are associated to these two groups.



**The scalar fields:** The generators of the gauge group are not yet the vector “gauge” bosons we need,  $W^+$ ,  $W^-$ ,  $Z^0$  and  $\gamma$ , because they are still massless while the first three must have a mass. These masses can be generated by the Higgs mechanism [20]. As three fields must acquire some mass, at least three scalar fields are required to give the gauge bosons the longitudinal degree of freedom.

The simplest solution is a doublet of complex scalar fields

$$\phi = \begin{pmatrix} \phi^+ \\ \phi^0 \end{pmatrix}. \quad (2.2)$$

In the “spontaneous symmetry breaking” mechanism, this field is non-zero in the vacuum

$$\phi_{\text{vac}} = \begin{pmatrix} 0 \\ \frac{v}{\sqrt{2}} \end{pmatrix}.$$

Through this mechanism, the potential  $V(\phi) = \mu^2 \phi^\dagger \phi + \lambda(\phi^\dagger \phi)^2$  will be used to give masses to the gauge bosons by a choice of  $\mu^2 < 0$ .

With these elements, the most general Lagrangian describing the interactions of the fermions (F), the vector bosons (B) and the scalar fields (S) looks like:

$$\mathcal{L}_{\text{weak}} = \underbrace{\mathcal{L}_{\text{FB}} + \mathcal{L}_{\text{BB}}}_{\mathcal{L}_{\text{GWS}}} + \underbrace{\mathcal{L}_{\text{SF}} + \mathcal{L}_{\text{SB}}}_{\mathcal{L}_{\text{Higgs}}} \quad (2.3)$$

where the boson self-coupling is

$$\mathcal{L}_{\text{BB}} = -\frac{1}{4} W_{\mu\nu}^j W^{j\mu\nu} - \frac{1}{4} B_{\mu\nu} B^{\mu\nu} \quad (2.4)$$

with

$$\begin{aligned} W_{\mu\nu}^j &= \partial_\mu W_\nu^j - \partial_\nu W_\mu^j + g\epsilon^{jkl} W_\mu^k W_\nu^l \\ B_{\mu\nu} &= \partial_\mu B_\nu - \partial_\nu B_\mu. \end{aligned}$$

The fermions–bosons coupling is made of two parts, one for the left-handed particles and another one for the right-handed:

$$\mathcal{L}_{\text{FB}} = \bar{L} i \gamma^\mu \left( \partial_\mu - \frac{1}{2} i g' B_\mu + \frac{1}{2} i g \tau_j W_\mu^j \right) L + \bar{R} \gamma^\mu (i \partial_\mu - g' B_\mu) R. \quad (2.5)$$

For the scalar field and the fermions an ad hoc Yukawa coupling is introduced:

$$\mathcal{L}_{\text{SF}} = -G_{\text{F}} [(\bar{L}\phi) R - \bar{R}(\phi^\dagger L)] \quad (2.6)$$

which induces the fermion mass  $m_{\text{f}} = \frac{G_{\text{F}} v}{\sqrt{2}}$ .  $G_{\text{F}}$  is not predicted by the SM.

Finally the Lagrangian for the scalar and vector fields is:

$$\mathcal{L}_{\text{SB}} = \left| \left( \partial_\mu + \frac{1}{2}igW_\mu^j\tau_j + \frac{1}{2}ig'IB_\mu \right) \phi \right|^2 - V(\phi). \quad (2.7)$$

The actual Lagrangian gives a mass to all the vector fields. However, a degree of freedom is still present and we can use it to have a massless photon. We can express two of the vector fields as a linear combination of the photon and the Z field, which is massive [18]:

$$\begin{pmatrix} B_\mu \\ W_\mu^3 \end{pmatrix} = \begin{pmatrix} \cos \theta_W & \sin \theta_W \\ \sin \theta_W & \cos \theta_W \end{pmatrix} \begin{pmatrix} A_\mu \\ Z_\mu \end{pmatrix}. \quad (2.8)$$

$\theta_W$  is the Weinberg angle and is one of the Standard Model's fundamental parameter.

Equation 2.8 constrains the value of the weak coupling constants  $g$  and  $g'$  because the net coupling of the photon must be proportional to the electric charge. Thus we have:

$$e = g \sin \theta_W = g' \cos \theta_W. \quad (2.9)$$

This electric charge constraint must be applied to the remaining vector fields too with the effect of rotating them:

$$\begin{pmatrix} W_\mu^+ \\ W_\mu^- \end{pmatrix} = \frac{1}{\sqrt{2}} \begin{pmatrix} 1 & -i \\ 1 & i \end{pmatrix} \begin{pmatrix} W_\mu^1 \\ W_\mu^2 \end{pmatrix}. \quad (2.10)$$

Finally, the mass of the boson produced by the Higgs mechanism are as follows

$$m_W = \frac{gv}{2}, \quad m_{Z^0} = \frac{gv}{2 \cos \theta_W} = \frac{m_W}{\cos \theta_W} \quad \text{and} \quad m_\gamma = 0.$$

The Higgs boson itself has a mass of

$$m_H = \sqrt{-\mu^2}.$$

However, this is only true at first order, with the bare fields. At higher order divergences can occur which require a renormalization of the theory. 't Hooft and Veltman have shown that this is possible for all gauge theories.

We can now rewrite 2.5 in terms of the neutral 2.8 and charged 2.10 bosons

and the coupling constants 2.9:

$$\begin{aligned}\mathcal{L}_{\text{FB}} &= \mathcal{L}_{\text{FW}} + \mathcal{L}_{\text{FZ}} + \mathcal{L}_{\text{FA}} \\ \mathcal{L}_{\text{FW}} &= -\frac{e}{\sqrt{2}\sin\theta_{\text{W}}}\bar{L}\gamma^\mu(\tau_+W_\mu^+ + \tau_-W_\mu^-)L \\ &= \frac{e}{\sqrt{2}\sin\theta_{\text{W}}}(J_+^\mu W_\mu^+ + J_-^\mu W_\mu^-)\end{aligned}\quad (2.11)$$

$$\begin{aligned}\mathcal{L}_{\text{FZ}} &= \frac{e}{2}\bar{L}\gamma^\mu(\tan\theta_{\text{W}}Z_\mu + \cot\theta_{\text{W}}\tau_3Z_\mu)L - e\gamma^\mu R(\tan\theta_{\text{W}}Z_\mu) \\ &= \frac{e}{2\sin\theta_{\text{W}}\cos\theta_{\text{W}}}(J_3^\mu - 2\sin^2\theta_{\text{W}}J_{\text{em}}^\mu)\end{aligned}\quad (2.12)$$

$$\begin{aligned}\mathcal{L}_{\text{FA}} &= \bar{L}\gamma^\mu\left(i\partial_\mu + \frac{1}{2}e(1-\tau_3)A_\mu\right)L + \bar{R}\gamma^\mu(i\partial_\mu - eA_\mu)R \\ &= \bar{f}i\gamma_\mu(\partial_\mu - ieA_\mu)f\end{aligned}\quad (2.13)$$

where  $\tau_\pm = \frac{1}{2}(\tau_1 \pm i\tau_2)$ . The fermionic currents are

$$J_\pm^\mu = \pm\bar{L}\gamma_\mu\tau_\pm L \quad (2.14)$$

$$J_3^\mu = \bar{L}\gamma_\mu\tau_3 L \quad (2.15)$$

$$J_{\text{em}}^\mu = \bar{R}\gamma_\mu R - \frac{1}{2}\bar{L}\gamma_\mu(1-\tau_3)L = q_i\bar{f}_i\gamma_\mu f_i. \quad (2.16)$$

### 2.1.2 Hadronic extension

The extension to the hadrons is done by adding a field for each of the six quarks. The Lagrangian 2.3 the *wrong-tag fraction*  $w$  doesn't even need to be modified. The quarks are simply added as three more weak isospin multiplets in addition to the already present lepton weak isospin multiplets.

The Lagrangian of the full Standard Model is obtained by adding a QCD term to 2.3 which is symmetric under  $SU(3)_C$  ( $C$  for ‘‘colour’’) but it won't be used later on.

$$\mathcal{L}_{\text{SM}} = \mathcal{L}_{\text{GWS}} + \mathcal{L}_{\text{Higgs}} + \mathcal{L}_{\text{QCD}} \quad (2.17)$$

$$\mathcal{L}_{\text{QCD}} = \frac{1}{4}G_{\mu\nu}^\alpha G^{\alpha\mu\nu} + i\bar{q}_i\gamma_\mu(D^\mu)_{ij}q_j \quad (2.18)$$

with  $G_{\mu\nu}^\alpha$ ,  $\alpha \in [1, 8] \cap \mathbb{N}$ , being the gluon fields and  $q_j$  the quark fields. There is no coupling between the gluon and the Higgs field as the gluons are supposed to be massless.

### 2.1.3 The quark couplings

When looking more closely at the differences between quarks and leptons, one will notice that all six quarks are massive while the neutrino are massless (in this

version of the theory). This difference implies that the coupling with the scalar fields must be different otherwise only the upper three quarks would have a mass. Another difference is that the flavour of the quarks is not conserved by the weak interaction. During a charged current interaction a quark decays into a quark of another flavour. This allows for the decay of flavoured particles like the K and the B mesons.

Both these differences are modelled in one step by introducing “bare” quarks  $d_i^0$  and  $u_i^0$ ,  $i \in \{1, 2, 3\}$ , which are not the mass eigenstates but which couple to the scalar fields in the exact same way as the leptons do. With this solution, 2.6 takes this form:

$$\mathcal{L}_{\text{SF}} \propto \frac{v}{\sqrt{2}} (\bar{d}_{L i}^0 D^{ij} d_{R j}^0 + \bar{u}_{L i}^0 U^{ij} u_{R j}^0) + \text{h.c.}$$

$D$  and  $U$  are matrices, which can be diagonalized with the help of two unitary matrices, giving:

$$\frac{v}{\sqrt{2}} V_L^D D V_R^D = \begin{pmatrix} m_d & & \\ & m_s & \\ & & m_b \end{pmatrix} \quad \text{and} \quad \frac{v}{\sqrt{2}} V_L^U U V_R^U = \begin{pmatrix} m_u & & \\ & m_c & \\ & & m_t \end{pmatrix}.$$

This implies that the quark fields can be written as:

$$u_L = V_L^U u_L^0, \quad u_R = V_R^U u_R^0, \quad d_L = V_L^D d_L^0, \quad \text{and} \quad d_R = V_R^D d_R^0.$$

The interaction with the W (2.11) involves the charged quark current in 2.14, which now turns out to be:

$$J_{+, \text{quarks}}^\mu = \bar{u}_L^0 \gamma^\mu d_L^0 = \bar{u}_L \gamma^\mu \underbrace{V_L^U V_L^{D\dagger}}_{V_{\text{CKM}}} d_L. \quad (2.19)$$

The  $V_{\text{CKM}}$  term is the weak mixing matrix<sup>1</sup> which allows the charged weak interactions to mix quarks flavour. By convention it only mixes the down-type quarks and absorbs the diagonalization of the up-type quarks:

$$\begin{pmatrix} d' \\ s' \\ b' \end{pmatrix} = \underbrace{\begin{pmatrix} V_{ud} & V_{us} & V_{ub} \\ V_{cd} & V_{cs} & V_{cb} \\ V_{td} & V_{ts} & V_{tb} \end{pmatrix}}_{V_{\text{CKM}}} \begin{pmatrix} d \\ s \\ b \end{pmatrix}. \quad (2.20)$$

As  $V_{\text{CKM}}$  is unitary it disappears in the expression of the neutral current:

$$J_{3, \text{quarks}}^\mu = \bar{u}_L^0 \gamma^\mu u_L^0 - \bar{d}_L^0 \gamma^\mu d_L^0 = \bar{u}_L \gamma^\mu u_L - \bar{d}_L \gamma^\mu d_L$$

---

<sup>1</sup>It was introduced by Makoto Kobayashi and Toshihide Maskawa as an extension to Nicola Cabibbo's  $2 \times 2$  d-s mixing matrix [21, 22].

thus no mixing are present here.

Actually the mixing can still be seen in neutral current but not at the tree level. They would not exist at all if all the quarks of given charge had the same mass but that's not the case. The suppression of the flavour changing neutral currents in the  $K^0$  meson decay suggested the existence of the  $c$  quark to Glashow, Iliopoulos and Maiani [23].

## 2.2 CP violation

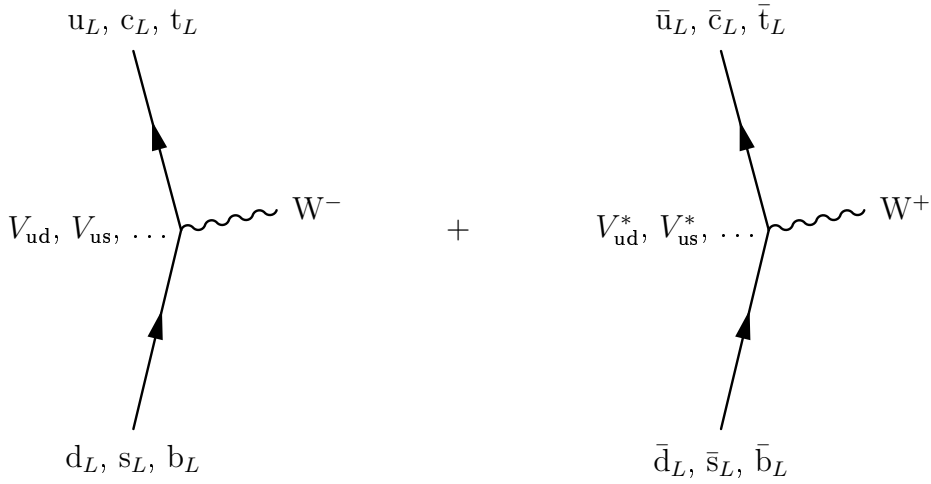


Figure 2.1: *Feynman diagram of the interaction between a quark and a  $W$ .*

CP violation is one of the most important fundamental mechanisms of the Standard Model. It's so important because it can distinguish matter and anti-matter and can help explain the fact that our universe is only made of matter. To understand how this mechanism is naturally present in the SM we will examine the quark- $W$  Lagrangian. Figure 2.1 shows the Feynman graph of these processes. The corresponding Lagrangian is

$$\mathcal{L} \propto \bar{u}_{Li} \gamma^\mu V_{ij} d_{Lj} W_\mu^- + \bar{d}_{Li} \gamma^\mu V_{ij}^* u_{Lj} W_\mu^+ \quad (2.21)$$

and after CP transformation

$$\mathcal{L}_{CP} \propto \bar{d}_{Li} \gamma^\mu V_{ij} u_{Lj} W_\mu^+ + \bar{u}_{Li} \gamma^\mu V_{ij}^* d_{Lj} W_\mu^-. \quad (2.22)$$

CP will be conserved if  $\mathcal{L} = \mathcal{L}_{CP}$ , which can only happen if  $V_{ij} = V_{ij}^*$ . With one or two quarks family this is the case because the CKM matrix can be constrained to be real. But this can no longer be true with three quarks families.

### 2.2.1 CKM matrix and unitary triangles

In the CKM case, the  $3 \times 3$  complex matrix contains nine free phases and 9 free moduli. With six quarks we can adjust five phases at our will leaving only four free phases. Also the matrix must be unitary, which implies nine more constraints. Three of them restrict further the phases so only one free phase exist. The last six constraints will reduce the 9 free moduli to three.

In conclusion, one of the matrix elements has a phase and for a non zero value it will be different from its conjugate. This means that CP violation can naturally arise in the SM.

These four free parameters are used to approximate the CKM matrix in the following way known as the Wolfenstein parameterisation [24]:

$$V_{\text{CKM}} = \begin{pmatrix} V_{ud} & V_{us} & V_{ub} \\ V_{cd} & V_{cs} & V_{cb} \\ V_{td} & V_{ts} & V_{tb} \end{pmatrix} \approx \begin{pmatrix} 1 - \frac{\lambda^2}{2} & \lambda & A\lambda^3(\rho - i\eta) \\ -\lambda & 1 - \frac{\lambda^2}{2} & A\lambda^2 \\ A\lambda^3(1 - \hat{\rho} - i\hat{\eta}) & -A\lambda^2 & 1 \end{pmatrix} \quad (2.23)$$

where  $\hat{\rho} = \rho \left(1 - \frac{\lambda^2}{2}\right)$  and  $\hat{\eta} = \eta \left(1 - \frac{\lambda^2}{2}\right)$ .

The unitarity of the CKM matrix means that the sum of the squared modulus of all the coefficients in a row or column is equal to one and that the different rows and columns are orthogonal. These six orthogonality relations can be represented as triangles in the complex plane. The area of these triangles turns out to be proportional to the strength of the CP violation. Of the six triangles two have comparable side lengths and are the most interesting ones. They are produced by the following relations and are depicted in figures 2.24 and 2.25:

$$V_{ud}V_{ub}^* + V_{cd}V_{cb}^* + V_{td}V_{tb}^* = 0, \quad (2.24)$$

$$V_{ud}^*V_{td} + V_{us}^*V_{ts} + V_{ub}^*V_{tb} = 0. \quad (2.25)$$

### 2.2.2 Measurements of the unitary triangles

It is very interesting to measure both the angles and the sides of the triangles thus over-constraining them. If all the measurements fits together we will have one more nice confirmation of the SM but if something goes wrong it will be a clear sign of the existence of some physical processes not foreseen by the Standard Model.

While the present B factories can make good measurements of  $\beta$ , the other angles will be known with reduced accuracy. This is the reason why the LHCb experiment has been devised.

The different characteristics of the unitary triangles can be measured through specific decays [25]:

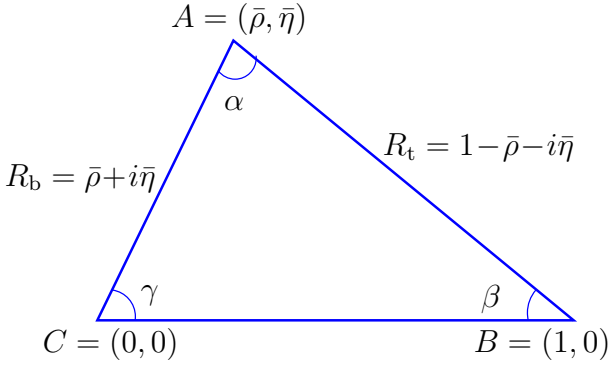


Figure 2.2: The main unitary triangle, corresponding to relation 2.24.

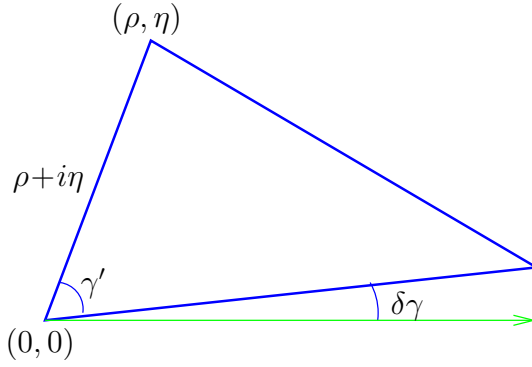


Figure 2.3: The unitary triangle corresponding to relation 2.25.

- $\alpha$ :  $B \rightarrow \rho\pi$  gives access to  $\sin 2\alpha$  as well as  $B \rightarrow \pi\pi$  but the last one requires the knowledge of the “penguin pollution”, which can be extracted from  $B \rightarrow K\pi$ .
- $\beta$ : The  $B^0-\bar{B}^0$  mixing phase  $\phi_B$  turns out to be equal to  $2\beta$  and can be extracted from  $B \rightarrow J/\psi K_S^0$  and similar channels. Also  $B \rightarrow \phi K_S^0$  allows the measurement of  $2\beta$  but it appears in a penguin loop. This difference can show signs of a new physics if both measurement don't give the same results.
- $\gamma$ : This angle cannot be measured directly but it can be extracted from the  $B \rightarrow D^*\pi$  channel, which depends on  $\gamma + \phi_B$  using  $\phi_B$  from the measurement described above. Or from  $B_s \rightarrow D_s K$ , which is sensitive to  $\gamma + \phi_{B_s}$ .
- $\delta\gamma$ : The  $B_s$  mixing phase  $\phi_{B_s}$  is equal to  $-2\delta\gamma$  and can be extracted from  $B_s \rightarrow J/\psi\eta$  or  $B_s \rightarrow J/\psi\phi$ .
- $|R_b|$ : This is the length of the CA side of the unitary triangle. It correspond to the ratio  $|V_{ub}|/|V_{cb}|$ . Both the numerator and the denominator can be obtained from inclusive semileptonic B decays.
- $|R_t|$ : This is the most difficult element to measure.  $|R_t| = \frac{1}{\lambda} \left| \frac{V_{td}}{V_{cd}} \right|$  in which the problematic term is  $V_{td}$ . At the LHC the most efficient way to extract it is through the ratio of the branching fraction of  $B \rightarrow \ell\ell X_{\bar{d}}$  and  $B \rightarrow \ell\ell X_{\bar{s}}$ , which is  $\frac{|V_{td}|^2}{|V_{ts}|^2}(1 + \text{corrections})$  and thus requires that  $|V_{ts}|$  is known.

### 2.2.3 CP phenomenology

In this section we will consider the mixing and decay of  $P^0$  and  $\bar{P}^0$  mesons where  $P^0$  refers to either  $K^0$ ,  $D^0$ ,  $B_d^0$  or  $B_s^0$ . It turns out that the general phenomenology

is the same for any flavoured neutral meson system (except mesons which are their own anti-particle).

As the weak interaction is the only one which can violate flavour, it is responsible for the decay of the neutral  $P^0$  mesons. Moreover, the fact that these mesons are neutral allows the weak interaction to mix  $P^0$  and  $\bar{P}^0$ , that means they can oscillate into one another before decaying.

So the wave function which describe the neutral mesons can be written as the sum of two components:

$$|\psi(t)\rangle = \psi_1(t)|P^0\rangle + \psi_2(t)|\bar{P}^0\rangle \quad (2.26)$$

where  $t$  is the proper time. It's evolution is governed by a Schrödinger-like equation:

$$i\frac{d}{dt} \begin{pmatrix} \psi_1 \\ \psi_2 \end{pmatrix} = \begin{pmatrix} H_{11} & H_{12} \\ H_{21} & H_{22} \end{pmatrix} \begin{pmatrix} \psi_1 \\ \psi_2 \end{pmatrix}. \quad (2.27)$$

The matrix  $\mathbf{H}$  is not Hermitian otherwise the mesons would not decay. However it can be written in terms of two Hermitian matrices with physical meanings:

$$\mathbf{H} = \mathbf{M} - \frac{i}{2}\mathbf{\Gamma}. \quad (2.28)$$

$\mathbf{M}$  is related to the mass and incorporates contributions from the intermediate virtual states, while  $\mathbf{\Gamma}$  is linked to the decay width and has contributions from the physical states to which both  $P^0$  and  $\bar{P}^0$  can decay. They are given, in the second-order perturbation theory, by sums over intermediate states  $n$  by:

$$M_{ij} = m_0\delta_{ij} + \langle i|\mathcal{H}_W|j\rangle + \sum_n P \frac{\langle i|\mathcal{H}_W|n\rangle\langle n|\mathcal{H}_W|j\rangle}{m_0 - E_n},$$

$$\Gamma_{ij} = 2\pi \sum_n \delta(m_0 - E_n)\langle i|\mathcal{H}_W|n\rangle\langle n|\mathcal{H}_W|j\rangle.$$

The operator  $P$  projects out the principal part.

If we consider the CP transformed system where  $P^0$  is interchanged with  $\bar{P}^0$  and assume that CP is conserved, we find that:

$$\begin{aligned} M_{11} &= M_{22} & M_{21} &= e^{2i\xi} M_{12} \\ \Gamma_{11} &= \Gamma_{22} & \Gamma_{21} &= e^{2i\xi} \Gamma_{12} \end{aligned}$$

where  $e^{2i\xi}$  comes from the arbitrary phase introduced by the CP transformation:

$$\text{CP}|P^0\rangle = e^{i\xi}|\bar{P}^0\rangle \quad \text{CP}|\bar{P}^0\rangle = e^{-i\xi}|P^0\rangle$$



Since the phase  $\xi$  is arbitrary and  $\mathbf{M}$  and  $\mathbf{\Gamma}$  are Hermitian CP is conserved only if

$$\text{Im}(M_{12}^* \Gamma_{12}) = 0$$

or equivalently

$$|H_{12}| = |H_{21}|.$$

The evolution of the meson can be described in terms of the mass eigenstates which are the eigenvectors of  $\mathbf{H}$  and thus gives

$$\begin{aligned} |P_H\rangle &= p|P^0\rangle + q|\bar{P}^0\rangle \\ |P_L\rangle &= p|P^0\rangle - q|\bar{P}^0\rangle \\ |P_H(t)\rangle &= e^{-im_H t} e^{-\Gamma_H t/2} |P_H\rangle \\ |P_L(t)\rangle &= e^{-im_L t} e^{-\Gamma_L t/2} |P_L\rangle \end{aligned}$$

where  $|p|^2 + |q|^2 = 1$  and the ratio  $q/p$  is constrained by the diagonalisation of  $\mathbf{H}$ .  $H$  denotes the heavy state while  $L$  is used for the light one. The  $m_H$ ,  $m_L$ ,  $\Gamma_H$  and  $\Gamma_L$  terms are not eigenvalues of  $\mathbf{M}$  and  $\mathbf{\Gamma}$ . However,  $\mu_H = m_H - i/2\Gamma_H$  and  $\mu_L = m_L - i/2\Gamma_L$  are the eigenvalues of  $\mathbf{H}$ . Also  $\text{tr}\mathbf{M} = m_H + m_L$  and  $\text{tr}\mathbf{\Gamma} = \Gamma_H + \Gamma_L$ .

Another representation of the evolution is based on the flavour states and is the one used to describe the evolution of  $B^0$  mesons which are created in a flavour specific state at  $t = 0$ , either  $P^0$  or  $\bar{P}^0$ :

$$\begin{aligned} |P^0(t)\rangle &= f_+(t)|P^0\rangle + \frac{q}{p}f_-(t)|\bar{P}^0\rangle \\ |\bar{P}^0(t)\rangle &= \frac{p}{q}f_-(t)|P^0\rangle + f_+(t)|\bar{P}^0\rangle \end{aligned}$$

where

$$f_{\pm}(t) = \frac{1}{2} (e^{-i\mu_H t} \pm e^{-i\mu_L t}).$$

This representation is used to compute the decay width of the meson to different final states which are observable quantities.

Phenomenologically, there are two independent decay amplitudes which enter the description of the decay of the neutral meson system:

$$\begin{aligned} A_f &= \langle f|T|P^0\rangle \\ \bar{A}_f &= \langle f|T|\bar{P}^0\rangle \end{aligned}$$

As the physics must be invariant under the phase redefinitions, it turns out that the following four quantities have a chance to be observable:

$$\left| \frac{q}{p} \right|, |A_f|, |\bar{A}_f| \text{ and } \lambda_f = \frac{1}{\lambda_f} = \frac{q \bar{A}_f}{p A_f}.$$

After CP-conjugation we find out that the following relations hold only if CP is conserved:

$$\left| \frac{q}{p} \right| = 1, \quad (2.29)$$

$$|A_f| = |\bar{A}_{\bar{f}}|, \quad |A_{\bar{f}}| = |\bar{A}_f|, \quad (2.30)$$

$$\arg \left( \frac{p^2}{q^2} A_f \bar{A}_f^* A_{\bar{f}} \bar{A}_{\bar{f}}^* \right) = 0. \quad (2.31)$$

We can thus distinguish three different types of CP violation (of which more than one can be incorporated in a particular decay):

- CP violation in the mixing also called “indirect CP violation”, when Eq 2.29 does not hold;
- CP violation in the decay amplitudes on “direct CP violation”, when Eq 2.30 is not satisfied;
- CP violation in a phase mismatch between the mixing parameters and the decay amplitudes or “interference CP violation”, when Eq 2.31 does not hold.

The direct CP violation can be tested by the asymmetry in  $P^0$  decay into flavour-specific final states:

$$\begin{aligned} A_D &= \frac{N(P^0 \rightarrow f) - N(\bar{P}^0 \rightarrow \bar{f})}{N(P^0 \rightarrow f) + N(\bar{P}^0 \rightarrow \bar{f})} \\ &= \frac{|A_f|^2 - |\bar{A}_{\bar{f}}|^2}{|A_f|^2 + |\bar{A}_{\bar{f}}|^2}. \end{aligned}$$

The simultaneous effect of the indirect and direct CP violation can be tested by this asymmetry:

$$\begin{aligned} A_M &= \frac{N(\bar{P}^0 \rightarrow f) - N(P^0 \rightarrow \bar{f})}{N(\bar{P}^0 \rightarrow f) + N(P^0 \rightarrow \bar{f})} \\ &= \frac{|p/q|^2 |A_f|^2 - |q/p|^2 |\bar{A}_{\bar{f}}|^2}{|p/q|^2 |A_f|^2 + |q/p|^2 |\bar{A}_{\bar{f}}|^2}. \end{aligned}$$

Finally, if no direct and indirect CP violation are present, the interference CP violation can be tested by the asymmetry of the decay of the neutral meson to a CP eigenstate by:

$$\begin{aligned} A_{\text{CP}}(t) &= \frac{\Gamma(P^0(t) \rightarrow f) - \Gamma(\bar{P}^0(t) \rightarrow f)}{\Gamma(P^0(t) \rightarrow f) + \Gamma(\bar{P}^0(t) \rightarrow f)} \\ &= \frac{\text{Im} \lambda_f \sin(\Delta m t)}{\cosh(\Delta \Gamma t / 2) - \text{Re} \lambda_f \sinh(\Delta \Gamma t / 2)}. \end{aligned}$$

## 2.3 Flavour tagging

When looking more closely at how  $\beta$ , for instance, can be measured, we see that it can be derived from the decay rate asymmetry:

$$A_{B \rightarrow J/\psi K_S^0}(t) = \frac{\bar{R}(t) - R(t)}{\bar{R}(t) + R(t)} = \sin 2\beta \sin \Delta mt$$

with

$$R(t) = |\langle J/\psi K_S^0 | \mathcal{H}_W | B^0(t) \rangle|^2 \quad \bar{R}(t) = |\langle J/\psi K_S^0 | \mathcal{H}_W | \bar{B}^0(t) \rangle|^2$$

Practically this means we need to count how many  $B^0$ 's decay to  $J/\psi K_S^0$  and how many  $\bar{B}^0$ 's do the same thing in a given time interval after creation. The question here is *How do you know it was a  $B^0$  and not a  $\bar{B}^0$ ?* and the answer is *Flavour tagging*.

The flavour tagging is a process which tries to identify the flavour of the  $b$  quark in a given  $B$  hadron at production. Its answer is three fold  $b$ ,  $\bar{b}$  or “I don't know”. The presence of the later one gives more information than a random guess. Chapter 4 gives the detail on how the decision is made.

The correctness of this decision is very important. If we cannot distinguish the  $B$  and  $\bar{B}$ , the measured asymmetry will be null. The measured decay rates are related to the real ones by the following formulae which take into account the *wrong-tag fraction*  $w$  (assuming it is equal for both  $B$  and  $\bar{B}$  events):

$$\begin{aligned} \bar{R}^{\text{meas}}(t) &= (1 - w)\bar{R}(t) + wR(t) \\ R^{\text{meas}}(t) &= w\bar{R}(t) + (1 - w)R(t) \end{aligned}$$

And thus the measured asymmetry turns out to be diluted with respect to the real asymmetry:

$$A^{\text{measured}} = \frac{\bar{R}^{\text{meas}} - R^{\text{meas}}}{\bar{R}^{\text{meas}} + R^{\text{meas}}} = (1 - 2w) \frac{\bar{R} - R}{\bar{R} + R} = (1 - 2w)A.$$



# Chapter 3

## The LHCb Experiment

This chapter presents the LHC accelerator, which will provide the protons for the LHCb experiment. The LHCb experiment is then described as well as its triggering system. At the end of this chapter the reader will find a description of the simulation software of the experiment.

### 3.1 Large Hadron Collider

The next generation of circular accelerator at CERN will use hadrons such as the protons instead of the previously used electrons and positrons. This change is required to obtain an increase in energy because the energy loss of electrons through synchrotron radiation would be too high or require a circular accelerator much larger than LEP, which is 27 km in circumference.

This next step towards higher-energy is the Large Hadron Collider (LHC), which will replace LEP in the same tunnel. In addition to the reuse of the tunnel all the accelerator chain in figure 3.1 will be reused with minor modification to the injection system. The LINAC will feed protons of 50 MeV into the two Proton Synchrotron Booster (PBS) rings. These protons of

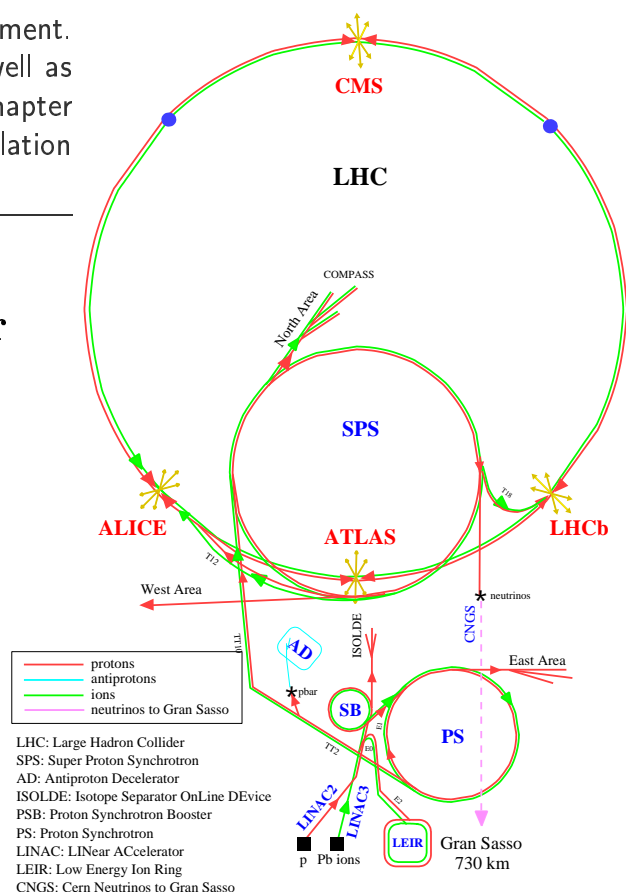


Figure 3.1: *The CERN accelerators facility.*

1 GeV are then accelerated up to 26 GeV in the Proton Synchrotron (PS) before being injected in the Super Proton Synchrotron (SPS) where they will reach an energy of 450 GeV. In the final step, they will reach the energy of 7 TeV in the LHC rings thus producing collisions of 14 TeV in the centre of mass frame, as explained in the next section.

While the main goal of the LHC is to provide the high energy and the high luminosity required for the search of the Higgs boson using p–p collisions, it will also be used to accelerate heavy ions like lead and calcium in order to study quark gluon plasmas (QGP) and thus almost “free” quarks. These capabilities are technologically challenging. A design closer to the LEP one, using protons and anti-protons, would have been easier to implement but the luminosity would not have reached what can be expected from the actual design because anti-protons are difficult to produce in large quantities. Moreover, heavy ion experiments would have required a dedicated accelerator in that case.

The LHC will host four main experiments. ATLAS and CMS are both classical multi-purpose experiments using a  $4\pi$  geometry. They are designed for the Higgs quest and physics beyond the Standard Model. The ALICE experiment is dedicated to QGP studies in the heavy ion collisions. Finally the LHCb experiment is mainly dedicated to the b-quark and CP violation studies.

### 3.1.1 Protons beams and their collisions

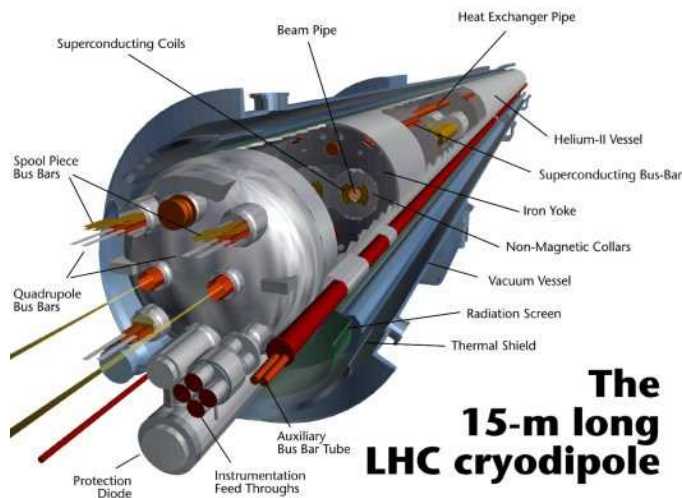


Figure 3.2: Section view of the LHC beam pipe.

small packets of protons (roughly  $10^{11}$  protons per bunch). The bunches travelling at almost the speed of light are spaced by 7.5 m or 25 ns which corresponds to a frequency of 40 MHz. In a ring of 27 km, 3564 bunches can be placed but the

In the LHC two beams of protons will cycle in opposite directions. In the LEP both electron and positron beams could use the same electric field for acceleration at the same time but with two proton beams, which don’t have opposite charge, separated accelerator cavities are required. The whole accelerator is thus made of two beam pipes, which joins together in eight interaction points (IP).

Unlike the electron beam in any television, high-energy beams such as the one of the LHC are separated into a series of *bunches* which are

LHC will only fill 2808. This is caused by the complex injection system used.

While all the 2808 bunches can collide at IP1 and IP5 where ATLAS and CMS are located, in IP8, where LHCb is placed, only 2652 bunch crossings are possible. This is due to the position of LHCb, 1/8 of a cycle out of phase combined with an additional displacement of 11.2 m which was required to fit the detector in the already existing location of the Delphi experiment at LEP.

While ATLAS and CMS both require the highest possible luminosity of  $10^{34}\text{cm}^{-2}\text{s}^{-1}$  from the machine, LHCb will only require  $2 \cdot 10^{32}\text{cm}^{-2}\text{s}^{-1}$ , which is obtained by an ad hoc tuning of the beam focus at the interaction point. LHCb uses a lower luminosity to reduce the number of collisions per bunch crossing. With the maximal luminosity, an average of 17.4 collisions are expected per bunch crossing (from the extrapolated inelastic cross-section of proton-proton collision based on UA1, DØ and CDF data). The decay of b particles being identified by their time of flight, events with a unique primary vertex are preferred. So the luminosity is reduced to get an average of 0.37 collision per bunch crossing. Overall, the effective interaction rate will be around 11 MHz ( $40\text{ MHz} \cdot \frac{2652}{3564} \cdot 0.37$ ).

### 3.1.2 b quarks and the LHC

At the time of this writing, the parameters of hadronic b quark production at  $\sqrt{s} = 14\text{ TeV}$  are only known by extrapolation from SPS and Tevatron data. Estimates of the cross section  $\sigma_{b\bar{b}}$  give a range of 175 to 950  $\mu\text{b}$ , which lead to a common value used by all the LHC experiments of 500  $\mu\text{b}$ .

Cross section			
Total	$\sigma_{\text{tot}}$	100	mb
Inelastic	$\sigma_{\text{inel}}$	55	mb
$c\bar{c}$	$\sigma_{c\bar{c}}$	3.5	mb
$b\bar{b}$	$\sigma_{b\bar{b}}$	500	$\mu\text{b}$

Table 3.1: *Cross sections assumed for the LHC experiments.*

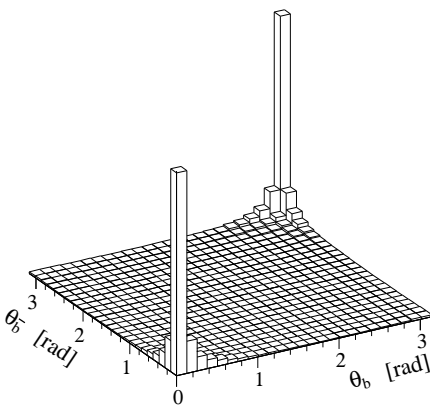


Figure 3.3: *Polar distribution of the b- and  $\bar{b}$ -hadrons at LHC.*

In p-p collisions the b  $\bar{b}$  quarks are mostly produced by a mechanism called “gluon fusion” where two or more gluons radiated by the protons’ partons interact together and convert into a pair of quarks. The momentum distribution of these quarks is almost flat in rapidity, which means it’s peaked around the beam direction. Figure 3.3 gives the polar distribution of the two quarks.

This particular distribution requires a detector specifically designed to cover the low polar angle region. For this reason the LHCb experiment looks like a fixed target experiment.

## 3.2 The LHCb detector

The LHCb experiment is dedicated to the study of b-hadron decays and CP violation. For this purpose it was designed as a single arm spectrometer. It covers the region from 35 mrad up to 300 mrad in the bending plane of the magnet (only 250 mrad in the vertical plane). Its distinctive features are:

- a high-resolution microstrip vertex detector for the identification of secondary vertices and precise proper-time measurements,
- a complex trigger system, able to trigger on both hadronic and leptonic b decays with a recognition of the vertex topology,
- a precise particle identification widening the range of accessible multi-particle final states.

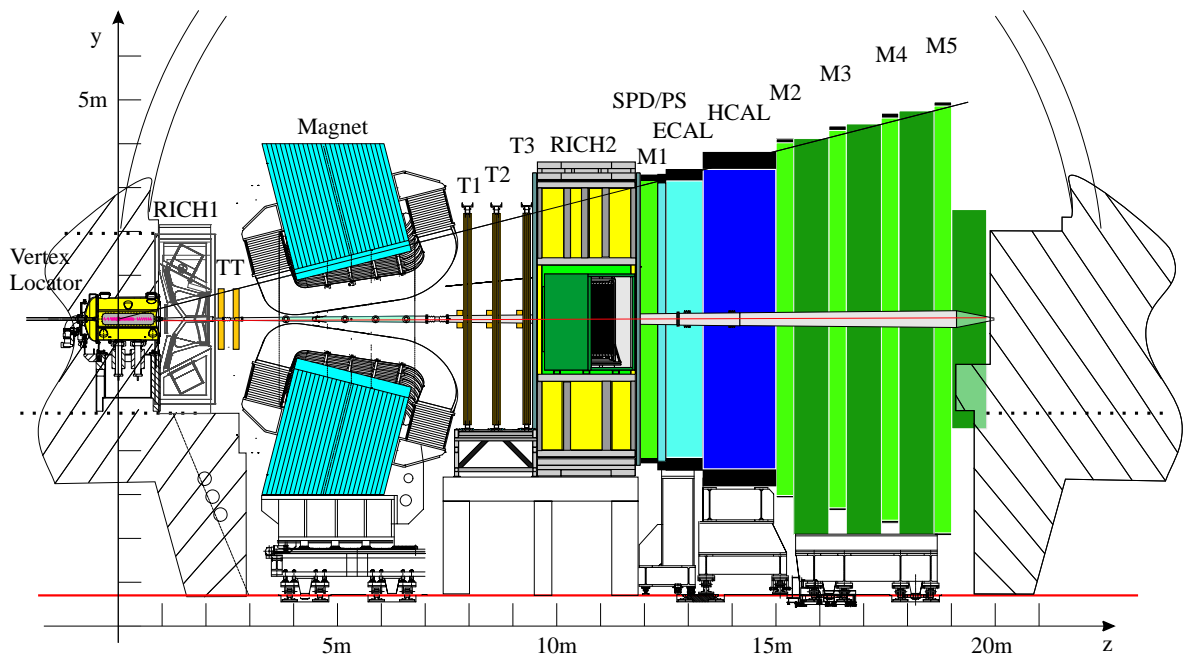


Figure 3.4: Side view of the LHCb detector in its latest “light” design.



Figure 3.4 shows the different sub-detectors of the whole spectrometer. From left to right, we have:

- the vertex locator (VELO),
- the upstream ring-imaging Cherenkov detector (RICH1),
- the magnet,
- the tracking system (TT & T1-T3),
- the downstream RICH detector (RICH2),
- the preshower (SPD/PS),
- the electromagnetic calorimeter (ECAL),
- the hadronic calorimeter (HCAL),
- the muon detector (M1 . . . M5).

The beam pipe crosses all the detector but the VELO, which is inside a vacuum vessel connected to the beam pipe.

The following subsections present briefly the subdetectors based on the Technical Design Report (TDR) descriptions.

### 3.2.1 The VELO

Vertex reconstruction is a fundamental requirement for the LHCb experiment. Displaced secondary vertices are a distinctive feature of b-hadron decays. The VERtEX LOCator (VELO [26]) has to provide precise measurements of track coordinates close to the interaction region. These are used to reconstruct production and decay vertices of beauty- and charm-hadrons, to provide an accurate measurement of their decay lengths, and to measure the impact parameter of particles used to tag their flavour. The VELO measurements are also a vital input to the second-level trigger (L1), which enriches the b-decay content of the data.

The VELO features a series of silicon stations placed along the beam direction. They are placed at a radial distance from the beam, which is smaller than the aperture required by the LHC during injection, and must therefore be retractable. This is achieved by mounting the detectors in a setup similar to Roman pots (Fig. 3.5). Due to the movements of the detector before and after the injection phase misalignments of the stations are possible and corrected by a software table updated at the beginning each run.

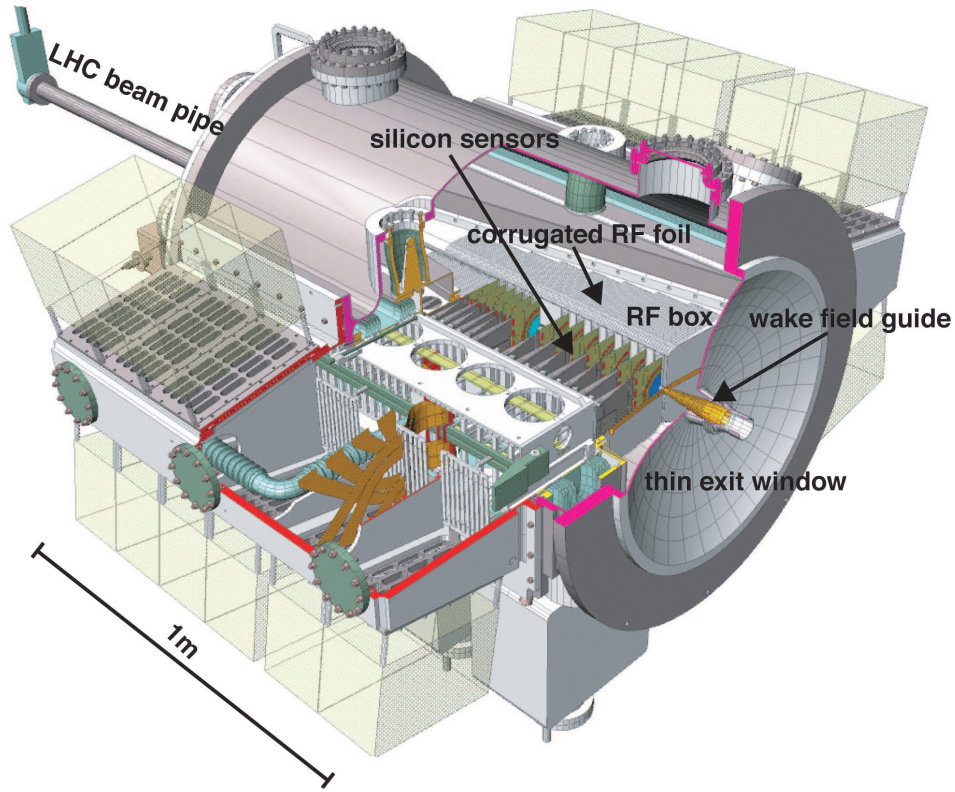


Figure 3.5: 3D view of the VELO TDR prototype with 25 stations.

The VELO stations are placed in a secondary vacuum separated from the beam vacuum by an RF shield. It also protects the sensors and electronics from electromagnetic noise induced by the beams themselves. This shielding is thin ( $\approx 100 \mu\text{m}$ ) and specially shaped to reduce the multiple scattering, which is the main source of background for the Level-1 trigger.

The vertex detector is made of 21 parallel disk-shaped silicon strip detectors. Figure 3.6 shows the stations placement. The previous design used 4 more stations but they were removed to reduce the cost and the amount of material seen by the particles. It almost doesn't change the physical performance of the detector itself.

Each station is made of two  $r$  and two  $\phi$  sensors. This simplifies a lot the track reconstruction done by the Level-1 trigger. Tracks from B events turn out to have a high impact parameter in the  $Orz$  plane. This allows to use a two-dimensional reconstruction of all the tracks in this plane followed by a 3D reconstruction of the most important tracks only giving a valuable gain in CPU time. Also the VELO is far enough from the magnet to have only straight tracks.

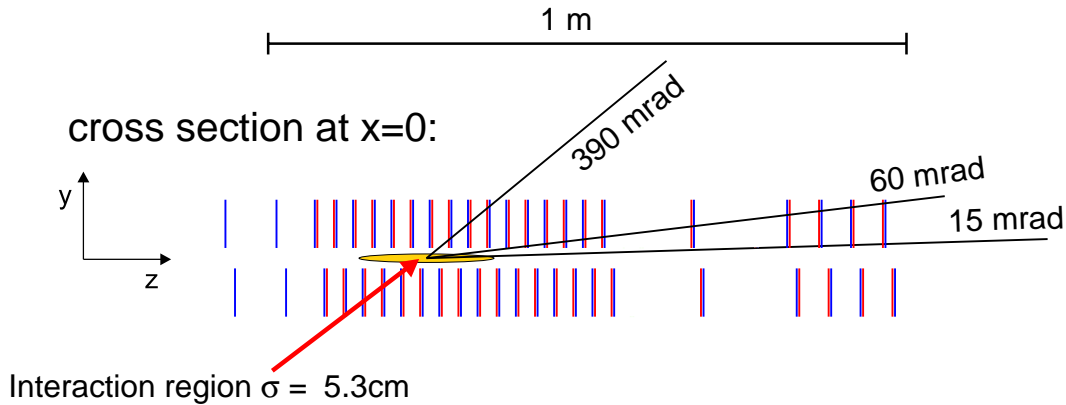


Figure 3.6: *Cross-section view of the VELO TDR design along the beam axis.*

Figure 3.7 shows the two base sensors used in a station. They have an inner active radius of 8 mm due to LHC machine constraint and an outer radius of 42 mm imposed by the magnet acceptance. They are made from  $220\ \mu\text{m}$  thick  $n$ -on- $n$  single sided silicon wafers. The strip pitch of the  $r$  sensor increases with the radius from 40 to  $92\ \mu\text{m}$ . The  $\phi$  sensor has a pitch increasing from 37 to  $98\ \mu\text{m}$  with a  $10^\circ$  to  $20^\circ$  stereo angle. Both cover  $182^\circ$  allowing an overlap to cover completely the acceptance.

The spatial resolution depends on the number of tracks but in average it is of  $42\ \mu\text{m}$  along the beam axis and  $10\ \mu\text{m}$  in the transverse direction.

The precision on the decay lengths will range from 220 to  $370\ \mu\text{m}$ . This corresponds to almost a resolution of 40 fs on the B proper time of flight.

The readout of the detectors is done by 16 chips per sensor. Data are kept

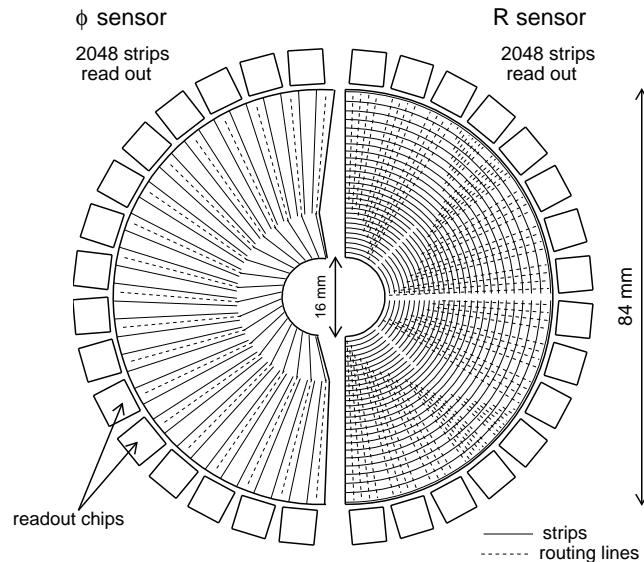


Figure 3.7: *Schematic view of the  $\phi$  and  $r$  silicon sensors. The  $\phi$  sensors strips have a stereo angle to resolve ambiguities.*

in the analog pipeline of the chips for up to 4  $\mu\text{s}$  until the L0 trigger decision is received. Then 32 readout line are serialised through a analogue link of 60 meters up to the radiation free area where the L1 electronics will check the data integrity, digitise the signals, perform a zero-suppression and find clusters before sending the results to the L1 trigger. Once accepted by the L1 trigger the data will also be sent to the High Level Trigger and subsequently to storage.

### 3.2.2 The RICH

Particle identification in LHCb is provided by two Ring Imaging Cherenkov detectors (RICH [27]). High momentum particles (up to  $\sim 100 \text{ GeV}/c$ ) are identified by the RICH 2 detector, situated downstream of the spectrometer magnet. Lower momentum particles, up to about  $60 \text{ GeV}/c$ , are identified by the RICH 1 detector, located upstream of the magnet.

The Cherenkov effect is used to achieve a good  $K-\pi$  separation. This is required to distinguish correctly the  $B \rightarrow K\pi$  and  $B \rightarrow \pi\pi$  channels for instance and it is also important for “kaon tagging”, as will be explained later.

The RICH detects ring images formed by the Cherenkov photons emitted along the track of charged particles traversing the detector. The image is captured by pixelated Hybrid Photon Detectors (HPDs). Due to the sensitivity of photomultipliers to magnetic field, the HPDs are placed above and below the detector and a shielding has been devised to reduce the magnetic field to less than 1 mT.

RICH 1 includes two radiators. A 5 cm-thick block of aerogel with a refractive index of  $n = 1.03$  for kaon identification above  $2 \text{ GeV}/c$  and  $\pi$ -K separation up to  $\sim 10 \text{ GeV}/c$ . The second radiator is made of  $\text{C}_4\text{F}_{10}$  with  $n = 1.0014$ .

The RICH 2 uses a single radiator of  $\text{CF}_4$  ( $n = 1.0005$ ) and covers high momentum (12–150 GeV), low angle tracks (15–120 mrad).

### 3.2.3 The magnet

The magnetic field used by the spectrometer is produced by a magnet made of 9 km of aluminium conducting wires inside a 120 kt steel plate yoke [28]. The magnetic field is produced along the y axis (vertical) and has a maximal intensity of 1.1 T. The inner size of the magnet defines the acceptance of the experiment, which is 300 mrad in the horizontal (bending) plane and 250 mrad in the vertical plane.

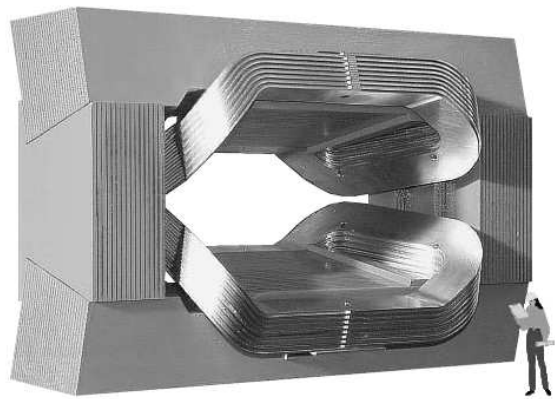


Figure 3.8: *The LHCb magnet.*

A classic warm magnet was chosen instead of a super-conducting one in order to be able to reverse the magnetic field to compensate for left-right asymmetry with a still reasonable cost.

### 3.2.4 The tracker

The tracking system or tracker provides the momentum measurement of the charged particles and the needed information to link to the hits in the calorimeters and muon chambers as well as seeds for the RICH detectors.

The tracker has been drastically reduced from the nine stations present in the TDR [2, 29, 30] to four station to reduce the radiation/nuclear interaction length. The first station called TT is placed right behind the RICH 1 and three more stations are placed after the magnet, just before the RICH 2.

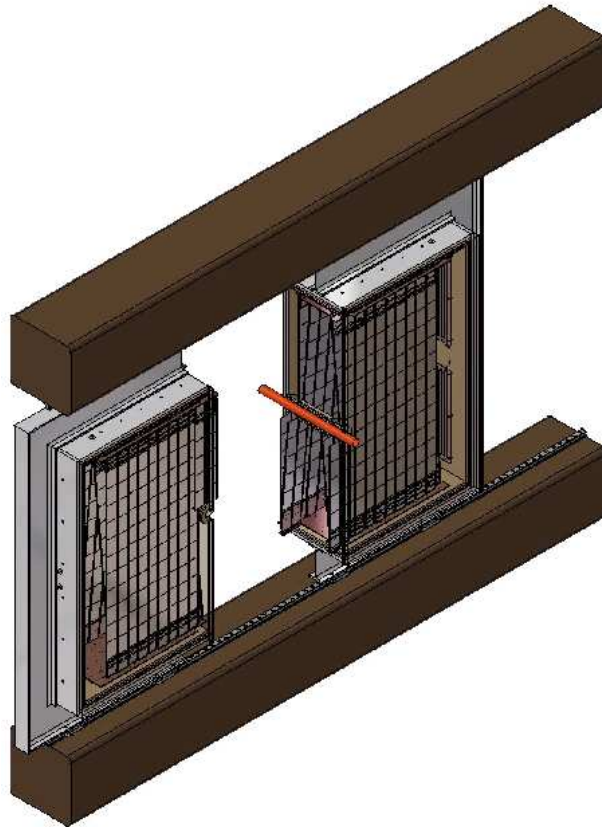


Figure 3.9: *The TT tracking station, opened with downstream wall removed to show the sensors.*

The TT tracking station plays two roles at a time. It's used to reconstruct low momentum tracks that are bent out of the acceptance of T1-T3. And it's also used by the Level-1 trigger to assign a transverse-momentum to large-impact parameter tracks.

TT is made of four layers of silicon micro-strip detectors. They are arranged in two pairs separated by 30 cm. The first and fourth layer have vertical strip ( $x$  layers) while the second and third have a stereo angle of  $+5^\circ$  ( $u$  layer) and  $-5^\circ$  ( $v$  layer) respectively.

The remaining three stations T1, T2 & T3 are split in two parts, the Inner Tracker and Outer Tracker. This separation is made to optimise cost and efficiency due to the track density, which roughly follows a  $1/r^2$  relation. The inner tracker occupies only 1.3% of the sensitive area of a tracking station, but approximately 20% of the charged particles produced close to the interaction point pass through this area.

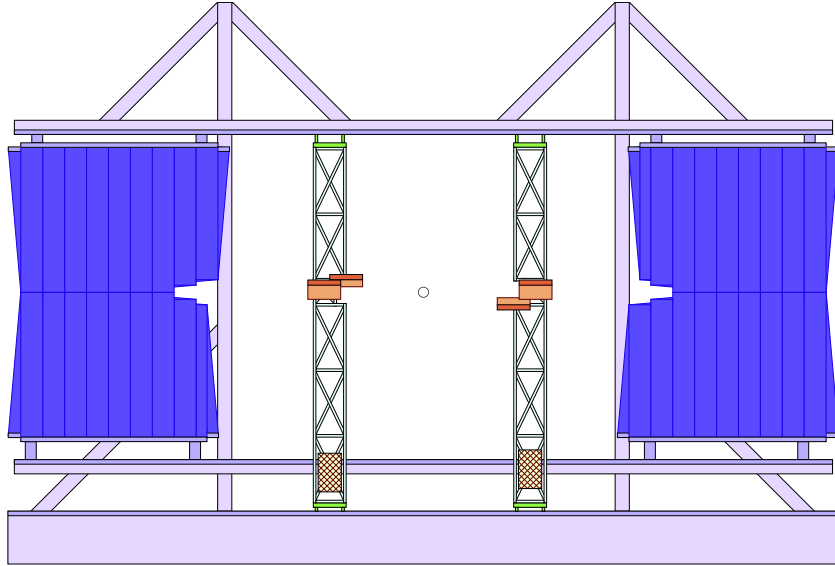


Figure 3.10: *Front view of an opened tracking station showing the beam pipe in the middle, the inner tracker boxes and then the outer tracker straw tubes on the outside.*

The inner tracker [30] will be made of  $410\ \mu\text{m}$  thick single-sided  $p$ -on- $n$  silicon micro-strip sensors arranged in a cross-like shape. Similarly to the TT station it will be made of two  $x$  layers and two stereo layers ( $u$  and  $v$ ). Each station is split in four boxes containing the four detection planes. Each sensor contains 384 readout strips with a pitch of  $198\ \mu\text{m}$  and a length of 108 mm.

The outer tracker [29] is made of drift cells called straw tubes. The drift gas

is an Ar/CF<sub>4</sub>/COF<sub>2</sub> mixture, which optimises the drift speed. The total drift, amplification and transmission time is kept slightly below 50 ns. Due to the minimal interval of 25 ns between two bunch crossing, it can happen that two events are piled-up in the outer tracker.

Like the rest of the tracking system, the outer tracker uses two  $x$ -layers, one  $u$ -layer and one  $v$ -layer. This global choice of two layers in the bending plane is governed by the requirement of an average momentum resolution of  $\delta p/p < 0.4\%$ .

### 3.2.5 The calorimeters

The calorimeters [31] are used to identify photons, electrons and hadrons and measure their position and energy. They also provide the input to the Level-0 trigger. As the L0 trigger rate is 40 MHz the detector read-out must be fast. A compromise was thus chosen between a small number of read-out channels, a low occupancy and a reasonable energy and position resolution. Finally a binary read-out has been chosen to full-fill the trigger requirements.

The calorimeters are split in four sub-detectors:

**SPD** a Scintillator Pad Detector plane is used to reduce the background of the high  $E_T$   $\pi^0$  tail in the electron trigger,

**PS** a PreShower for the rejection of the high background of charged pions,

**ECAL** the Electromagnetic CALorimeter, which measures the energy of the photons and the electrons, and

**HCAL** the Hadronic CALorimeter, which does the same thing for the hadrons.

The SPD and the PS are put on either sides of a 12 mm thick lead wall and are made of 15 mm thick scintillator pads. The scintillation light is driven through wavelength shifting (WLS) fibres to the multi-anode photomultipliers, which are located above and below the detector. With this structure about 25 photoelectrons on average are produced for each minimum ionising particle thus giving a clean separation between electrons and photons.

The ECAL uses the “shashlik” technology with lead as the absorber material. It’s segmented into three resolution zones in order to optimise the  $\pi^0$  resolution.

Finally, the HCAL uses 16 mm thick iron and 4 mm thick scintillating tiles parallel to the beam. The scintillation light is converted from UV to visible light by scintillating dopant and then driven from the end of the tile to the photomultipliers by WLS fibres.

### 3.2.6 The muon detector

Muons are the charged particles with the lowest interaction probability. They are easily distinguished from the other particles simply by using a large shield. In LHCb, the shield is made of the whole calorimeter system plus four layers of steel. Figure 3.11 shows the five muon stations and the steel shielding, the calorimeter would be placed between M1 and M2 [32]. The M1 station is used to measure the  $p_T$  of the tracks found in M2-M5 and to cross-check the calorimeter information in the L0-trigger.

Each station is made of multiple wire proportional chambers (MWPC).

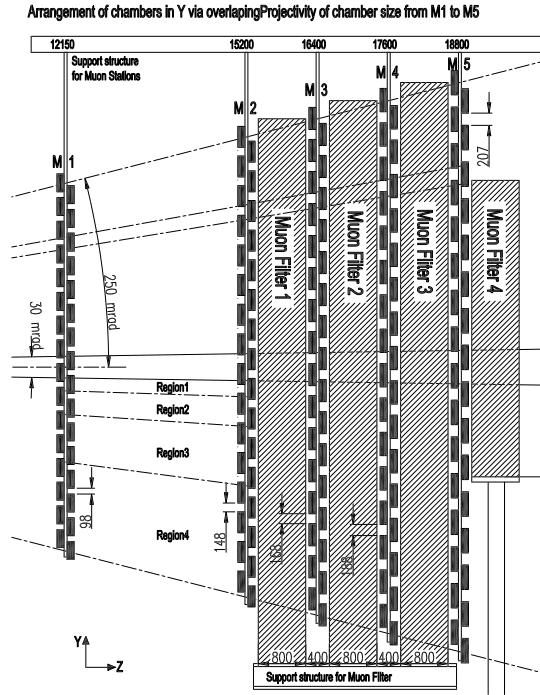


Figure 3.11: Side view of the muon detector.

### 3.3 The LHCb trigger

Due to the small cross-section of the  $b\bar{b}$  pair production compared to the inelastic scattering of protons very few bunch crossings give birth to interesting events in the LHCb detector. In order to avoid wasting resources to acquire useless events a complex triggering system was developed to reduce the data taking rate from the 40 MHz bunch crossing rate down to a reasonable level [33].

The trigger is split in a series of levels which gradually reduce the data rate:

- L0** The Level-0 reduces the event rate to  $\sim 1$  MHz. This is done by four high- $p_T$  triggers and a pile-up veto. (The low luminosity and the bunch structure reduce the rate of visible interactions to only once per 100 ns in average.)

The L0 trigger has a fixed latency of  $4 \mu\text{s}$ , which imposes a buffering of the data in the front-end chips themselves. The four high- $p_T$  triggers are the following, for which we indicate the nominal threshold values:

**The electron trigger** combines information from the M1, the preshower and the ECAL looking for high  $E_T$  electrons. The event is accepted if  $E_T > 2.8 \text{ GeV}$ .



**The photon trigger** looks like the electron trigger but uses M1 as a veto. To be accepted the  $E_T$  must be bigger than 2.6 GeV.

**The hadron trigger** uses the HCAL, the preshower and M1, accepting events with a hadron of  $E_T > 3.6\text{GeV}$ .

**The muon trigger** reconstructs tracks with M1 to M5 and checks for a compatibility with the hypothesis of a high  $p_T$  muon coming from the vertex region. The  $E_T$  must be greater than 1.1 GeV for single muon or 1.3 GeV for more muons.

On average 20% of the events with at least one visible interaction contain two or more visible interactions. As these events are more difficult to analyse and could easily be mis-identified as B events they are vetoed by two dedicated stations in the VELO. These two stations use only  $r$ -sensors and a binary readout in order to follow the high throughput required by the trigger. The  $z$  intercept of the tracks reconstructed from these detectors in the  $r - z$  plane are histogrammed and if more than one peak is present the height of the second highest peak is used to possibly reject the event.

**L1** The Level-1 trigger is a topology trigger which looks for detached secondary vertices. For this purpose it uses the information collected from the VELO sub-detector and uses the following processing steps:

**2D reconstruction:** Using only the  $r$ -sensors, triplets of hits in consecutive stations are formed within the same octant and are then extended to more stations. This set of 2D tracks in the  $r - z$  plane are used as input to the next step.

**Primary vertex finding:** Intersection of the 2D tracks with the beam axis are histogrammed and a peak search is applied to find primary vertex seeds. If more than one seed is found the event is discarded (L1 pileup-veto). A fitting procedure is then applied to refine the primary vertex position.

**High IP tracks reconstruction in 3D:** The impact parameter (IP) with respect to the primary vertex of the 2D tracks is computed. Tracks with an IP between  $150\ \mu\text{m}$  and  $3\ \text{mm}$  as well as tracks matching with an L0 object (calorimeter hit or muon) are then reconstructed in 3D. These 3D tracks are matched against L0 object to improve the ghost rejection. Finally the 3D tracks are extrapolated to TT to get an estimate of the  $p_T$ . Events are accepted based on a cut in the plane defined by the sum of the logarithm of the two highest  $p_T$ s and the sum of the logarithm of their respective impact parameter. In addition to this cut a "bonus"

system is used to increase the chance to accept specific channels. This bonus is based on dimuon invariant mass, high  $E_T$  photon and electron.

The different cuts are tuned to reduce the event rate of the L0 accepted events from 1 MHz down to 40 kHz.

**HLT** The High Level Trigger is the most CPU consuming part of the trigger. It can be split in four distinct operations:

- A Confirm the Level-1 algorithm, but using T1–T3 to improve the momentum resolution. This will quickly reduce the event rate to 20 kHz.
- B Full pattern recognition of long tracks and lepton identification but no RICH information is used.
- C Exclusive selection of channels. The goal is to get the highest possible efficiency for the channels considered as the most important for the physics goals.
- D Inclusive selection of channels. More general criteria are used here to select a large quantity of interesting channels without the need of a lot of exclusive reconstruction.

The final event rate which need to be transfered for permanent storage will be around 200 Hz.

In summary, LHCb’s trigger system will manage the reduction of the huge amount of data produced by the detector to a reasonable amount for final storage. Without the whole trigger a throughput of 40 TB/s would have been required. The Level-0 already reduces this to 1 TB/s and the Level-1 squeezes it to a manageable 4 GB/s. Finally the HLT lets a mere 40 MB/s go out to tape.

### 3.4 Monte Carlo and analysis programme

In modern physics the complexity of the experiments and the large amount of data requires a large effort on computing facilities and the relevant software. In LHCb as in any other experiment, the computing group has to prepare the tools needed for both the design phase and the final physics studies.

Figure 3.12 shows the structure of the software used and the data flow between the logical blocks. The *generator* simulates the collisions of two protons and thus “generates” the particles that the rest of the software will consider. The *simulation* emulates as much as possible the response of the real detector which is figured by the *detector* block. Finally the digitised information coming out of either the simulated or the real detector feeds the *reconstruction* which builds up a synthetic

view of the event. The *analysis* then uses this information to extract physics parameters.

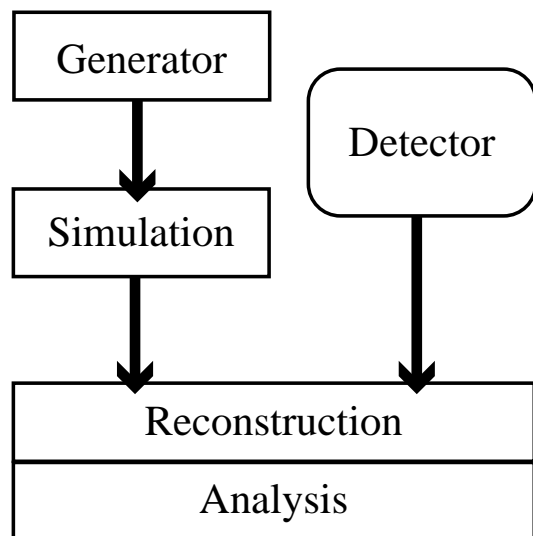


Figure 3.12: *Block diagram of the structure of LHCb's software.*

distributions obtained with the real data. This allows the extraction of parameters which are not directly observable.

Today (October 2003), the LHCb experiment mainly exists only in simulation. This software has been split in two parts, the simulation, which uses Monte Carlo techniques, and the reconstruction, which must be reusable as is with the real data.

During the detector design phase, the understanding of the results of the reconstruction are fundamental. This understanding requires that one might follow the particles through all the steps of the simulation and further on through the reconstruction. These data about what really happened at all the stages is simply called the “truth”.

The LHCb experiment uses two main languages right now. The FORTRAN, which is inherited from the past, and the C++, which has been chosen as the best successor to fulfil the ever growing needs imposed by the amount of data collected. In LHCb, the C++ software makes use of the Gaudi framework [34]. Collaboration with the CERN GRID project is also important for the future storage and analysis of the data.

During the development phase the rounded box in figure 3.12 does not exist and all the other boxes see a lot of changes. These changes both happen due to evolving choices in the software technology used and because the detector design improves as well as the precision of its simulation. As the goal is to choose the best possible detector design, many different ways have to be explored. Also writing a perfect simulation of all the detector is a very long job and is thus only done by an iterative procedure.

Once the real detector is built and operational the rounded box can be connected to the rest of the diagram. At this point the simulation is used to produce reference distributions based on some parameters, which are then compared to the

### 3.4.1 Generation & simulation

The left part of figure 3.12 has to simulate:

- the proton-proton collision physics or “generation”,
- the trajectories of the particles produced by the collision as well as their decays,
- the interaction of the particles with the matter which constitute the detector,
- the detector response to these interactions and any intrinsic noise,
- the pileup signal produced by previous collisions.

In LHCb, all this is done in FORTRAN but the last point. Currently the software is being rewritten in C++ for better integration. The FORTRAN version is called SICBMC and integrates a few software packages:

**PYTHIA 6** [35] is responsible for the p-p collision only.

**QQ** [36] takes care of the decay of the particles produced by PYTHIA.

**GEANT 3** [37] does the complicated job of propagating the particles through the detector and computing the interaction with its matter. It uses QQ when it needs to decay a particle.

Efforts are underway to replace the simulation part done by GEANT 3 with a new C++ version based on its object oriented successor GEANT 4. This new part is named Gauss inside LHCb. The digitisation phase of the simulation (which is mainly done at the time of the reconstruction, right now) will be moved into the Boole package. The reconstruction is also the only part of the simulation which is already in C++.

### 3.4.2 Reconstruction & analysis

In the case of a particle such as a charged pion, the *reconstruction* is the complicated job of associating the hits registered by the sub-detectors to form the *track* and then adding information from the RICH and calorimeters to identify this particle and finally give it a momentum and a charge.

Associating hits together is rather complicated especially because some hits along tracks might be missing and also some more hits can exist which are just electronic noise. In LHCb different kinds of tracks can be reconstructed depending on what information is available. Ideally, we would get only *long* tracks with enough hits throughout the whole detector. But  $K_S^0$  can fly far enough before they

decay into two pions such that these two tracks do not leave hits in the VELO. These tracks are called *downstream* tracks. So some shorter tracks need to be reconstructed which do not leave enough hits in the VELO. Also particles with a low momentum could be bent out of the acceptance of the T1–T3 stations. This is one more kind of short tracks called *upstream* tracks. Finally, tracks with low polar angles can be seen only by T1–T3 and are called *T* tracks.

The reconstruction job is done by the package called Brunel [38]. It receives raw hits and digitises them. Then it proceeds to the reconstruction and finally gives out “ProtoParticle”s. These objects are summaries of all the information collected by the reconstruction algorithm and most probably related to a single particle.

In the last phase, the analysis, the ProtoParticles are used to create “Particles” which are defined by a condensed set of information and reflect a clear choice on the particle identification. The analysis is done in a framework called DaVinci [39] which contains a lot of small packages. These tools are useful to the physicist to ease the writing of channel selection algorithms and for subsequent physical information extraction.



# Chapter 4

## Flavour tagging

---

The following chapter describes the strategies used by the LHCb experiment to determine the flavour of the B mesons at their production time. It is shown that multiple strategies are required to obtain a reasonable level of efficiency.

---

Many physics CP violation studies imply the measurement of the decay asymmetry between a particle and its anti-particle. In LHCb, physicists are interested in the asymmetry of the neutral B meson (both  $B_d$  and  $B_s$  decays). For instance, for a given decay final state  $f$  (for example a CP eigenstate like  $J/\psi K_S^0$ ) and after a proper time  $t$ , we are interested in:

$$A_{\text{CP}}(t) = \frac{N_{\bar{B}^0 \rightarrow f}(t) - N_{B^0 \rightarrow f}(t)}{N_{\bar{B}^0 \rightarrow f}(t) + N_{B^0 \rightarrow f}(t)}.$$

where  $t$  is the proper time elapsed between the neutral B production and its decay to  $J/\psi K_S^0$ .

When the interesting B decay is observed, we need to know if it was produced as a  $B^0$  or a  $\bar{B}^0$ . This information must be obtained from the rest of the event and this is the job of the *flavour tagging*.

Here we assume that the b quarks are produced by flavour conserving reactions (e.g.  $g+g \rightarrow b\bar{b}$ ). The tagging can be done by identifying the b hadron containing the other b. This is what we call *opposite-side* tagging. Also, the b quark in the meson is not alone. Similarly to what happened to the b and  $\bar{b}$  quark, the quark which comes along in the meson has a brother nearby who can also help in the tagging process. We will refer to this procedure as *same-side* tagging.

## 4.1 Flavour tagging signatures

Let's start by looking at the history of the other b quark in its hadron. When the b hadron decays one of its decay products carries an electric charge, which can be a signature of the b quark charge, and thus allows to distinguish between the quark and the anti-quark. In the following sections we will see that it's indeed possible to distinguish this particular particle from the other decay products based on kinematical criteria. Even when such a distinction is not possible, a partial reconstruction of the b hadron can give valuable information under the form of the "probable" charge of the hadron. Globally, the techniques consisting in an examination of the other b quark are called *opposite-side tagging*.

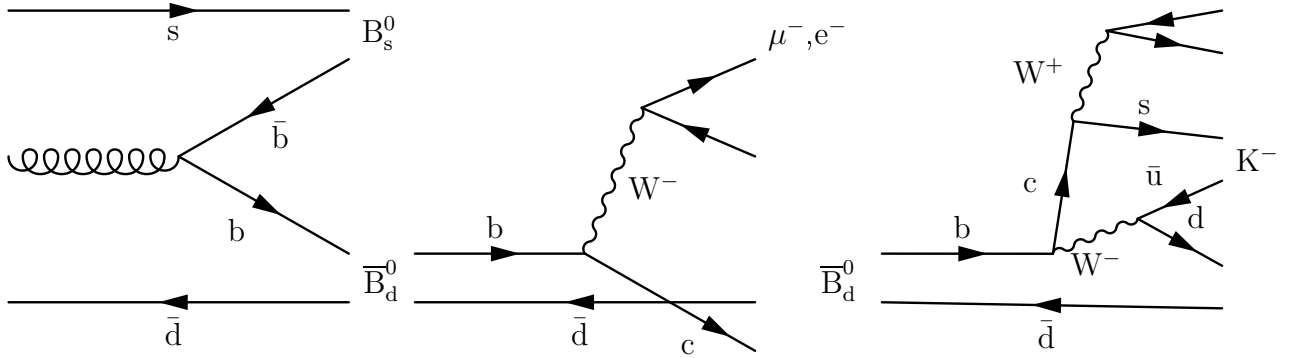


Figure 4.1: *Opposite side tagging signatures. Explanations in the text.*

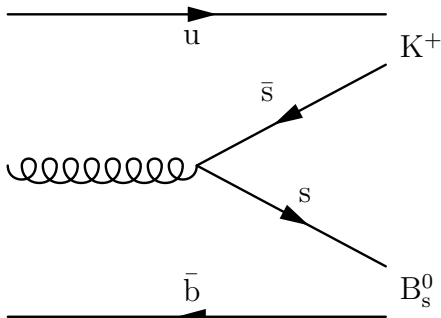


Figure 4.2: *Example of the production mechanism of a same-side tagging signature.*

On the left of Figure 4.1 a  $B_s^0$  is produced and needs to be tagged. The other b quark has formed a  $\bar{B}_d^0$ . The b quark will decay through a  $W^-$ , which can produce a lepton (in the middle) which is a good signature. Another outcome of the  $\bar{B}_d^0$  decay is presented on the right. The  $W^-$  creates a pair of quarks which are generally unusable for tagging but the decay of the c quark can be used. The s quark produced by this decay will create a kaon which can be used for tagging if it is charged.

Another possibility is illustrated in Figure 4.2, still relying on the fact that particles are always created with their anti-particle. In this case we look at the particle which was created at the same time as the quark which is the companion of the b quark in the B meson. For instance in a  $B_s^0$  we have a  $\bar{b}$  and a s quarks. The s quark was produced with a  $\bar{s}$



quark. The hadronisation phase has almost certainly used this  $\bar{s}$  quark to form a kaon. The goal is thus to find a kaon when we have a  $B_s$  or pion when it's a  $B_d$ . This technique is called *same-side* tagging.

In the rest of this chapter, the B meson under study is called *signal* B. The particle which carries the information about its flavour (kaon, muon or electron) will be called the *tagger*. The b hadron formed with the opposite side b quark will be called the *companion*.

As one can see from Figures 4.1 and 4.2, in the opposite-side tag, a  $K^-$  indicates the presence of a  $B_s^0$ , while it is a  $K^+$  in the same-side tag. One has to take into account this fact for a correct charge assignment.

Finally, the tagging implies a decision about whether we are in presence of b or  $\bar{b}$  quark. When no tagger is available, it's better to clearly say so because a random selection would dilute the physics information. In that case the tagging procedure will assign a null decision to the event, with a *none* tag.

## 4.2 Tagging power characterisation

The selection of particles to decide what is the flavour of the B hadron relies on a set of cuts which need to be optimised. For this purpose it is useful to have a single value, characterising to quality of the tagging, to maximise.

As mentioned in section 2.3, the measured asymmetry is diluted by the wrong tag fraction. However, the tagging efficiency in itself is also important (no tags means no mistake but it also means no physics). The best available combination of the tagging efficiency and the dilution arises when looking at the statistical uncertainty of the real asymmetry:

$$\mathcal{A} = \frac{\mathcal{A}^m}{1 - 2w} \Rightarrow \sigma_{\mathcal{A}} = \frac{\sigma_{\mathcal{A}^m}}{1 - 2w}$$

$$\mathcal{A}^m = \frac{R^m - \bar{R}^m}{R^m + \bar{R}^m} \Rightarrow \sigma_{\mathcal{A}^m}^2 = \left( \frac{\partial \mathcal{A}^m}{\partial R^m} \right)^2 \sigma_{R^m}^2 + \left( \frac{\partial \mathcal{A}^m}{\partial \bar{R}^m} \right)^2 \sigma_{\bar{R}^m}^2$$

$$\sigma_{\mathcal{A}^m}^2 = \left( \frac{2\bar{R}^m}{(R^m + \bar{R}^m)^2} \right)^2 R^m + \left( \frac{-2R^m}{(R^m + \bar{R}^m)^2} \right)^2 \bar{R}^m = \frac{4R^m \bar{R}^m}{(R^m + \bar{R}^m)^3}$$

At this point one should note that

$$1 - \mathcal{A}^{m2} = \frac{4R^m \bar{R}^m}{(R^m + \bar{R}^m)^2}$$

and thus

$$\sigma_{\mathcal{A}^m}^2 = \frac{1 - \mathcal{A}^{m2}}{R^m + \bar{R}^m} = \frac{1 - \mathcal{A}^{m2}}{N^m} = \frac{1 - \mathcal{A}^{m2}}{\epsilon N}$$

where  $N^m$  is the number of event tagged,  $\epsilon$  is the tagging efficiency and  $N$  the number of collected events. When combining everything together to get the statistical uncertainty on the real asymmetry, we get:

$$\sigma_{\mathcal{A}} = \frac{\sqrt{1 - \mathcal{A}^{m2}}}{\sqrt{N}\sqrt{\epsilon}(1 - 2w)} \propto \frac{1}{\sqrt{\epsilon}(1 - 2w)}$$

which clearly states that we need to maximise the *effective tagging efficiency* (or tagging power):

$$\epsilon_{\text{eff}} = \epsilon(1 - 2w)^2.$$

Annexe A gives the detailed computation of the statistical error on the effective tagging efficiency.

During the development phase of the experiment, the two parameters appearing in this formula are determined by counting how many tags of the different kind are produced and by comparing them with the Monte Carlo truth. For the tagging this means we have to compare the tagging decision with the flavour of the generated B meson. That way we have:

$$\text{The tagging efficiency } \epsilon = \frac{\#\text{right} + \#\text{wrong}}{\#\text{right} + \#\text{wrong} + \#\text{none}}.$$

$$\text{The wrong-tag fraction } w = \frac{\#\text{wrong}}{\#\text{right} + \#\text{wrong}}$$

When the experiment will run on real data, the wrong-tag fraction from the Monte Carlo will be used to evaluate the systematic uncertainty on physical results. However, cross check of the tagging power will also be done on real data by tagging flavour specific B decays. On these decay a fit of both the oscillation frequency and amplitude allows the extraction of the wrong-tag.

### 4.3 Limiting factors

The tagging efficiency is limited by the branching fraction of b hadron decaying into a lepton or kaon combined with the production fraction of each species of b hadron, see Table 4.1 and 4.2.

The branching ratio of b hadron to leptons was directly measured to be  $10.59 \pm 0.22\%$ . Similarly, the kaon tag is limited to an efficiency of  $74 \pm 6\%$ .

The wrong-tag fraction is also enhanced by the oscillation of the neutral B mesons. Ref. [5] gives an average mixing parameter of  $\bar{\chi} = 11.84 \pm 0.45\%$ . In

b hadron	Fraction in %	Channel	BR in %
$B^-$	$38.8 \pm 1.3$	$B^+ \rightarrow \ell^+ \nu X$	$10.2 \pm 0.9$
$\bar{B}^0$	$38.8 \pm 1.3$	$B^0 \rightarrow \ell^+ \nu X$	$10.5 \pm 0.8$
$\bar{B}_s^0$	$10.6 \pm 1.3$	$B^{0/+} \rightarrow K^+ X$ (inclusive)	$78.9 \pm 2.5$
b baryon	$11.8 \pm 2.0$	$B_s^0 \rightarrow D_s^- X$	$94 \pm 30$
		$B_s^0 \rightarrow D_s^- \ell^+ \nu X$	$7.9 \pm 2.4$
		$\Lambda_b \rightarrow \Lambda_c \ell^- \bar{\nu} X$	$7.7 \pm 1.8$

Table 4.1: *Fractions of weakly decaying b hadron species in  $Z \rightarrow b \bar{b}$  decay and in  $p\bar{p}$  collisions at  $\sqrt{s} = 1.8$  TeV. Table from [5].*

Table 4.2: *Branching ratio for the dominant decay channels of the main b hadrons. Data from [5].*

addition to this irreducible source of wrong tag, leptons from the charm decays of the b hadron decays as well as kaons from the direct decay of the  $B_s^0$  will also degrade  $w$ .

The detector acceptance, the trigger, the tracking efficiency and the particle identification will also limit the probability to find a tagger. However a more subtle effect is also induced by the tracking. Combining the hits from the two ends of the detector could be tricky and in some cases *clones* can be produced. Clones are track duplicates. While the tracking tries to avoid clones as much as possible by killing a track which shares too many hits with another one, a clone rate of 1%-2% is still left. If a muon, electron or kaon from a signal B is cloned it has unfortunately a good chance to be selected as a tagger. We will see that this effect is observable in the dilepton channels and will need to be handled specifically in the future.

Finally, the bremsstrahlung of the electron is also an annoying effect which limits the tagging efficiency.

	$\mu$	e	K
Branching Ratios	10.6%	10.6%	74%
Oscillation, Acceptance and Trigger	8.7%	6.3%	33%
Track Reconstruction (as "long")	8.1%	5.2%	21%
Correct Particle Identification	7.5%	4.0%	15%
Tagging cuts	5.7%	2.8%	11%

Table 4.3: *Tagging efficiency for opposite-side muon, electron and kaon tags after various steps of the simulation for  $B_{(s)}^0 \rightarrow h^+ h^-$  events.*

Table 4.3 shows how the probability to find the right tagging lepton evolves through the different steps of the analysis.

## 4.4 Tagger selection criteria

For the opposite-side tagging one would ideally reconstruct the companion  $b$  hadron completely. However this approach is too difficult because  $b$  hadrons have so many ways to decay with most of them having a high track multiplicity such that the chance to reconstruct all the decay products of the hadron is very small. Just for the  $B^+/B^-$  meson the PDG indicate more than 150 decay channels, not counting the many different decays of the charmed hadron which is produced in many of them. Implementing the code to reconstruct such a large amount of channels is by itself unproductive if not impossible.

In the case of the same-side tagging the situation is different as only one particle is related to the signal  $B$  flavour. However, the relation is hidden inside the hadronisation process and thus no explicit way to find it exists.

To handle the presence of multiple interactions, tracks coming from these auxiliary interactions are removed prior to tagging. This will help by reducing the chance to select a track from these interactions. For this purpose, the reconstructed primary vertex toward which the  $B$  meson is pointing is selected and all the tracks with an impact parameter significance against any remaining vertex less 3.7 are removed.

The chosen solution is to select the *opposite-side* tagger based on the fact that the  $b$  hadron masses are large ( $> 5$  GeV) and thus the lepton or kaon tagger have a harder momentum spectrum. Also the  $B$  decay products are distributed in an isotropic way in the rest frame of the  $B$  and thus have a larger transverse momentum making this variable very useful.

The fact that the  $b$  hadron decays through a weak interaction implies a rather long life-time and thus a displaced vertex. The point of production of the possible tagger being distinct from the primary vertex, the impact parameter significance of the tagger can also be used as an input parameter of the algorithm.

As charged  $b$  hadrons cannot oscillate they clearly indicate the flavour of the signal  $B$ . Finding the charge of the companion  $b$  hadron means reconstructing its decay which is not practical. The solution is to sum the charge of the tracks which are compatible with a displaced vertex compatible with the hypothesis of being the other  $b$  hadron. If this hadron was indeed a charged one, the sum of the charge of the reconstructed tracks will be biased toward the hadron charge.

For the *same-side* tagger the strategy relies on the topological proximity of the tagger and the  $B$  meson.

The following subsections discuss the tuning of the particle identification and then the selection of the various tags. Ideally the optimisation of the cuts would be done by a multi-dimensional analysis of the effective tagging efficiency as a function of the relevant parameters. However, this approach needs so much computing time

that an iterative process is used instead. For each tag an initial set of cuts is selected from the distribution of the parameters. Then one parameter is changed with all the others fixed to get a distribution of the effective tagging efficiency  $\epsilon_{\text{eff}}$ . From this distribution a new cut value is obtained and used for the same procedure applied to the next parameter. In general this technique converges quickly. In the following subsections we will show the distribution of  $\epsilon_{\text{eff}}$  for each parameter when the others are fixed to the final value.

#### 4.4.1 Particle identification

Particle identification is crucial for the flavour tagging. Of course, a perfect particle identification is impossible to achieve. LHCb's software offers several identification algorithm and leaves the final decision to the user. While a default set of parameters exists, every one is free to use his/her own. Any analysis is free to choose between best purity and best efficiency for instance.

The information from the different sub-detectors are combined under the form of a series of likelihood values for the five hypotheses available to charged tracks, that is: muon, electron, kaon, pion and proton. One can construct a combined likelihood and take a decision by imposing a threshold [40, 41].

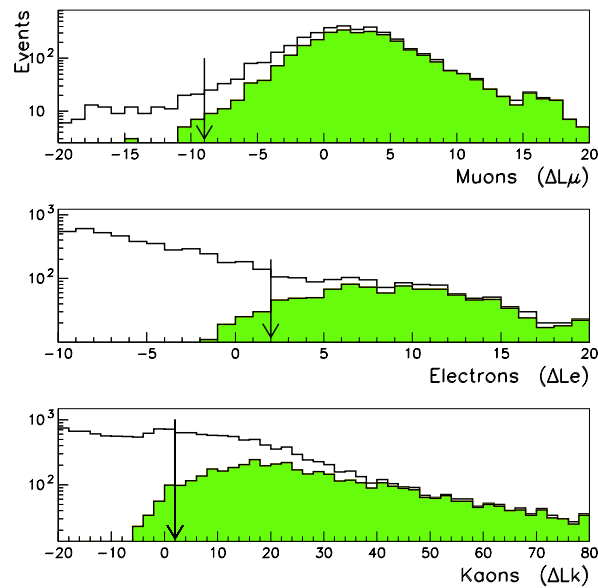


Figure 4.3: *Distributions of the difference in log-likelihood for the tagging candidates (muons, electron and kaons, from top to bottom) hypothesis and the default pion hypothesis in reconstructed  $B_s^0 \rightarrow D_s^\mp K^\pm$  events. Shaded histograms are for true muons, electrons or kaons.*

For the flavour tagging, specific values have been chosen. Figure 4.3 shows the log-likelihood distributions for the tagging candidates (muons, electron and kaons) in  $B_s^0 \rightarrow D_s^\mp K^\pm$  events where all the decay products are reconstructed. The arrow indicate the chosen cut for the difference in log-likelihood between the muon/electron/kaon hypothesis and the default pion hypothesis. For the muon the cut is placed at  $-9$  and the presence of information from the muon subsystem is required. Similarly, for the electron the information from the calorimeters is required to be present and the cut is set to 2. Finally the cut for the kaon is placed at 2 and information from the RICH must be present. A second cut in the difference in log-likelihood between the kaon and proton hypotheses is also used and set to 3.

#### 4.4.2 Opposite-side muon tagger

Because of the large mass of b hadrons, the selection of the muon tagger relies on the momentum and transverse momentum being harder than usual. The use of both allows for a better separation of the muon from the charm decay than just the use of the momentum.

Figure 4.4 shows that, at the generator level, the muons with a momentum larger than  $\sim 5$  GeV are more likely to come from the decay of a b quark than from other sources. However, the momentum does not allow one to distinguish the muon of the direct decay of the b from the muon produced by the decay of the charm. The transverse momentum distribution shown in Figure 4.5 indicates that muons produced by the decay of the charm can be rejected with a cut around 1.2 GeV. The distribution of the impact parameter significance of the reconstructed<sup>1</sup> muons presented in Figure 4.6 shows that even for small impact parameter the fraction of muons from a b is still important (but it is difficult to estimate as the first bins are depleted because of the momentum threshold inherent to the particle identification). For this reason no cut is applied on this parameter.

Figures 4.8 to 4.10 show how the effective tagging efficiency evolves when one cut is changed and the others are fixed at the retained value for  $B_s^0 \rightarrow K^+ K^-$  events. We can see that except in the case of the transverse momentum the dependance is quite weak. Figure 4.7, which shows the momentum versus transverse momentum distribution of the muon from  $b \rightarrow \mu$  and  $b \rightarrow c \rightarrow \mu$ , indicates that along the segment covered by Figure 4.8 we should not expect any change in the fraction of wrong muon coming from the charm, but along the path covered by Figure 4.9 an improvement can be expected up to 1.4 GeV and then a degradation due to the decreasing efficiency.

When more than one muon is selected, the one with the highest transverse momentum is kept.

---

<sup>1</sup>The error on the impact parameter is only available for reconstructed data.

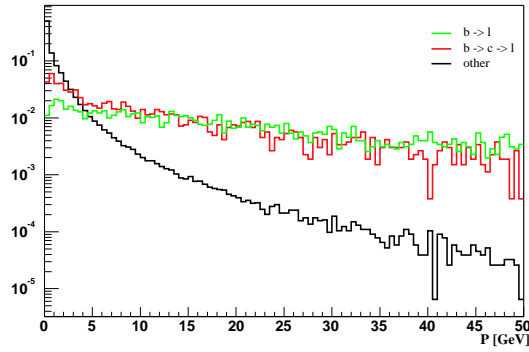


Figure 4.4: *Momentum distribution of the true muons in  $B_s^0 \rightarrow K^+ K^-$  events from different sources (normalised areas).*

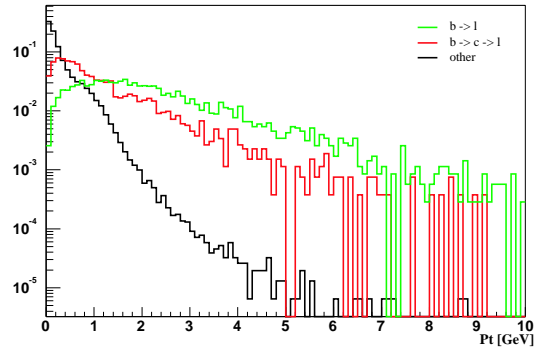


Figure 4.5: *Transverse momentum distribution of the true muons in  $B_s^0 \rightarrow K^+ K^-$  events from different sources (normalised areas).*

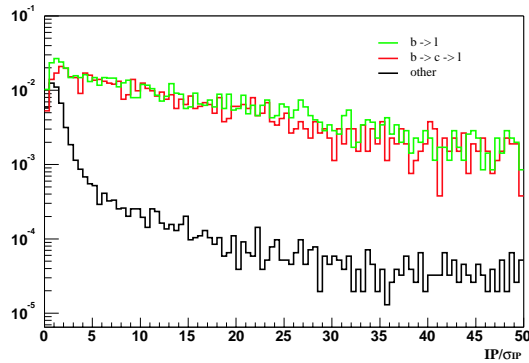


Figure 4.6:  *$IP/\sigma_{IP}$  distribution of the reconstructed muons in  $B_s^0 \rightarrow K^+ K^-$  events from different sources (normalised to the number of generated muons).*

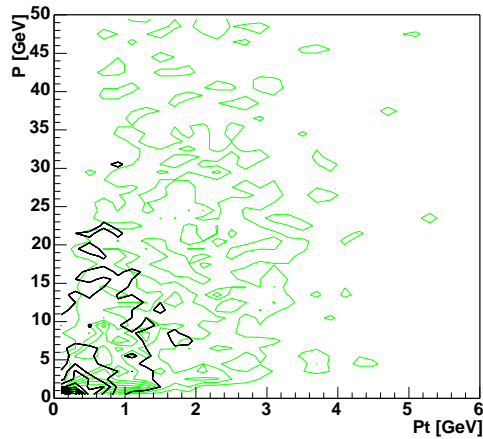


Figure 4.7: *Momentum vs transverse momentum distribution of the true muons in  $B_s^0 \rightarrow K^+ K^-$  events (light:  $b \rightarrow \mu$ ; dark:  $b \rightarrow c \rightarrow \mu$ ).*

The retained values for the cuts are thus:

$$p > 5 \text{ GeV}/c$$

$$p_t > 1.2 \text{ GeV}/c$$

No IP cut

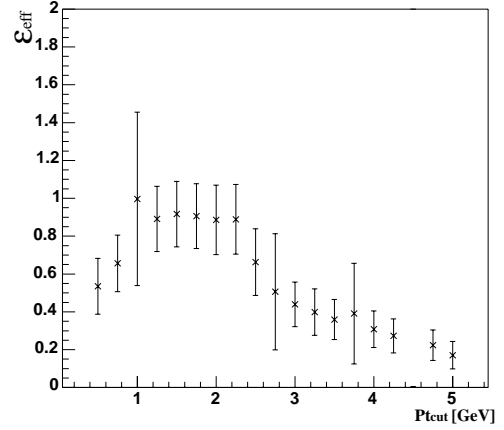
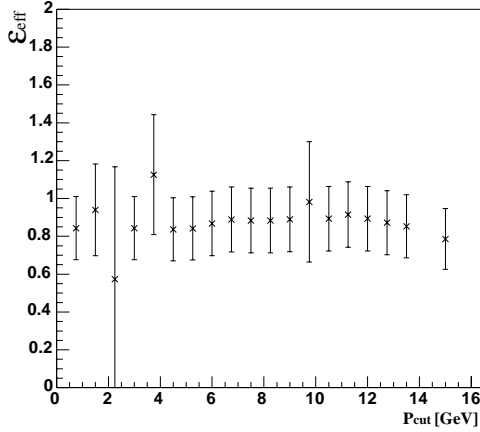


Figure 4.8:  $\epsilon_{\text{eff}}$  for muon tagger as a function of the momentum cut for reconstructed and triggered  $B_s^0 \rightarrow K^+ K^-$ .

Figure 4.9:  $\epsilon_{\text{eff}}$  for muon tagger as a function of the transverse momentum cut for reconstructed and triggered  $B_s^0 \rightarrow K^+ K^-$ .

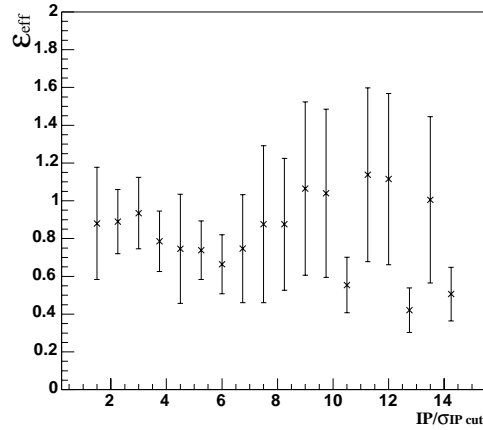


Figure 4.10:  $\epsilon_{\text{eff}}$  for muon tagger as a function of the  $IP/\sigma_{IP}$  cut for reconstructed and triggered  $B_s^0 \rightarrow K^+ K^-$ .

### 4.4.3 Opposite-side electron tagger

As the production mechanism of the electron tagger is identical to the muon one, the same criteria are used.

The distributions relative to the electrons shown in Figures 4.11 to 4.17 are similar to the one available for the muons. They have been produced in the same way and the same remarks as in the previous sub-section apply.



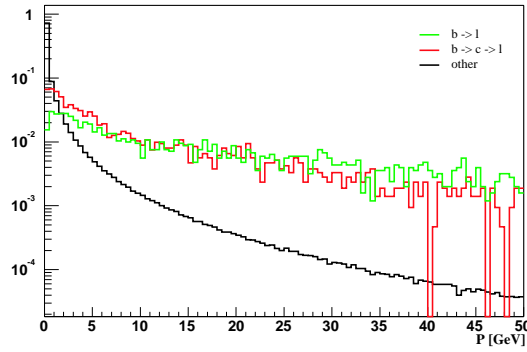


Figure 4.11: *Momentum distribution of the true electrons in  $B_s^0 \rightarrow K^+ K^-$  events from different sources (normalised areas).*

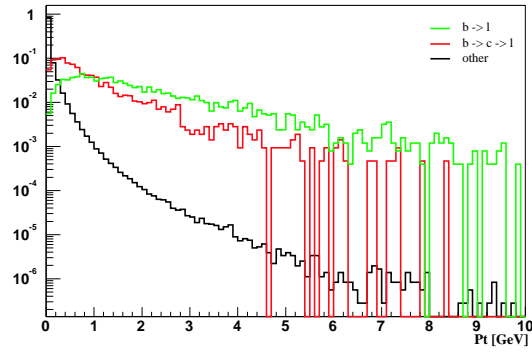


Figure 4.12: *Transverse momentum distribution of the true electrons in  $B_s^0 \rightarrow K^+ K^-$  events from different sources (normalised areas).*

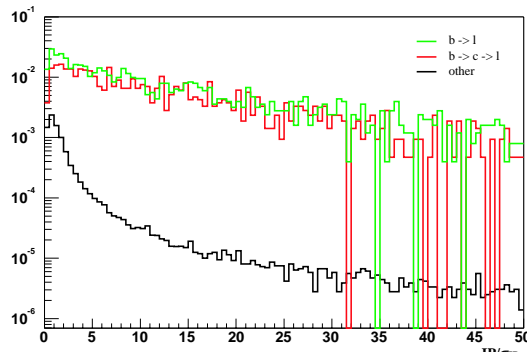


Figure 4.13:  *$IP/\sigma_{IP}$  distribution of the reconstructed electrons in  $B_s^0 \rightarrow K^+ K^-$  events from different sources (normalised to the number of generated electrons).*

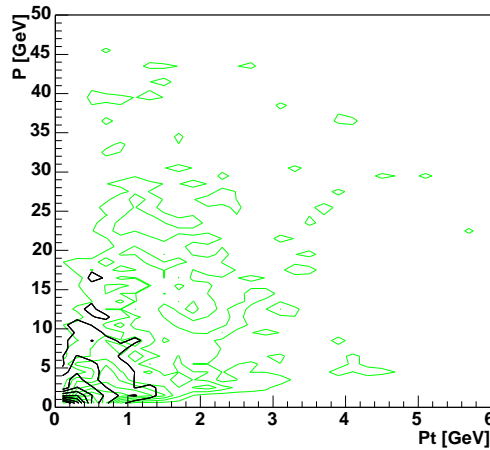


Figure 4.14: *Momentum vs transverse momentum distribution of the true electrons in  $B_s^0 \rightarrow K^+ K^-$  events (light:  $b \rightarrow e$ ; dark:  $b \rightarrow c \rightarrow e$ ).*

The retained values for the cuts are:

$$p > 5 \text{ GeV}/c$$

$$p_t > 1.2 \text{ GeV}/c$$

No IP cut

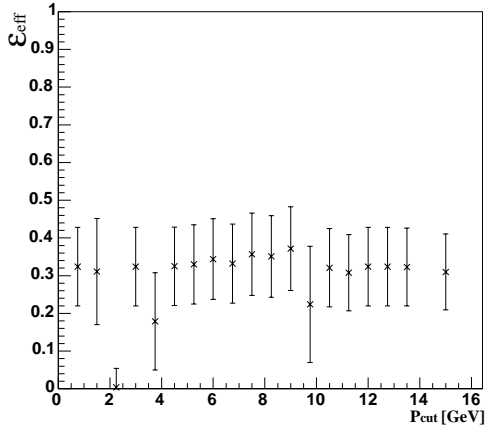


Figure 4.15:  $\epsilon_{eff}$  for electron tagger as a function of the momentum cut for reconstructed and triggered  $B_s^0 \rightarrow K^+ K^-$ .

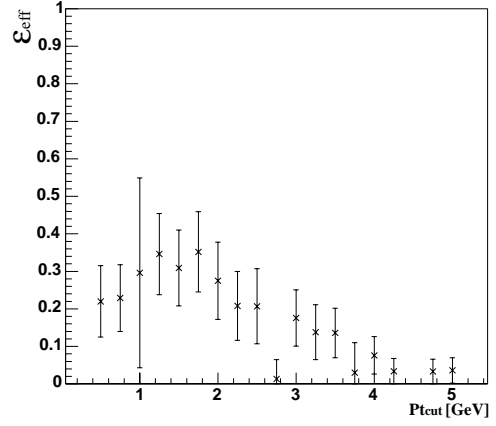


Figure 4.16:  $\epsilon_{eff}$  for electron tagger as a function of the transverse momentum cut for reconstructed and triggered  $B_s^0 \rightarrow K^+ K^-$ .

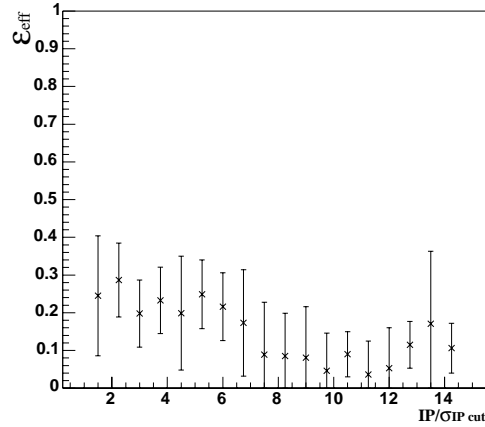


Figure 4.17:  $\epsilon_{eff}$  for electron tagger as a function of the  $IP/\sigma_{IP}$  cut for reconstructed and triggered  $B_s^0 \rightarrow K^+ K^-$ .

#### 4.4.4 Opposite-side kaon tagger

The selection of the kaon makes use of the impact parameter significance relative to the primary vertex the signal B points to. The kinematic cuts are also less effective for the kaon due to its larger mass and the fact that it is produced by the decay of the charm quark after the  $b \rightarrow c$  decay.

Unlike the case of the leptons, the selection of more than one kaon will lead to

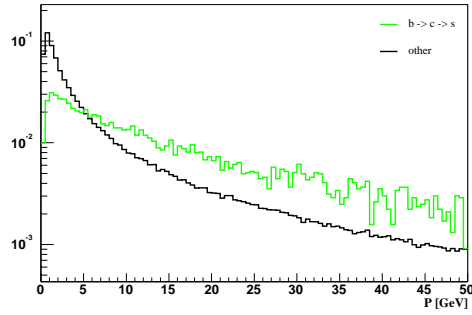


Figure 4.18: Momentum distribution of the true kaons in  $B_s^0 \rightarrow K^+ K^-$  events from different sources (normalised areas).

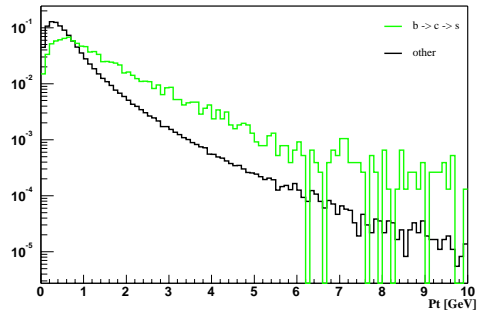


Figure 4.19: Transverse momentum distribution of the true kaons in  $B_s^0 \rightarrow K^+ K^-$  events from different sources (normalised areas).

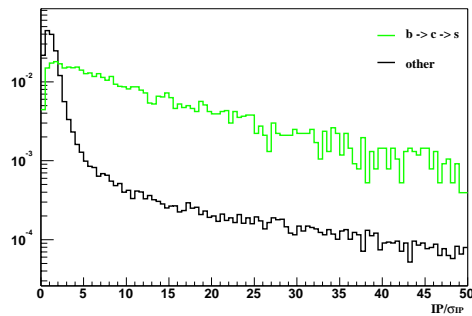


Figure 4.20:  $IP/\sigma_{IP}$  distribution of the reconstructed kaons in  $B_s^0 \rightarrow K^+ K^-$  events from different sources (normalised to the number of generated kaons).

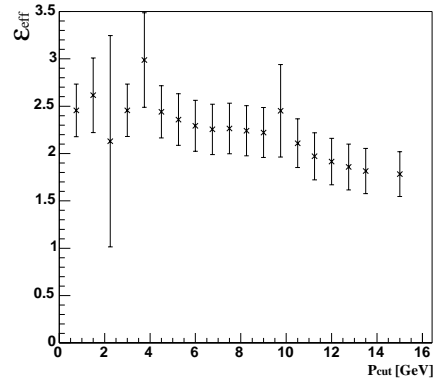


Figure 4.21:  $\epsilon_{eff}$  for opposite-side kaon tagger as a function of the momentum cut for reconstructed and triggered  $B_s^0 \rightarrow K^+ K^-$ .

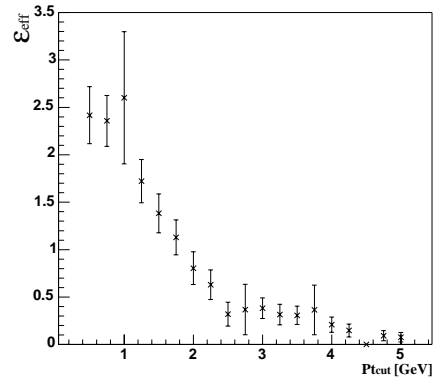


Figure 4.22:  $\epsilon_{eff}$  for opposite-side kaon tagger as a function of the transverse momentum cut for reconstructed and triggered  $B_s^0 \rightarrow K^+ K^-$ .

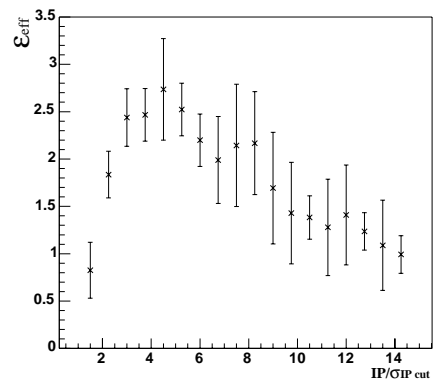


Figure 4.23:  $\epsilon_{eff}$  for opposite-side kaon tagger as a function of the  $IP/\sigma_{IP}$  cut for reconstructed and triggered  $B_s^0 \rightarrow K^+ K^-$ .

a vote. This tends to compensate slightly for the selection of kaons from a neutral resonance like a  $\phi(1020)$ .

The plots in Figure 4.22 show clearly that the transverse momentum cut must be set to a rather low value while Figure 4.23 shows that the impact parameter significance cut has the dominant effect.

The retained values for the cuts are:

$$p > 3 \text{ GeV}/c \qquad p_t > 0.4 \text{ GeV}/c \qquad \text{IP}/\sigma_{\text{IP}} > 3.7$$

#### 4.4.5 Opposite-side vertex charge

The inclusive reconstruction of the companion b-hadron vertex is done through the following steps:

1. Pre-selection of the tracks by removing tracks
  - which are identified as muons,
  - which are compatible with being the products of a  $K_S^0$  decay,
  - with  $p < 2 \text{ GeV}$ ,
  - with  $\text{IP}/\sigma_{\text{IP}} < 3$ .
2. Selection of two tracks as a seeding vertex based on
  - low error on the impact parameter ( $< 1\text{mm}$ ),
  - reasonably large  $\text{IP}/\sigma_{\text{IP}}$  ( $2 < \text{IP}/\sigma_{\text{IP}} < 100$ ) with respect to the primary vertex of the signal B,
  - good vertex quality ( $\chi^2/(\text{Number of degree of freedom}) < 10$ ),
  - not too close to the primary vertex ( $\Delta z > 1 \text{ mm}$ ),
  - good enough likelihood that the seed comes from the decay of a b hadron ( $L > 0.32$ ). This likelihood is based on the impact parameter significances and the transverse momenta of the two tracks, and the angle between them.

The seed with the best likelihood is retained.
3. Growing of the seeding vertex is done by iteratively adding a  $K^\pm$ ,  $\pi^\pm$  or  $e^\pm$  if these criteria are fulfilled:
  - $\sigma_{\text{IP}} < 1.5 \text{ mm}$  and  $1.8 < \text{IP}/\sigma_{\text{IP}} < 100$  relative to the primary vertex,
  - likelihood  $L > 0.2$ ,

- newly formed vertex has  $\chi^2/(\text{Number of degree of freedom}) < 5$  and  $\Delta_z > 1$  mm,

and removing the track which has the largest impact parameter significance relative to this vertex if it's larger than 3 and we still have more than two tracks until all pre-selected particles have been processed.

This tagging strategy was developed and tuned by Marta CALVI and Marco MUSY from the Università degli Studi di Milano. Further details can be found in [42].

#### 4.4.6 Same-side kaon tagger

The selection of the possible kaon which incorporates the companion of the s quark of a  $B_s^0$  is done by looking for a kaon which satisfies the same particle identification criteria as the opposite-side kaon in addition to these cuts:

- $IP/\sigma_{IP}$  relative to the primary vertex is less than 2.5,
- the difference in azimuthal direction between the kaon candidate and the signal B is less than 1.1,
- the difference in pseudo-rapidity between the kaon candidate and the signal B is less than 1,
- the mass of the B-K system is less than  $6.8 \text{ GeV}/c^2$  (the B mass plus  $1.5 \text{ GeV}/c^2$ ),
- the momentum is larger than  $4 \text{ GeV}/c$  and
- the transverse momentum is bigger than  $400 \text{ MeV}/c$ .

Like the vertex charge tagging, the same-side kaon tagging was provided by Marta CALVI and Marco MUSY from the Università degli Studi di Milano.

#### 4.4.7 Multiple tags selection

The search for a tag is done independently for each of the above strategies. So in some cases, more than one tag can be found.

The vertex charge tag is only used as a last resort tag when all the other answered **none**.

When two lepton tags are found we need to chose one because only one can come from the real decay of the b quark. In that case, the one with the highest momentum is retained as the b-hadron is most probably heavier.

At this point any combination of the lepton tag, opposite-side kaon tag and same-side kaon tag can occur. If we are trying to tag a  $B^0$  and not a  $B_s^0$ , the same-side kaon tag is ignored. Similarly, when a same-side pion tag will be present, it will be ignored when tagging a  $B_s^0$ . Then a simple vote to the majority is done leading to a combined decision.

The possibility to use a less naive approach, for instance with a neural-net, is under investigation by Marco MUSY from the Università degli Studi di Milano.

Category	$\epsilon$ [%]	$w$ [%]	$\epsilon_{\text{eff}}$ [%]
$\mu$ only	$8.8 \pm 0.3$	$35.6 \pm 1.8$	$0.73 \pm 0.18$
e only	$3.5 \pm 0.2$	$37.3 \pm 2.9$	$0.23 \pm 0.10$
$K_{OS}$ only	$10.4 \pm 0.3$	$36.7 \pm 1.7$	$0.74 \pm 0.19$
$K_{SS}$ only	$13.8 \pm 0.4$	$30.5 \pm 1.4$	$2.1 \pm 0.30$
vtx Q only	$11.7 \pm 0.4$	$43.3 \pm 1.6$	$0.21 \pm 0.10$
$\mu + K_{OS}$	$1.2 \pm 0.1$	$18.2 \pm 3.9$	$0.49 \pm 0.13$
$\mu + K_{SS}$	$1.2 \pm 0.1$	$19.4 \pm 4.0$	$0.45 \pm 0.13$
e + $K_{OS}$	$0.66 \pm 0.09$	$24.1 \pm 5.8$	$0.18 \pm 0.08$
e + $K_{SS}$	$0.52 \pm 0.08$	$20.9 \pm 6.2$	$0.18 \pm 0.08$
$K_{OS} + K_{SS}$	$1.7 \pm 0.1$	$20.4 \pm 3.4$	$0.58 \pm 0.15$
$\mu + K_{OS} + K_{SS}$	$0.52 \pm 0.08$	$27.9 \pm 6.8$	$0.10 \pm 0.07$
e + $K_{OS} + K_{SS}$	$0.26 \pm 0.06$	$42.9 \pm 10.8$	$0.01 \pm 0.02$
Total	$54.2 \pm 0.7$	$33.4 \pm 0.8$	$5.98 \pm 0.50$

Table 4.4: The list of the categories used when combining tags and their corresponding tagging efficiency for  $L0 \& L1$  triggered and selected  $B_s^0 \rightarrow D_s^\mp K^\pm$ .

Each of the possible tag combinations defines what is called a *category*. As all these categories are orthogonal, the evaluation of the tagging power is done per category. Finally the global tagging power is done by summing the effective tagging efficiency of all the categories because they are independent and mutually exclusive. The tagging efficiency is also summed and the wrong-tag fraction is computed with  $w = \frac{1}{2}(1 - \sqrt{\epsilon_{\text{eff}}/\epsilon})$ .

## 4.5 Triggers effects

The trigger and the tagging work in a similar way. They both look for high transverse momentum tracks and high impact parameter tracks. While the tagging explicitly removes the tracks from the signal B, the trigger does not have so much information and will thus fire on particle from either side. Firing on the signal

side is the expected behaviour. Triggering on the other side will affect the tagging performance and must be studied in detail.

Both the Level-0 with its high  $p_t$  lepton and hadron triggers and the Level-1 with its topological trigger will affect the tagging by enriching the sample of events with more easily taggable events. This effect is shown below for each tag by comparing a set of channels which can and cannot trigger.

### 4.5.1 Effects of the triggers on the muon tagging

Trigger	$\epsilon$	$w$	$\epsilon_{\text{eff}}$
none	$6.3 \pm 0.1$	$36.2 \pm 0.9$	$0.48 \pm 0.06$
L0	$9.6 \pm 0.2$	$34.9 \pm 1.0$	$0.87 \pm 0.11$
L0&L1	$11.1 \pm 0.3$	$35.3 \pm 1.1$	$0.96 \pm 0.15$

Table 4.5: *Evolution of the muon tagging power over trigger levels for reconstructed  $B_{(s)}^0 \rightarrow hh$  before selection.*

Trigger	$\epsilon$	$w$	$\epsilon_{\text{eff}}$
none	$9.0 \pm 0.1$	$40.5 \pm 0.7$	$0.32 \pm 0.05$
L0	$9.5 \pm 0.1$	$40.3 \pm 0.8$	$0.36 \pm 0.06$
L0&L1	$10.8 \pm 0.2$	$39.8 \pm 0.9$	$0.44 \pm 0.07$

Table 4.6: *Evolution of the muon tagging power over trigger levels for reconstructed  $B_s^0 \rightarrow (J/\psi(1S) \rightarrow \mu \mu)(\phi(1020) \rightarrow K^+ K^-)$  before selection.*

The effect of the muon trigger enriching the event sample is clearly demonstrated in Table 4.5 with a 50% increase in the tagging efficiency. Also the wrong-tag fractions at each trigger level are compatible.

Table 4.6 shows that much less improvement is obtained when the trigger has the ability to pickup a high  $p_t$  muon from the signal B. However, two things are important to notice:

1. the efficiency before trigger is already larger than in Table 4.5,
2. the wrong-tag fraction at any trigger level is worse than in the previously mentioned table.

These strange effects have the same origin. We observe that if we increase the fraction of events with a muon to move from the 6% of the  $B_{(s)}^0 \rightarrow hh$ <sup>2</sup> to 9%, adding only random muons ( $w = 0.5$ ), the wrong-tag of 36% will raise to  $\sim 41\%$ . This seems indeed to be the case; the origin of these muons is two-fold:

<sup>2</sup> $B_{(s)}^0 \rightarrow hh$  stands for  $B_d^0 \rightarrow \pi^+ \pi^-$ ,  $B_d^0 \rightarrow K^+ \pi^-$ ,  $B_s^0 \rightarrow \pi^+ K^-$  and  $B_s^0 \rightarrow K^+ K^-$ .

1. Clones from the signal muon. With a clone rate of only 1%, at most 2 of the 3 additional percents can be explained that way.
2. Decay in flight of the kaon produced by the  $\phi(1020)$ . Due to the rather soft momentum spectrum of the kaons  $\sim 16\%$  of them decay before the tracking chambers and 66.7% of them will produce a muon. So if the kink induced by the decay is small a few of them can be reconstructed as muons and bias the tagging.

### 4.5.2 Effects of the triggers on the electron tagging

Trigger	$\epsilon$	$w$	$\epsilon_{\text{eff}}$
none	$4.3 \pm 0.1$	$35.9 \pm 1.0$	$0.35 \pm 0.05$
L0	$4.6 \pm 0.1$	$36.9 \pm 1.4$	$0.32 \pm 0.07$
L0&L1	$5.2 \pm 0.2$	$35.6 \pm 1.7$	$0.43 \pm 0.10$

Table 4.7: *Evolution of the electron tagging power over trigger levels for reconstructed  $B_{(s)}^0 \rightarrow hh$ .*

Trigger	$\epsilon$	$w$	$\epsilon_{\text{eff}}$
none	$5.4 \pm 0.4$	$38.7 \pm 3.3$	$0.27 \pm 0.16$
L0	$6.0 \pm 0.5$	$39.3 \pm 4.4$	$0.27 \pm 0.23$
L0&L1	$6.8 \pm 0.7$	$43.8 \pm 5.5$	$0.11 \pm 0.19$

Table 4.8: *Evolution of the electron tagging power over trigger levels for reconstructed  $B_s^0 \rightarrow (J/\psi(1S) \rightarrow e e)(\phi(1020) \rightarrow K^+ K^-)$ .*

Table 4.7 shows that the electron trigger also improves the tagging efficiency. However the amplitude is lower.

Table 4.8 shows a similar behaviour to Table 4.6. The explanation is the same and the difference in amplitude is most probably caused by the lower branching fraction of kaon to electron, which is only 4.87%.

### 4.5.3 Effects of the triggers on the opposite-side kaon tagging

Table 4.9 shows that the Level-1 trigger helps the opposite-side kaon tagging. This reflects the fact that both the L1 and the opposite-side kaon tagging rely on tracks with high impact parameter.

Unlike the lepton tags, the kaon tag efficiency is not affected by the Level-0. This is not surprising for  $B_{(s)}^0 \rightarrow hh$  channels as the trigger can easily fire on the



Trigger	$\epsilon$	$w$	$\epsilon_{\text{eff}}$
none	$14.7 \pm 0.2$	$34.1 \pm 0.6$	$1.48 \pm 0.11$
L0	$14.6 \pm 0.2$	$31.8 \pm 0.8$	$1.93 \pm 0.16$
L0&L1	$16.6 \pm 0.3$	$31.2 \pm 0.9$	$2.35 \pm 0.23$

Table 4.9: *Evolution of the tagging power of the opposite-side kaon over trigger levels for reconstructed  $B_{(s)}^0 \rightarrow hh$ .*

signal hadron. Isolating an effect of the hadron trigger on the tagging is impossible as it would require a purely leptonic decay of the B meson. Such a decay has never been observed and is not implemented in our generator.

#### 4.5.4 Effects of the triggers on the vertex charge tagging

Trigger	$\epsilon$	$w$	$\epsilon_{\text{eff}}$
none	$21.3 \pm 0.2$	$42.0 \pm 0.5$	$0.54 \pm 0.07$
L0	$21.2 \pm 0.3$	$40.7 \pm 0.7$	$0.74 \pm 0.11$
L0&L1	$24.3 \pm 0.3$	$39.9 \pm 0.8$	$1.00 \pm 0.16$

Table 4.10: *Evolution of the vertex charge tagging power over trigger levels for reconstructed  $B_{(s)}^0 \rightarrow hh$ .*

The most sensitive tagging to the effect of the Level-1 topological trigger is the vertex charge tagging. Table 4.10 shows clearly that the L1 help select events with high impact parameter tracks and thus secondary vertices.

#### 4.5.5 Global effects of the triggers

$B_s^0 \rightarrow hh$						
Trigger	$\epsilon$	$w$	$\epsilon_{\text{eff}}$			
none	$43.9 \pm 0.3$	$34.4 \pm 0.5$	$4.3 \pm 0.2$			
L0	$46.1 \pm 0.4$	$32.7 \pm 0.6$	$5.5 \pm 0.4$			
L0&L1	$49.8 \pm 0.5$	$32.8 \pm 0.8$	$5.9 \pm 0.5$			
$B_s^0 \rightarrow J/\psi(\mu\mu)\phi(\text{KK})$			$B_s^0 \rightarrow J/\psi(\text{ee})\phi(\text{KK})$			
Trigger	$\epsilon$	$w$	$\epsilon_{\text{eff}}$	$\epsilon$	$w$	$\epsilon_{\text{eff}}$
none	$47.4 \pm 0.2$	$33.9 \pm 0.3$	$4.9 \pm 0.2$	$44.7 \pm 0.8$	$34.9 \pm 1.2$	$4.1 \pm 0.6$
L0	$48.1 \pm 0.2$	$33.8 \pm 0.4$	$5.0 \pm 0.2$	$48.3 \pm 1.1$	$32.4 \pm 1.7$	$6.0 \pm 1.0$
L0&L1	$50.4 \pm 0.3$	$33.4 \pm 0.4$	$5.5 \pm 0.3$	$53.6 \pm 1.5$	$32.2 \pm 2.1$	$6.8 \pm 1.4$

Table 4.11: *Sensitivity of the combined tagging to the different trigger levels.*

For completeness we give the combined tagging results in Table 4.11 for a few channels.

## 4.6 Multiple interactions

“Multiple interactions” means that more than one pair of protons collided during a given bunch crossing. But when studying the effect of these multiple interactions we are interested only in the events which give visible signals in the detector. As the LHCb experiment only covers the low angle region on one side of the interaction point, many multiple interactions do not give signals in the detector. For this reason this section only considers *visible interactions*. An interaction is visible if it gives birth to at least two tracks each having three VELO  $R$  hits and three VELO  $\phi$  hits and matched to a track segment in T1 to T3 (Table 4.12).

The number of reconstructed primary vertices, which should reflect the number of visible interactions, can also be used (Table 4.13). As the number of reconstructed primary vertices is lower in average than the number of interactions, we can extract some more information by comparing the tagging power for these two variables.

# of visible interaction	1	2	3+
Frequency in %	69.0±0.9	25.2±0.4	5.9±0.2

Table 4.12: *Frequency of multiple visible interactions.*

# of primary vertices	1	2	3+
Frequency in %	78.2±0.9	20.3±0.4	1.5±0.1

Table 4.13: *Frequency of reconstructed primary vertices.*

count	$\epsilon$	$w$	$\epsilon_{\text{eff}}$	count	$\epsilon$	$w$	$\epsilon_{\text{eff}}$
1	11.9±0.2	34.7±0.7	1.12±0.11	1	6.1±0.1	36.9±1.0	0.42±0.07
2+	18.2±0.4	35.2±1.1	1.60±0.23	2+	6.2±0.2	36.0±1.8	0.49±0.13
1+	13.3±0.2	34.8±0.6	1.23±0.10	1+	6.1±0.1	36.7±0.9	0.43±0.06

Table 4.14: *Tagging power of the muon as a function of the number of visible interactions (for reconstructed and triggered  $B \rightarrow hh$  events).*

Table 4.15: *Tagging power of the electron as a function of the number of visible interactions (for reconstructed and triggered  $B \rightarrow hh$  events).*

count	per visible interactions			per primary vertices		
	$\epsilon$	$w$	$\epsilon_{\text{eff}}$	$\epsilon$	$w$	$\epsilon_{\text{eff}}$
1	18.0±0.2	28.2±0.6	3.42±0.18	19.1±0.2	30.3±0.5	2.98±0.16
2+	22.5±0.4	38.1±1.0	1.29±0.21	18.3±0.5	34.6±1.3	1.74±0.30
1+	19.0±0.2	30.9±0.5	2.78±0.14	19.0±0.2	30.9±0.5	2.78±0.14

Table 4.16: *Tagging power of the opposite-side kaon, on the left per visible interactions, on the right per reconstructed primary vertices (for reconstructed and triggered  $B \rightarrow hh$  events).*

count	per visible interactions			per primary vertices		
	$\epsilon$	$w$	$\epsilon_{\text{eff}}$	$\epsilon$	$w$	$\epsilon_{\text{eff}}$
1	20.5±0.3	28.7±0.6	3.71±0.23	20.6±0.2	29.3±0.6	3.53±0.21
2+	17.9±0.4	29.3±1.3	3.08±0.38	15.7±0.5	25.3±1.6	3.83±0.52
1+	19.9±0.2	28.8±0.6	3.56±0.20	19.9±0.2	28.8±0.6	3.56±0.20

Table 4.17: *Tagging power of the same-side kaon, on the left per visible interactions, on the right per reconstructed primary vertices (for reconstructed and triggered  $B_s^0 \rightarrow D_s^\pm K^\pm$  events).*

count	per visible interactions			per primary vertices		
	$\epsilon$	$w$	$\epsilon_{\text{eff}}$	$\epsilon$	$w$	$\epsilon_{\text{eff}}$
1	26.1±0.2	39.2±0.5	1.22±0.11	28.0±0.2	40.0±0.5	1.12±0.10
2+	32.8±0.4	43.7±0.8	0.52±0.14	25.9±0.5	42.9±1.1	0.52±0.17
1+	27.7±0.2	40.4±0.4	1.02±0.09	27.7±0.2	40.4±0.4	1.02±0.09

Table 4.18: *Tagging power of the vertex charge, on the left per visible interactions, on the right per reconstructed primary vertices (for reconstructed and triggered  $B \rightarrow hh$  events).*

# vis. int.	$\epsilon$	$w$	$\epsilon_{\text{eff}}$
1	52.3±0.6	32.5±0.9	6.4±0.6
2+	62.4±1.2	35.5±1.6	5.2±1.0
1+	54.2±0.6	33.4±0.8	6.0±0.5

Table 4.19: *Variation of the combined tagging power for single and multiple visible interaction events (for reconstructed and triggered  $B_s^0 \rightarrow D_s^\pm K^\pm$  events).*

Globally, the higher the number of visible interactions, the larger the efficiency. As the number of visible interactions grows, the number of tracks in the event increases and the chance to find a tag is greater.

Of the various tags, the electron is the only one which is not much affected as hadronic collision produces to a large extend only hadrons (Table 4.15). The muon tagging power increase for multiple interaction due to an interplay between the muon trigger and the pile-up veto, the former having precedence; also some more kaons will decay into muons (Table 4.14).

The opposite-side kaon and the vertex charge show a noticeable degradation of the wrong-tag (Tables 4.16 and 4.18). As both use the impact-parameter as an important cut they tend to be disturbed by the new tracks, which usually have a large impact parameter against the primary vertex of the B.

Table 4.17 shows that the tagging efficiency for the same-side kaon tag decrease with the number of interaction. This reflects the fact that we select kaons coming

from the primary vertex of the signal B. When more than one primary vertex is reconstructed, the precision on the position of the primary vertex of the B is higher than when only one is reconstructed as there is more than one primary vertex in average. Consequently fewer kaons are accepted due to the impact parameter significance being higher.

Table 4.19 gives the combined tagging power for the single and multiple visible interactions.

Looking at what happens when the tagging power is computed per reconstructed primary vertices shows that the effect mostly comes from the fact that the mean number of reconstructed primary vertices is lower than the mean number of visible interactions. As the particles are filtered to remove the one that do not come from the primary vertex toward which the B is pointing, the results are better when the visible interactions are reconstructed as separate primary vertices. When multiple interactions are present and only one primary vertex is reconstructed, the resolution gets worse and the impact parameter significance is diminished. This allows more tracks to pass the cuts and thus increases the efficiency and the wrong-tag fraction at the same time.

## 4.7 Dependency on specific decay channels

Channel	$\epsilon$	$\omega$	$\epsilon(1 - 2\omega)^2$
$B^0 \rightarrow \pi\pi$	$41.8 \pm 0.7$	$34.9 \pm 1.1$	$3.8 \pm 0.5$
$B^0 \rightarrow K\pi$	$43.2 \pm 1.4$	$33.3 \pm 2.1$	$4.8 \pm 1.1$
<b><math>B^0 \rightarrow hh</math></b>	$42.1 \pm 0.6$	$34.7 \pm 1.0$	$4.0 \pm 0.5$
$B^0 \rightarrow J/\psi(ee)K_S^0$	$45.3 \pm 2.7$	$38.2 \pm 3.5$	$2.5 \pm 1.4$
$B^0 \rightarrow J/\psi(\mu\mu)K_S^0$	$45.1 \pm 1.3$	$36.7 \pm 1.9$	$3.2 \pm 0.8$
$B^0 \rightarrow J/\psi(\mu\mu)K^{*0}$	$41.2 \pm 0.6$	$34.8 \pm 1.1$	$3.8 \pm 0.5$
$\bar{B}^0 \rightarrow J/\psi(\mu\mu)K^{*0}$	$42.7 \pm 0.7$	$33.4 \pm 1.1$	$4.7 \pm 0.5$
<b><math>B^0/\bar{B}^0 \rightarrow J/\psi(\mu\mu)K^{*0}</math></b>	$41.9 \pm 0.5$	$34.3 \pm 0.8$	$4.2 \pm 0.4$
Channel	$\epsilon$	$\omega$	$\epsilon(1 - 2\omega)^2$
$B_s^0 \rightarrow D_s^\mp K^\pm$	$54.3 \pm 0.6$	$33.4 \pm 0.8$	$6.0 \pm 0.5$
$B_s^0 \rightarrow D_s^- \pi^+$	$54.7 \pm 1.2$	$30.0 \pm 1.6$	$8.7 \pm 1.2$
<b><math>B_s^0 \rightarrow D_s^\mp h^\pm</math></b>	$54.3 \pm 0.5$	$32.8 \pm 0.7$	$6.4 \pm 0.5$
$B_s^0 \rightarrow KK$	$49.8 \pm 0.5$	$33.0 \pm 0.8$	$5.8 \pm 0.5$
$B_s^0 \rightarrow \pi K$	$49.5 \pm 1.8$	$30.4 \pm 2.6$	$7.6 \pm 1.7$
<b><math>B_s^0 \rightarrow hh</math></b>	$49.8 \pm 0.5$	$32.8 \pm 0.8$	$5.9 \pm 0.5$
$B_s^0 \rightarrow J/\psi(ee)\phi(KK)$	$53.6 \pm 1.5$	$32.3 \pm 2.1$	$6.8 \pm 1.4$
$B_s^0 \rightarrow J/\psi(\mu\mu)\phi(KK)$	$50.4 \pm 0.3$	$33.4 \pm 0.4$	$5.5 \pm 0.3$

Table 4.20: Summary of the combined tagging power for different  $B_d$  channels (top) and  $B_s$  channels (bottom) after  $L0^{\&L}L1$  and selection. The entries in bold face are combined results of some of the preceding channels.

Table 4.20 gives a summary of the tagging power of the studied  $B_d$  and  $B_s$  channels for selected and triggered events. The results for  $B_d$  are lower than those  $B_s$  as the same-side kaon tag cannot be used. The differences between the channels are caused by acceptance and selection cuts of the signal  $B$ , which are correlated to the tagging  $b$ , as well as by the trigger as explained in the previous sections.

## 4.8 The flavour tagging software

The flavour tagging code used in LHCb was designed as an independent package for the Gaudi framework to be used with the LHCb analysis framework DaVinci. The use of modern software technologies like object oriented programming and dynamic code loading allows to split such a large project in smaller independent chunks.

While the design goal for the flavour tagging was to have a package which ignores the Monte Carlo truth and another one which does the monitoring with access to the truth, everything is still inside a single package called `FlavourTagging`. This package is just one of many other DaVinci packages.

When code can be dynamically loaded, a clear interface is a must to avoid specialised loading code which would kill the very first advantage of dynamic code loading. For this purpose the `FlavourTagging` provides an implementation of the generic `IAlgorithm` interface which defines the basic functions to hook up a new piece of reconstruction or analysis code. This is the access point through which DaVinci will ask the `FlavourTagging` to do its job.

Newcomers might find this programmatic approach rather off putting, but Gaudi hides all these details behind a *job option file* where a simple list of the names of different implementation of the `IAlgorithm` is required to have them automatically executed (specifying the dynamic module to load is also needed). Gaudi also provides a simplified way to configure any block of software through the job option file.

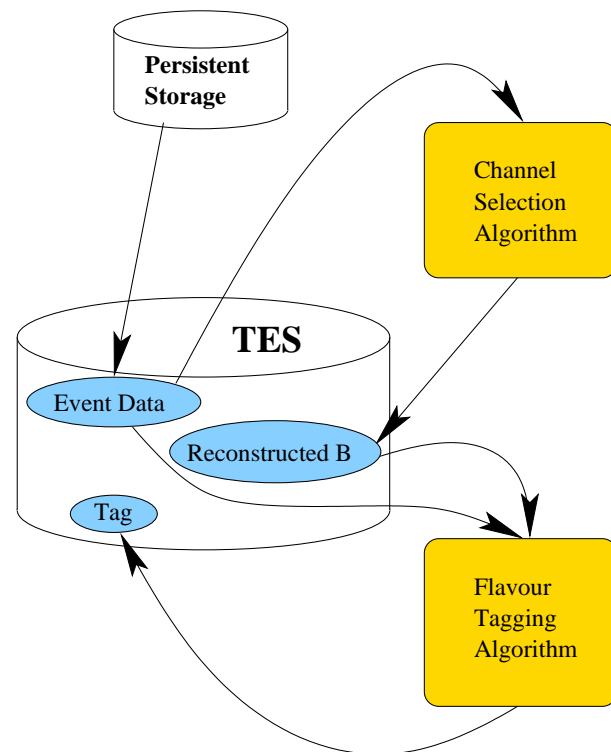


Figure 4.24: *Main data flow of a tagging job.*

The last fundamental thing to know about the Gaudi framework is how data are exchanged between the different blocks of code. In Gaudi any building block has access to a minimal number of *Services*. These services can be used to access other blocks of code (transparently loading them if needed). Or to retrieve and save data from/to different storage area. For the usual exchange of data the *Transient Event Store* (TES) is available. This approach avoids the need to care for file IO and allows to specify through the job option file where data should be read/written and under which format.

Figure 4.24 summarises how the different building blocks of a typical tagging job fit together and how the data are exchanged.

### 4.8.1 Inside look

The internal code of the flavour tagging uses the modular approach of the C++ and dynamic module loading to its full extent. The Gaudi framework provides special features for lightweight function centric tools, which can easily be replaced by any other implementation.

The flavour tagging software is build around the idea that any tagging strategies have the same thing to do and the same data requirements. So this has been abstracted in an interface, the `IFlavourTaggingTool`. This is a specialisation of Gaudi's `IAlgTool` interface. That way the implementation of this interface can easily be accessed from the Tool Service.

The `IFlavourTaggingTool` provides a set of call signatures to accommodate the various data type used in DaVinci. The main entry point of the tool is the `tagThisB` method which returns a `FlavourTag` object containing the tagging decision based on these three inputs:

- The reconstructed B to tag.
- The set of particles that makes this event.
- The reconstructed primary vertex of the B.

All the other methods present in the `IFlavourTaggingTool` are lower level ones, which take different set a particles as input. They simply reflect the inner work, which is to find all the decay products of the B to tag and then remove them from the list of particles to consider for the tagging.

At the time being, four implementations of the `IFlavourTaggingTool` interface exist in the flavour tagging package. They are:

1. `SingleParticleTaggingTool`: This implementation uses kinematic cuts as well as the  $IP/\sigma_{IP}$  cut and particle ID to find a tag. It's used, with appropriate settings, to produce both lepton tags and the opposite-side kaon tag.

2. `KaonSameSideTaggingTool` The same-side kaon tag strategy.
3. `VertexChargeTaggingTool` The implementation of the vertex charge tagging.
4. `CategoryTaggingTool` This tool is a dedicated tag combiner, which uses the preceding tools and then combines their answers.

The feeding of the main tagging tool (the `CategoryTaggingTool`) is done with the implementation of the `IAlgorithm` which is named `FlavourTaggingAlgorithm`. This algorithm takes three main parameters:

1. the location of the reconstructed B in the TES,
2. the tagging tool to use, which defaults to the `CategoryTaggingTool` and
3. the minimum impact parameter significance with respect to the pile-up vertices (default is 3.7).

The `FlavourTaggingAlgorithm` will get the list of particles in this event and for each B hypothesis, it will:

- Find the primary vertex the B is pointing to.
- Build the list of pile-up vertices, that is any other primary vertex.
- Pick-up all the particle in the event which have an  $IP/\sigma_{IP}$  larger than the third parameter above against all the pile-up vertices.
- Call the specified tagging tool.
- Save the resulting `FlavourTag` in the TES.

### 4.8.2 Flavour tags

The tags saved in the TES contain some more information in addition to the simple decision whether the B contained a b or  $\bar{b}$  quark (or if it was not taggable). Obviously we want to now for which B this information is meaningful. For this purpose a pointer to the B which was tagged is saved in the `FlavourTag` object. The kind of tag (particle tagger or vertex charge) is also saved and if relevant, the selected tagger is saved too.

So once the tags have been produced, the physics analysis can simply loop over them. From there it can find the B and its flavour. The rest is analysis specific.

## 4.9 Future

The following step in the study of LHCb's flavour tagging would be to test different ways to combine the various tags. In particular, an even number of tags often leads to a **none** tag. Hopefully, one could combine the tags with a weighted sum to try to recover as much events as possible. More generally a neural network could be used for this purpose.

Another thing to watch is the evolution of the quality of the electron reconstruction and identification as this can bring improvements to the electron tag.

Also efforts on the tracking could improve the tagging. For instance the inclusion of upstreams tracks or a better clone killing.

Finally, new tagging strategies can be added to the software which was designed with this ability in mind. These additional strategies include the same-side pion tag and the jet-charge tag.



# Chapter 5

## Contribution to the development of LHCb's Vertex Locator

---

The development of LHCb's vertex locator required several realistic tests of the possible alternatives. In this chapter the reader will find some insight to some of these tests as well as the major results obtained.

---

Almost any new experiment pushes the technological limits a bit further. This implies that any new technology must be tested and characterised. The development of a large experiment like LHCb is not done entirely by simulations. The parameters used in the simulation must reflect the reality and they can only be obtained by small experiments taking place in conditions which are as closed as possible to the final system.

These new technologies are used to solve specific problems. In the case of the VELO detector, some major technological issues are:

**The high radiation environment.** The inner part of the silicon sensors will be exposed to a radiation level of up to  $1.3 \cdot 10^{14} n_{\text{eq}}/\text{cm}^2$  per year while the outer region will only have to resist to a dose of  $5 \cdot 10^{12} n_{\text{eq}}/\text{cm}^2$  per year.

**The high data-taking rate and event size.** The bunch crossing rate of the LHC of 40 MHz as well as the number of channels of the order of 200'000 makes it hard to read-out the whole detector every time.

**The cost constraint.**

In order to make the right design decision, different kinds of silicon sensors, different strip pitches, read-out electronics and so on were tested. The tests are usually of two kinds. Laboratory tests are done providing detailed control and

characterisation. They also give the background required before the second kind of test — the testbeams. Testbeams reproduce as much as possible the real condition. They are done on some of the CERN PS or SPS beams. Due to the limited number of beams and the large number of groups from all of the LHC experiments which need access to the beams the time available for a testbeam is rather limited and must be used as efficiently as possible.

The following section presents the characterisation of the “telescope” used in the subsequent tests. The remaining sections present the infrastructure and issues encountered during the testing of one of the possible read-out chips as well as some sensor technologies. The kinds of sensors tested and their behaviour after irradiation will be presented in Section 5.4.

## 5.1 VELO telescope characterisation

A “telescope” is a tool which allows the determination of the flight direction of a particle. Such a tool will be used to measure the efficiency and resolution of sample detectors. In 1998 a “solid state telescope” was built for testing LHCb VELO silicon sensor prototypes. Preliminary prototypes of the LHCb sensors were used in this telescope. Several beam tests were performed to fully characterise them. The efficiency as a function of the bias voltage, the resolution as a function of the angle of the tracks, and the capacitive charge sharing between adjacent strips were measured. The results were compared with a Monte Carlo simulation of the silicon and LHCb’s simulation software was updated with this improved knowledge.

### 5.1.1 The VELO telescope

The telescope is made of three stations each consisting of one  $R$ - and one  $\phi$ -measuring sensor made from 300  $\mu\text{m}$  thick  $n$ -on- $n$  wafers covering  $72^\circ$ . The  $R$  type detectors have circular strips with pitches of 40  $\mu\text{m}$  and 60  $\mu\text{m}$ . The  $\phi$  type sensors have strips arranged radially, with pitches varying between 46  $\mu\text{m}$  and 126  $\mu\text{m}$ . Each strip in the  $\phi$  type detector is rotated by  $5^\circ$  about its centre to provide stereo information. The telescope detectors are equipped with slow VA2 read-out chips with an integration time of 1  $\mu\text{s}$ . Figure 5.1 shows the telescope with both halves equipped.

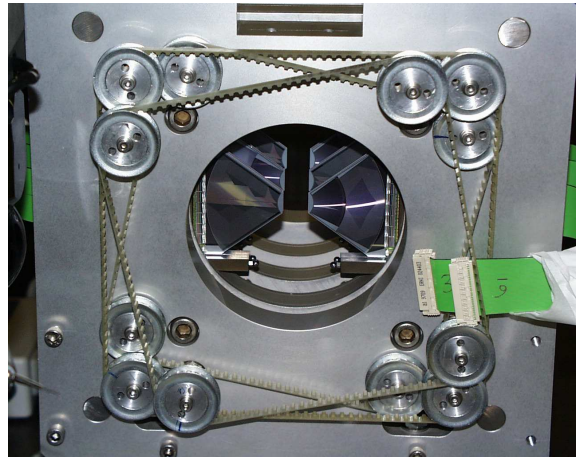


Figure 5.1: *The 1998 test beam telescope containing six symmetrically placed stations, each containing one  $R$ -measuring and one  $\phi$ -measuring sensor. (Only one half of it was used during the tests made after 1998.)*

The mounting of the detectors places them roughly parallel to each other, but angles of about  $1^\circ$  between the detector planes are typical. In order to take data with the tracks passing through the detectors at a specific angle the entire telescope was turned. In this way, only one set of alignment constants had to be determined with the telescope frame as reference. In order to be able to access the largest possible angle, while still having the tracks pass through all detector planes, the detectors were moved as close together as the mechanics allowed. In practice, the largest achievable angle was roughly 9 degrees.

### 5.1.2 Efficiency measurement

The efficiency was measured by fitting a track in 5 out of the 6 detectors, interpolating on the remaining detector, and looking for a cluster on that detector. Only clusters within 1 mm of the point of interception are considered. As there are only two detectors measuring the same coordinate as the detector under study, events were selected with one hit only in both of these detectors, thus avoiding the possibility to form wrong combinations. The signal to noise cut for this study was set to 15. The most probable value of the Landau observed in the detectors had a signal to noise of about 50.

The efficiency measured in the central  $R$  and  $\phi$  detectors is presented in Figure 5.2 for bias voltages of 55 V to 100 V. The maximum efficiency is obtained at 90 V bias. A part of the observed inefficiency is due to dead and noisy channels. When accounting for them, the efficiency is constant down to about 70 V but the number of dead and noisy channels increases on the  $R$  detector below 90 V.

When the bias voltage is decreased, the inefficiencies first appears on the  $r$  detector, and only in limited region as can be seen in Figure 5.3. This suggests that this effect is due to variations in the silicon quality leading to somewhat different depletion voltages depending on the position on the wafer.

### 5.1.3 Resolution measurements

In the track fit, the position of the clusters on the telescope detectors is given by the weighted mean of the strip positions, where the weight is determined according to the charge signal on each strip belonging to the cluster. The position resolution of a cluster on a detector depends on the number of strips in the cluster. For a cluster with two or three strips, the weighting improves the cluster position. For a large numbers of strips, the signal-over-noise level on individual strips may drop below threshold, and the resolution is expected to deteriorate.

The average position resolution of a silicon detector is then a function of the angle  $\alpha$  of incidence of the particle, as the charges are collected perpendicular to the detector plane, and with increasing angles, the average number of strips per

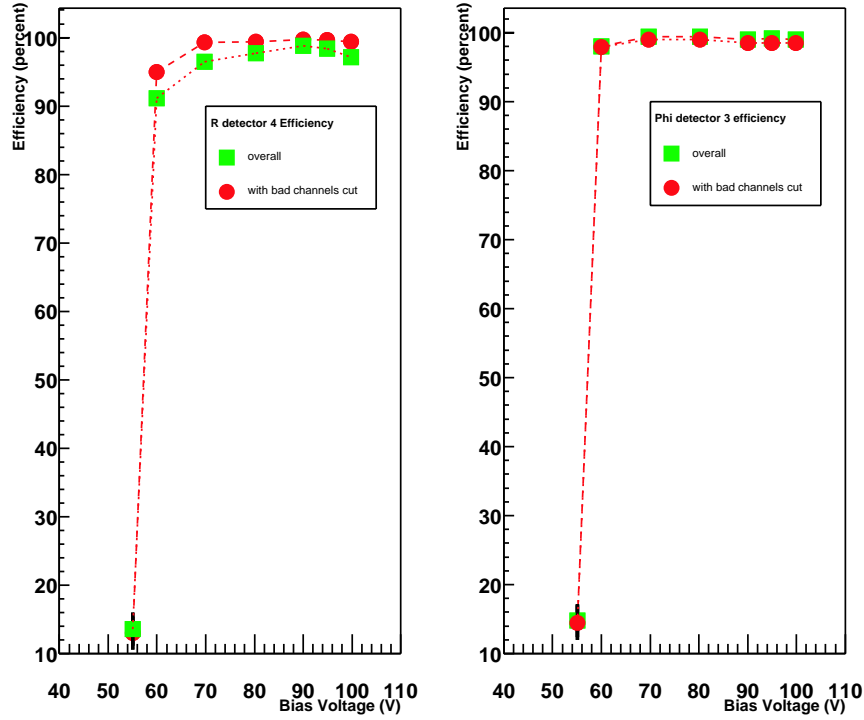


Figure 5.2: *The cluster finding efficiency as a function of bias voltages for R and  $\phi$  detectors.*

cluster also increases. In the following, we will use the *projected angle*  $\alpha_p$  as the relevant parameter:

$$\tan \alpha_p = \frac{l_p}{d},$$

where  $l_p$  is the distance perpendicular to the strip between the entry and exit points of the particle traversing the detector, and  $d$  is the detector thickness.

In order to take into account the relative detector resolutions for each track, an iterative procedure was used which is described in [43]. As this procedure requires to know the resolution for any value of  $\alpha_p$ , the data are fitted with the following function to be able to interpolate the resolution:

$$\sigma(y) = \frac{a}{\alpha_p^2 + b} + c\alpha_p,$$

where the parameters  $a$ ,  $b > 0$ , and  $c$  are to be determined.

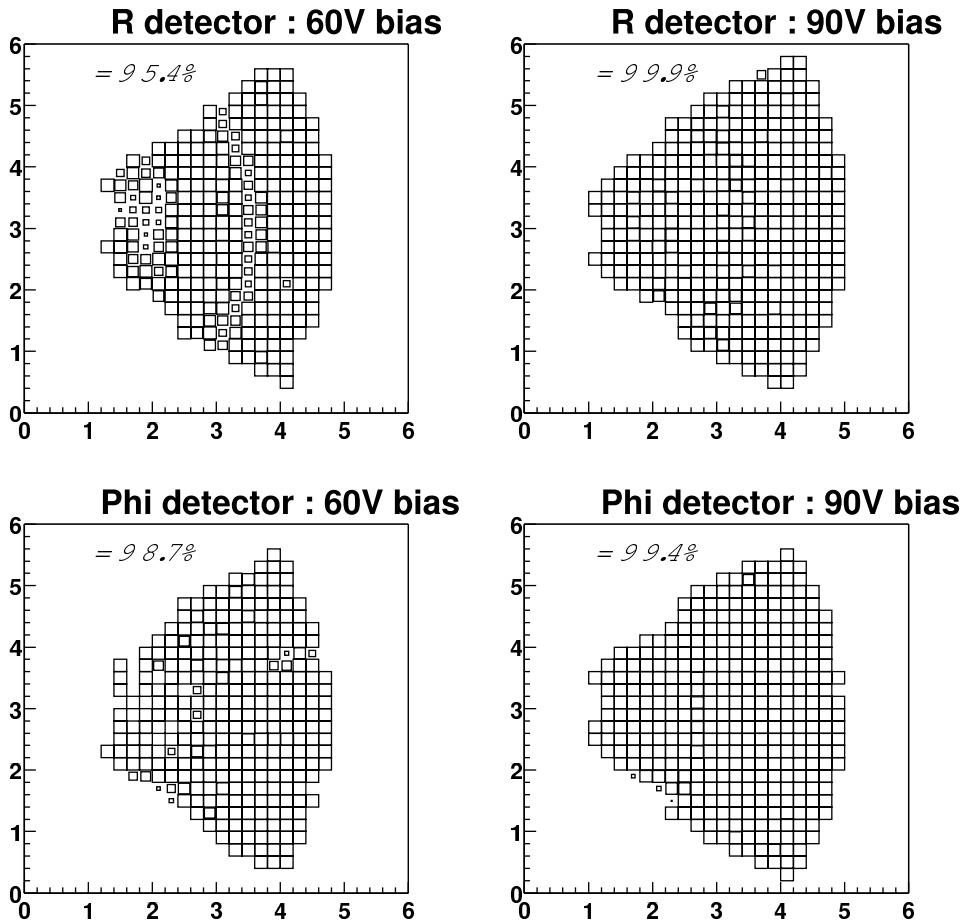


Figure 5.3: The cluster finding efficiency as measured on the central  $R$  and  $\phi$  detectors for 60 V and 90 V bias. On each plot, the horizontal and vertical axes indicate the local coordinates on the detector in cm, while the area of the boxes in the histogram is proportional to the efficiency at a given location. The mean efficiencies (integrated over the detector area) after accounting for the dead and noisy channels are indicated in the plots of Figure 5.2.

The resulting resolution functions are presented in Figure 5.4 for both pitch regions of the  $R$ -measuring sensors. The best resolutions obtained are the following:

strip pitch	projected angle	resolution
40 $\mu\text{m}$	80–120 mrad	3.6–3.9 $\mu\text{m}$
60 $\mu\text{m}$	$\geq 200$ mrad	4.0–4.6 $\mu\text{m}$

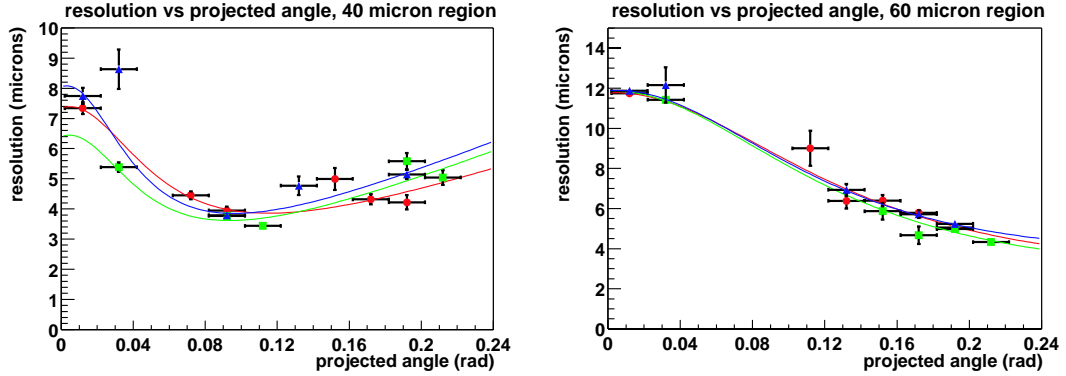


Figure 5.4: *The resolution as a function of the projected angle for the 40  $\mu\text{m}$  and 60  $\mu\text{m}$  pitch regions. The results for the three detectors are shown superimposed. Note that the information from the three detectors is not independent.*

#### 5.1.4 Measurement of charge sharing

The non-zero capacitance between adjacent strips leads to charge sharing, which in turn affects the fraction of clusters that contain a given number of strips for particles traversing the detector at a given projected angle. The charge sharing fraction  $x$  is defined such that on a given strip, only a fraction  $1 - 2x$  of the charge is measured, while the two adjacent strips measure a fraction  $x$  each if otherwise no charge was deposited there.

The charge sharing fraction has been measured by fitting tracks through five detectors of the telescope, excluding the central  $R$  detector. The tracks are then extrapolated to this detector. Tracks are selected if the projected angle at the point of intercept with the middle  $R$  detector is smaller than 50 mrad and if they pass through the centre of the region between two strips, i.e. if their distance to either strip is more than 40% of the strip pitch. These two strips are called *near* strips in the following. This selection ensures that for the two *far* strips that have a distance from the track of  $\sim 1.5$  times the strip pitch, the probability to collect charge deposited by the traversing particle is small. This was confirmed by the absence of dependence of the charge sharing on the projected angle.

Each of these two near strips is considered in turn if their ADC value is greater than 20. For lower ADC values, the information on the charge sharing is diluted by noise. The value of the charge sharing fraction  $x$  is then measured from the ADC values on the near strip and the adjacent far strip as follows:

$$x = \frac{\text{ADC}_{\text{far}}}{\text{ADC}_{\text{near}} + 2\text{ADC}_{\text{far}}}.$$

The resulting charge sharing fractions are:

$$x(40\mu\text{m}) = (5.3 \pm 0.3)\% \quad \text{and}$$

$$x(60\mu\text{m}) = (4.7 \pm 0.1)\%.$$

## 5.2 Experimental set-up

The various set-ups used for the testing of the VELO prototype sensors are very similar and in particular the acquisition system retained the same structure. The logic and the number of ADC modules were the main changing parts. Figure 5.5 shows a schematic of the DAQ. The detector set-up used for the first test of the fast readout chips is presented in Figure 5.6. Finally, Figure 5.7 shows the setup used for the irradiated silicon tests. The main thing to note about these last two figures is the addition of a second telescope station, which incorporates a fast readout. The purpose of this station is two fold:

1. to improve the precision of the extrapolated track on the test detector,
2. to determine which track was “in time” for the fast readout of the test detector.

The telescope used was one half of the 1998 prototype of the VELO which was presented in Section 5.1. It is made of three stations of one  $R$  and one  $\phi$  sensor. Both sensors are flipped from station to station. The telescope is readout by a set of VA2 chips operated at 5 MHz with an integration time of 1  $\mu\text{s}$ .

The test sensors in all experiments as well as the fast station used in the silicon tests were readout with SCT128A chips [3]. The chips were running at the nominal LHC clock rate of 40 MHz with an integration time of 25 ns. However, the digitisation was only done at 5 MHz.

The detector of interest during the irradiated silicon tests was operated in a cool box where the temperature was kept at  $-10^\circ\text{C}$ .

The data acquisition system is made of a series of VME modules:

- A PowerPC based VME-bus controller drives the whole DAQ system.
- A sequencer (SEQSI) is used to generate the various clocks and control signals.
- A Time Digital Converter (TDC) is used to record the time of the scintillators trigger up to a precision of 1 ns.
- A set of Analogue Digital Converters (ADC) sample the data sent by the various readout chips.

and a few NIM modules for the trigger logic.

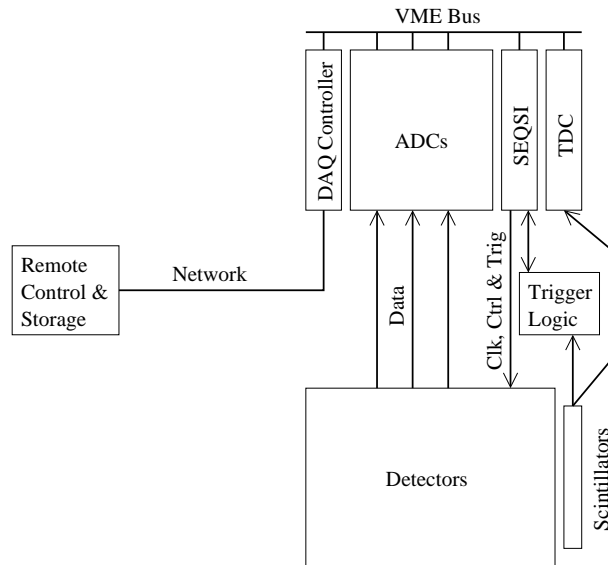


Figure 5.5: Schematic view of the data acquisition system used for the VELO testbeams.

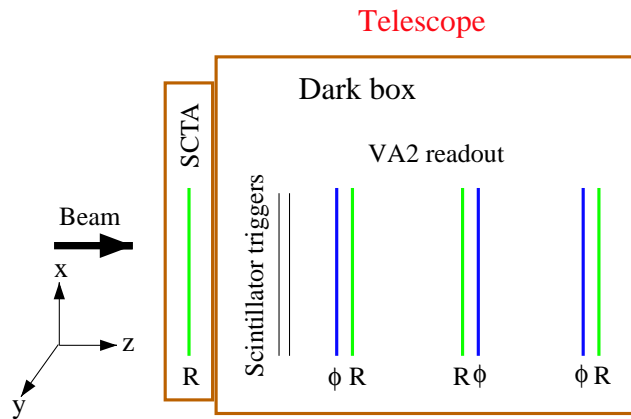


Figure 5.6: Detector layout used for the SCT128A testbeam.

### 5.2.1 Data acquisition system

While the CPU embedded in the DAQ controller plays a very important role, the heart of this system is actually the sequencer. The timing of the many different signals is very important for both the quality of the sampling of the ADCs as well as the correct operation of the fast readout chips.

The SEQSI module provides 24 independent channels plus 4 clock lines and a



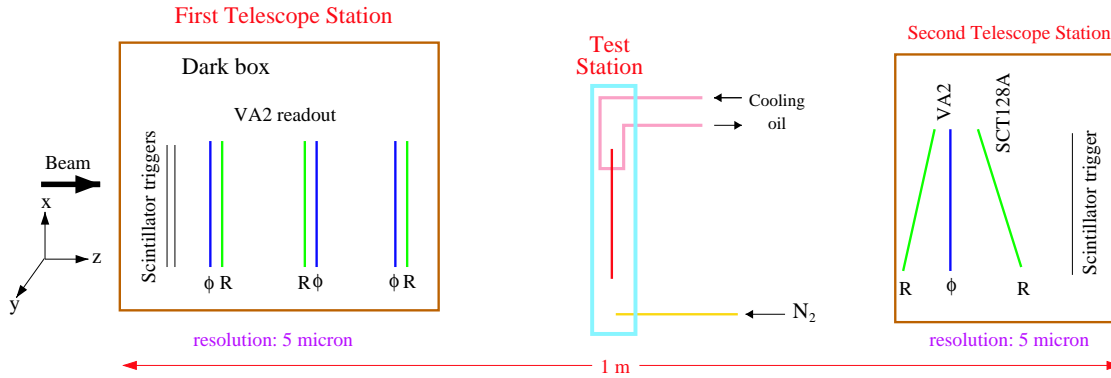


Figure 5.7: Set-up of the detectors used for the irradiated silicon testbeams. The sensor under test is in the middle of the two solid state telescopes.

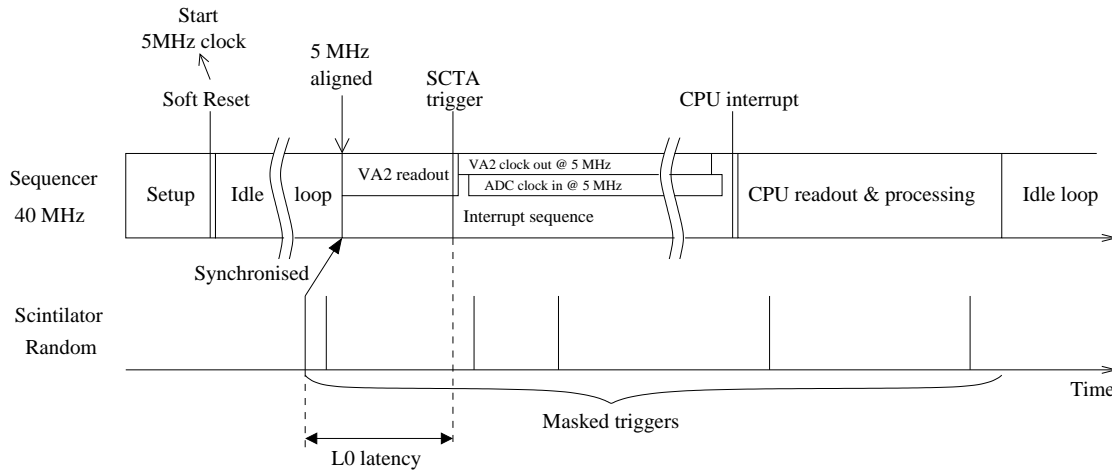
few more special signals to control some functionality. Any number of sequences (up to the limited RAM available in the module) can be pre-loaded in the SEQSI. However only two sequences are available during normal operation, one *loop* sequence and one *interrupt* sequence. By preceding the loop sequence by an initialisation sequence in the SEQSI's memory, one can have a third functional sequence. The start address of both the loop and the interrupt sequences are set by two registers. The end of any sequence must be flagged by either the “stop clock” bit of the “jump” bit one clock cycle before the end of the sequence (forgetting the jump bit will give strange results as the sequencer will run past its memory, mess around with its clock and restart from address zero). When the sequencer sees the jump bit it will load its address register with the content of the “loop start” register. Turning on the clock will start playing the sequence at any pre-set address incrementing the address at each clock cycle. This is how an initialisation sequence can be made. When an external trigger is received, it is first synchronised with the internal clock and then the interrupt sequence address is loaded. This two step process implies that two clock cycles are required to enter the interrupt sequence.

In addition to the constraint of the sequencer itself, the length of all the cables must be taken into account when building the sequence to drive and readout the detectors. In summary the full sequence pre-loaded in the SEQSI is

1. Initialisation. The fast readout chips (SCTA) are reset and loaded with the operational settings. Their internal counters are reset (“soft reset”).
2. “Idle” loop. While waiting for the trigger, the system would usually run into a rather simple loop. However, this sequence is more complex as it must take the following things in account:

- As the sequencer takes two clock cycles to execute the jump, the idle loop cannot be shorter than that.
  - The SCT128A uses an internal counter to produce the 5 MHz clock required for the output of the analogue data. This internal clock is started by the soft reset sent during the initialisation. In order to make sure that the analogue data reaches the ADC at a fixed time, the trigger must be synchronised to this 5 MHz clock. This implies that the idle sequence must be 200 ns long and it must provide some signals for the trigger synchronisation.
  - As the SCT128A was designed for fast readout, its integration time is very short. Accepting any trigger in the 200 ns window of the idle sequence will kill the amount of useful data as the readout will be in time only 1/8 of the time! So an additional “trigger accept” signal is produced by the idle sequence and or-ed with the incoming trigger. For the purpose of the pulse shape study, this trigger accept can be moved/enlarged to fully scan the pulse shape.
  - The SEQSI doesn't provide a convenient way to block any further trigger from re-starting the trigger sequence. To prevent any restart of the trigger sequence, the accepted trigger is latched and used as a busy signal until the new sequence is entered.
3. Detector readout. The trigger sequence of the SEQSI is used to instruct the slow readout chip to read the detector and then all the chips are required to send the data. The 5 MHz sampling clock used by the ADC is also provided by this sequence. It turned out that daisy chaining the chips introduces a small dead-time between the chip data that the sampling clock must take care of. A busy signal to veto any new trigger is also sent. Finally an interruption is sent to wake-up the CPU in order to flush the ADCs to disk.

Once the interrupt generator module is activated, it will raise a busy signal and signal the CPU that data are ready to be processed. The DAQ controller will then read the ADCs and the TDC, decode the SCT128A calibrations and trailer data, and pack the data in a specific format. Next the event is passed to the storage layer which sends them to the remote control and storage unit. And finally, the ADCs, TDC and the interrupt module busy signal are cleared allowing the system to accept a new trigger. The DAQ controller software uses the Cascade framework [44] which provides remote monitoring and control. The final event rate achieved was of the order of 15 Hz with a peak value of  $\sim 25$  Hz.

Figure 5.8: *Schematic of the DAQ timing.*

### 5.2.2 The SCT128A read-out chip

The radiation hard environment, in which the VELO will operate, makes it impossible to digitise the collected charge in place. For this reason, the detector will use an analogue read-out. The so-called *front-end* electronic, which will be placed inside the tank of the VELO, will have to send the collected charges a few meters away to the repeater boards which will then send them through a series of differential lines some 60 meters away in the radiation free area. Once in this area the data will be received by the *off detector electronic* (ODE) for digitisation and it will check the data integrity for possible lose of synchronisation.

As the VELO is made of more than 200'000 strips of less than  $100\ \mu\text{m}$  wide, attaching a cable to all of these strips to read-out the detector is clearly impossible for space reasons. The chosen solution is to collect the charges deposited in 32 channels and send this information through a serial line. Sending 32 such analogue samples in 25 ns is actually impossible. Hopefully, only a few of the bunch crossings will deposit valuable information in the detector. The Level-0 of the trigger is here to flag these interesting events, reducing the event rate down to roughly 1 MHz.

However, the events which are accepted come randomly and the detector must really be read-out every 25 ns. In order to give enough time to the Level-0 trigger to do its job the samples pass through a pipeline in the front-end chip.

The SCT128A is a first prototype devised by the ATLAS collaboration for its Semiconductor Tracker (SCT) [45]. It provides 128 inputs to a 112-cell deep analogue pipeline terminated by a single multiplexer. The chip is made using a radiation hard BiCMOS DMILL process and was tested successfully after an irradiation of up to 10 Mrad. Its functional block diagram is presented in figure 5.9.

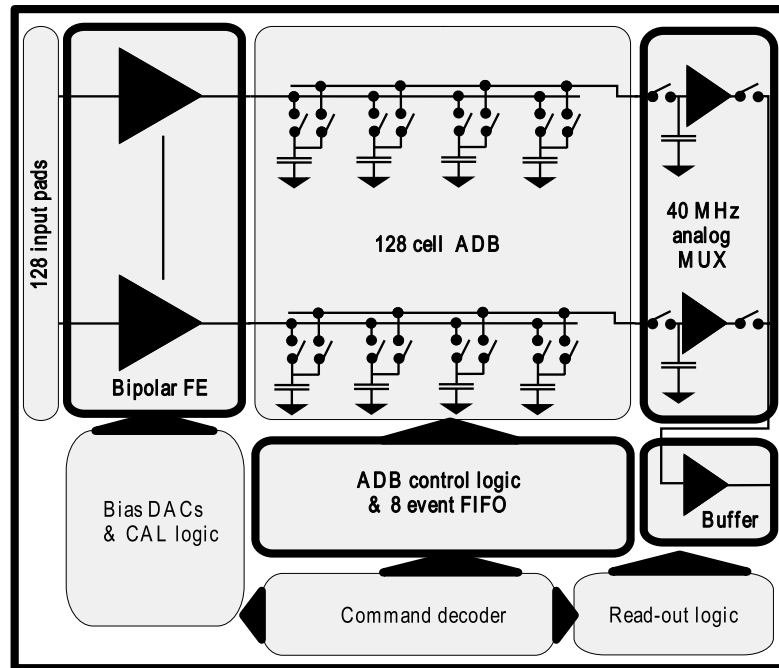


Figure 5.9: *Block diagram of the SCT128A fast readout chip [3].*

The chip operation is controlled by a reset line and two LVDS lines, one for the clock and a second one for serial commands. The description of the different instructions can be found in [3]. Two versions of the chips were available. One for low capacitance detectors (2-5 pF) and one for higher capacitance (15-20 pF).

The chip has the ability to flag up to eight events for output. Special commands can be sent to the chip to flag 4 or 8 consecutive events in addition the usual single event trigger command.

As the ODE boards must be capable to digitise the incoming signals and extract the data for the subsequent processing and storage, a pseudo-digital header and a trailer are added to the analogue data, see Figure 5.10. The header (0101) is followed by 3 calibration values representing the 0, 80% and 100% of the output range. The 128 channels of physical data are sent in sequence and finally a trailer is emitted. The trailer indicates a possible overflow of the trigger FIFO, a four bits bunch counter and a four bits trigger counter. The chip can be tuned to output the data at either 40, 20, 10 or 5 MHz. Due to the limitation of the ADCs used, the slowest setting was used during our tests.

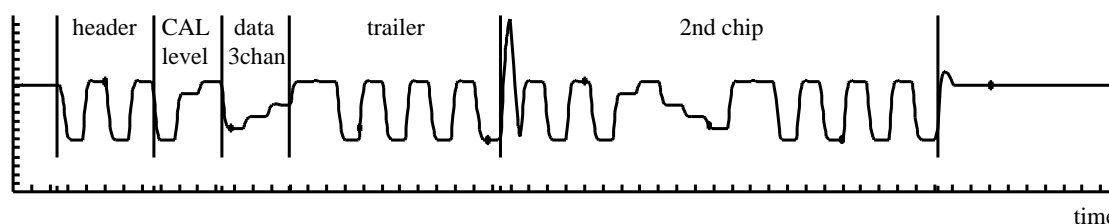


Figure 5.10: *The output of two daisy chained SCT128A chips. Only 3 of the 128 channels outputted are shown.*

### 5.2.3 Testbeam event reconstruction

#### Common mode noise suppression

The first thing done for the event reconstruction is actually a suppression of the common mode noise present in the data. This technique is based on the fact that sets of contiguous strips might have a common baseline shift (common mode, CM) due to some kind of pickup. As the occupancy of the detector will be sufficiently low, it's possible to compute a common noise level for each group of related strips. If some strips in a group have a large ADC value (be it signal or noise), it will be ignored during the evaluation of the correction to apply.

The grouping of the strips for the calculation of the CM correction is based on the routing and on the read-out chip they are connected to. Due to the rather complicated routing imposed by the strip layout on the sensors, contiguous input lines are not necessarily connected to contiguous strips. Figure 5.11 shows a schematic of the routing lines of the sensor used for the fast read-out test.

In our analysis the first 500 events are used to get an initial value of the pedestals as well as an estimate of the noise by computing the rms of the signal for each strip. Then the following steps are taken for each region of the detector, and for each event:

1. The pedestal is subtracted.
2. The mean is computed and subtracted.
3. The rms of the sample is computed.
4. A straight line is fitted to the sample, excluding channels larger than 3 times the rms, and the sample is corrected to get a flat distribution.
5. Step 3 and 4 are repeated a second time.

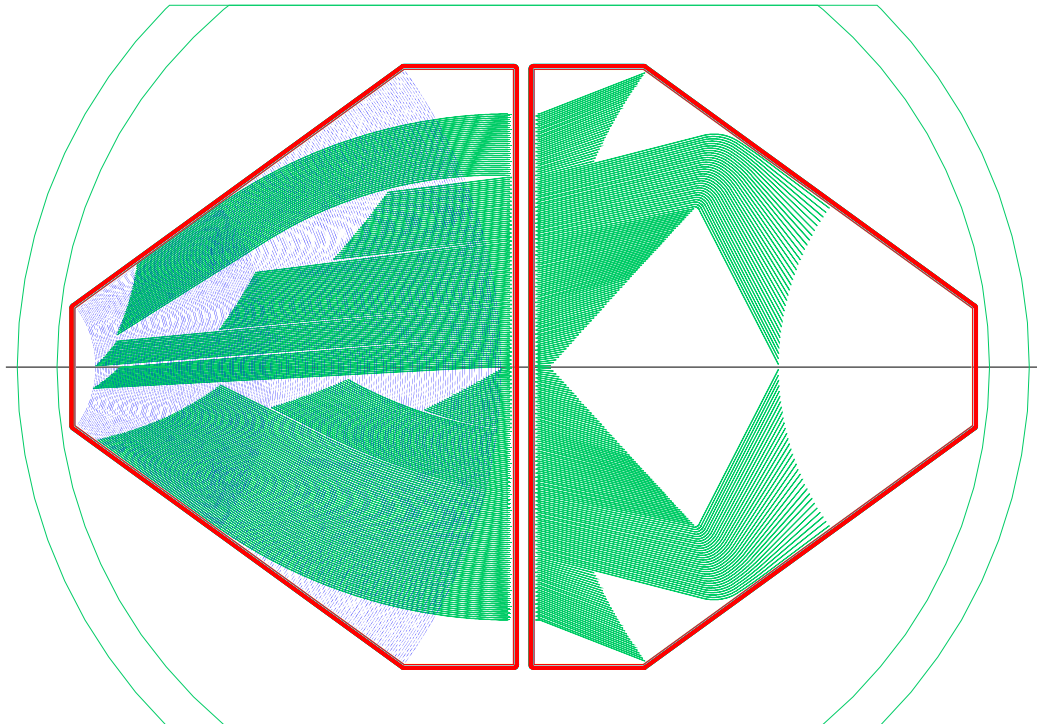


Figure 5.11: *The Hamamatsu  $R$  and  $\phi$  sensors on their production wafer. The  $R$  strips are shown in blue. The routing lines of both sensors are presented in green.*

6. The average common mode noise of each strip is updated if the signal is less than 3 times the previous value and the signal-to-noise for this event is computed.
7. Finally, the pedestal is updated.

### Cluster finding

After the data has been improved by the common mode correction procedure, clusters are created. The clustering is done by first sorting the channels by signal-to-noise and then, starting from the highest  $s/n$ :

1. If the next available channel has a  $s/n$  less than a given cut, the process stops, otherwise the channel is flagged as used.
2. The neighbouring channel on both side is retrieved and compared to the central one. If it is above the  $s/n$  cut or if it's above 10% of the central channel signal, it is added to the cluster and flagged as used.

3. The next pair of neighbouring channels is processed in the same way.
4. The cluster position, signal and noise are computed.
5. The process goes back to point 1.

While the procedure is rather simple, it has some evident problems. The notion of neighbouring strip is not obvious due to the special routing of the strips to the read-out chips, especially in the case of the  $R$  detector. The strips of the central part of this detector are split in two. So at the boundary between the split strips and the non-split strip, the two inner most non-split strips have two possible neighbours. It's important to handle this correctly otherwise any particle passing in this small region may create clusters from two strips which are not close to each other. Indeed, the outermost cluster can be combined with any  $\phi$  hits while the inner cluster overlap only half of the  $\phi$  strips.

### Alignment

The last step before tracks can really be reconstructed is to translate the position of the clusters from their local sensor frame to the global detector frame. The parameter of this transformation are known with some precision from metrology.

The future positioning of the VELO sensors will not be measurable with great precision as the detector will be moved out during the injection of the beam and back in place after that. These small movements ( $\sim 3$  cm) will defeat any precise alignment due to the vibrations.

To account for these limitation, the detector will be aligned using tracks and the same procedure was applied to the testbeam set-up. Events without reconstruction ambiguities are selected from the data and then a fitting procedure is applied with some alignment constraint as free parameters (for more details see [46]).

## 5.3 SCT128A signal shape study

The shape of the signal as seen by the read-out chip is very important for two reasons, if the signal lasts too long it will be seen in the next event (overspill), and due to the fast shaping time a badly timed sampling point will significantly degrade the signal. The complete study is available in [4].

The charge signal as seen by the SCTA chip is parameterised as a flat pulse. The relevant parameters are the rise time  $t_{\text{rise}}$ , the width of the plateau  $t_{\text{plateau}}$  and the fall time  $t_{\text{fall}}$ . While this is only a crude approximation it describes the observed SCTA output well and is sufficient for the purpose of this analysis. The

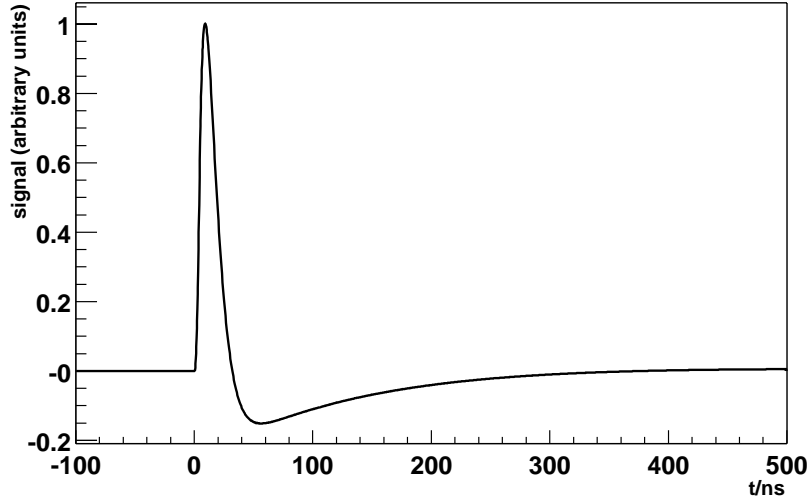


Figure 5.12: *The expected time domain response of the SCTA readout chip to an input signal corresponding to rise time of 1ns; a plateau of 5ns; and a fall time of 1ns. The poles of the SCTA circuit have been set to  $a = 1/7$  GHz and  $b = 1/180$  GHz.*

Laplace transform is given by

$$F_{\text{pulse}}(s) = \frac{1}{s^2} (1 - e^{-t_{\text{rise}}s} - e^{-(t_{\text{rise}}+t_{\text{plateau}})s} - e^{-(t_{\text{rise}}+t_{\text{plateau}}+t_{\text{rise}})s}).$$

The readout circuit can be parameterised to a good approximation by two poles, giving rise to a bipolar output pulse shape. Thus, the Laplace transfer function is given by

$$F_{\text{transfer}}(s) = \frac{s^2}{(s+a)^2(s+b)^2},$$

where  $a$  and  $b$  denotes the frequencies corresponding to the two poles.

The Laplace output response is obtained as the product  $F_{\text{output}} = F_{\text{pulse}}F_{\text{transfer}}$ . The inverse of this function gives the time domain response:

$$o(t) = k(t) - k(t - t_{\text{rise}}) - k(t - t_{\text{rise}} - t_{\text{plateau}}) + k(t - t_{\text{rise}} - t_{\text{plateau}} - t_{\text{fall}})$$

where

$$k(t) = \left( \frac{2}{(a-b)^3} e^{-at} + \frac{1}{(a-b)^2} t e^{-at} + \frac{2}{(b-a)^3} e^{-bt} + \frac{1}{(b-a)^2} t e^{-bt} \right) H(t)$$

with  $H(t)$  the unit step function.



The resulting expected pulse shape is illustrated in Figure 5.12. On the figure an undershoot is clearly visible. In order to measure the pulse shape down to these signal values, the clusters cannot be used. The detector strip signals (after common mode correction) were used directly. The reconstructed tracks from the telescope were extrapolated to the test detector and the charge of the strip in a small region around this point were summed (see Figure 5.13 which shows a testbeam event). The number of strips to use was determined after aligning the test detector and by using the resulting precision. The number of strips retained was 8 but the analysis was redone with only 6 strips with consistent results.

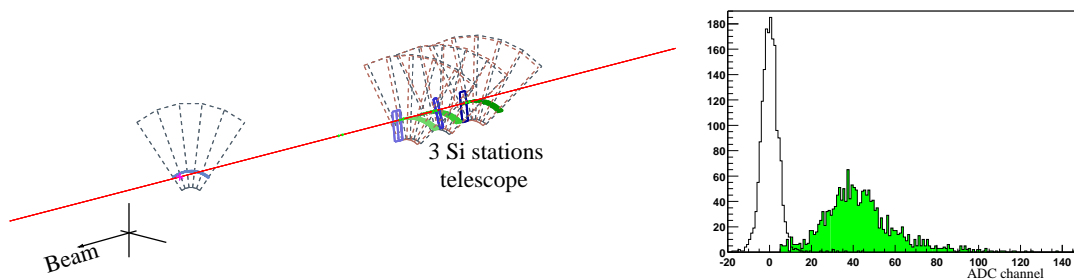


Figure 5.13: *Left: a beamtest event. The telescope allows the determination of the impact point on the sensor under test. The line corresponds to the inferred trajectory of the particle. Right: amplitude spectrum. The Landau shape is obtained by requiring the hit to be in coincidence with the extrapolated track, the pedestal by requiring the anti-coincidence.*

The time scan required for this analysis was provided by the absence of synchronisation between the CERN SPS beam and the DAQ clock combined with the length of the SPS bunches.

The resulting pulse shape of this analysis are shown in Figure 5.14 for a 200 V bias and for differently irradiated regions of the detector. The detector used was a  $300\ \mu\text{m}$  thick  $n$ -on- $n$   $R$ -measuring sensor identical to those used in the testbeam telescope.

From the fitted shape, it was possible to conclude that the SCT128A satisfies to the criteria of the experiment with less than 30% of the signal in the overspill while loosing at most a few percent of the signal at the sampling point and this even in the case of a highly irradiated detector. Table 5.1 gives the range of sampling time relative to the maximum of the signal for an overspill of 30% and for the different level of irradiation.

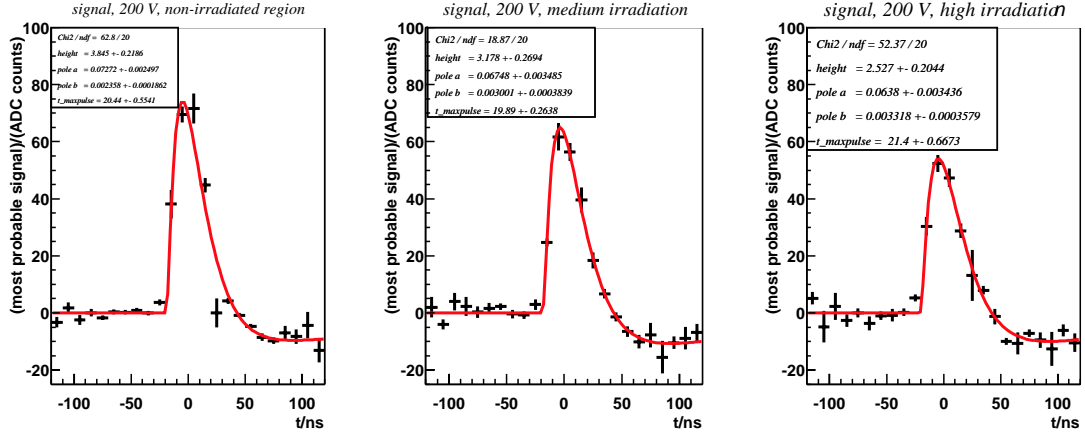


Figure 5.14: *The most probable signal values as a function of the readout time, separately for the non-irradiated and irradiated regions of the detector. The results of fits to the distributions are superimposed. [4]*

$\langle \text{dose} \rangle = 0$	
readout time	signal fraction
$t_{\min} = -1.3 \text{ ns}$	100%
$t_{\max} = 14.2 \text{ ns}$	58%
$\langle \text{dose} \rangle = (1.28^{+0.39}_{-0.35}) \cdot 10^{14} \text{ n}_{\text{eq}}/\text{cm}^2$	
readout time	signal fraction
$t_{\min} = 0.4 \text{ ns}$	97%
$t_{\max} = 8.9 \text{ ns}$	75%
$\langle \text{dose} \rangle = (2.07^{+0.42}_{-0.43}) \cdot 10^{14} \text{ n}_{\text{eq}}/\text{cm}^2$	
readout time	signal fraction
$t_{\min} = 0.3 \text{ ns}$	94%
$t_{\max} = 7.4 \text{ ns}$	77%

Table 5.1: *The range of readout times for which the overspill fraction is less than 30%. min and max reflect the evolution of the allowed timing due to the variation in the capacity of the strips on the detector and thus the pulse shape.*

## 5.4 Performance of irradiated sensors

The selection of the technology used for the silicon micro-strips sensor is based on the evolution of the operational parameters as a function of the radiation dose

absorbed. Especially, the longer the lifetime of the sensors, the lower the number of times it will be needed to replace them thus reducing the cost. The following sub-sections will present the methodology and results obtained for the testing of the first two VELO prototypes [47, 48].

### 5.4.1 Sensors description

The first prototype is a  $n$ -on- $n$  design with individual  $p$ -stops and a thickness of  $300\ \mu\text{m}$  manufactured by Hamamatsu Photonics. Figure 5.15 shows the layout of the strips on both the  $R$  and  $\phi$  sensors. For the performance test, a  $\phi$  sensor was irradiated in the CERN PS facility with 24 GeV protons to a peak fluence of  $4.1 \pm 0.4 \cdot 10^{14}$  protons/cm<sup>2</sup>. The operational peak fluence, at the inner radius of the detector, is expected to be less than  $2 \cdot 10^{14}$  protons/cm<sup>2</sup> per year.

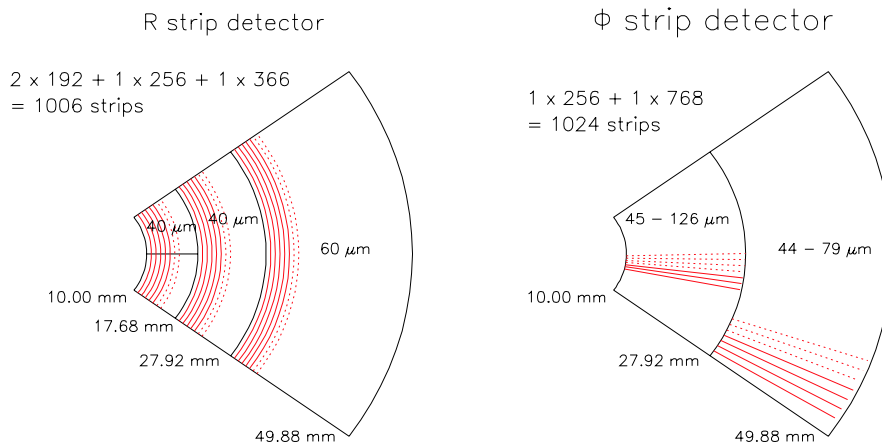


Figure 5.15: *Strip layout of the Hamamatsu prototype detectors. Both design were used for the telescope. The irradiated test sensor was of the  $\phi$  design.*

Only four regions of the detector were read-out by the SCT128A because no hybrid was available for this specific design. Figure 5.16 shows the locations of these regions with respect to the irradiated area. The size of the shaded squares is proportional to the dose received.

The second sensor tested was produced by MICRON Semiconductors. It is a  $p$ -on- $n$  design with a thickness of  $200\ \mu\text{m}$ . The strips from the inner region were connected to the read-out pads using routing lines on a second metal layer. Its irradiation and read-out map is presented in Figure 5.17.

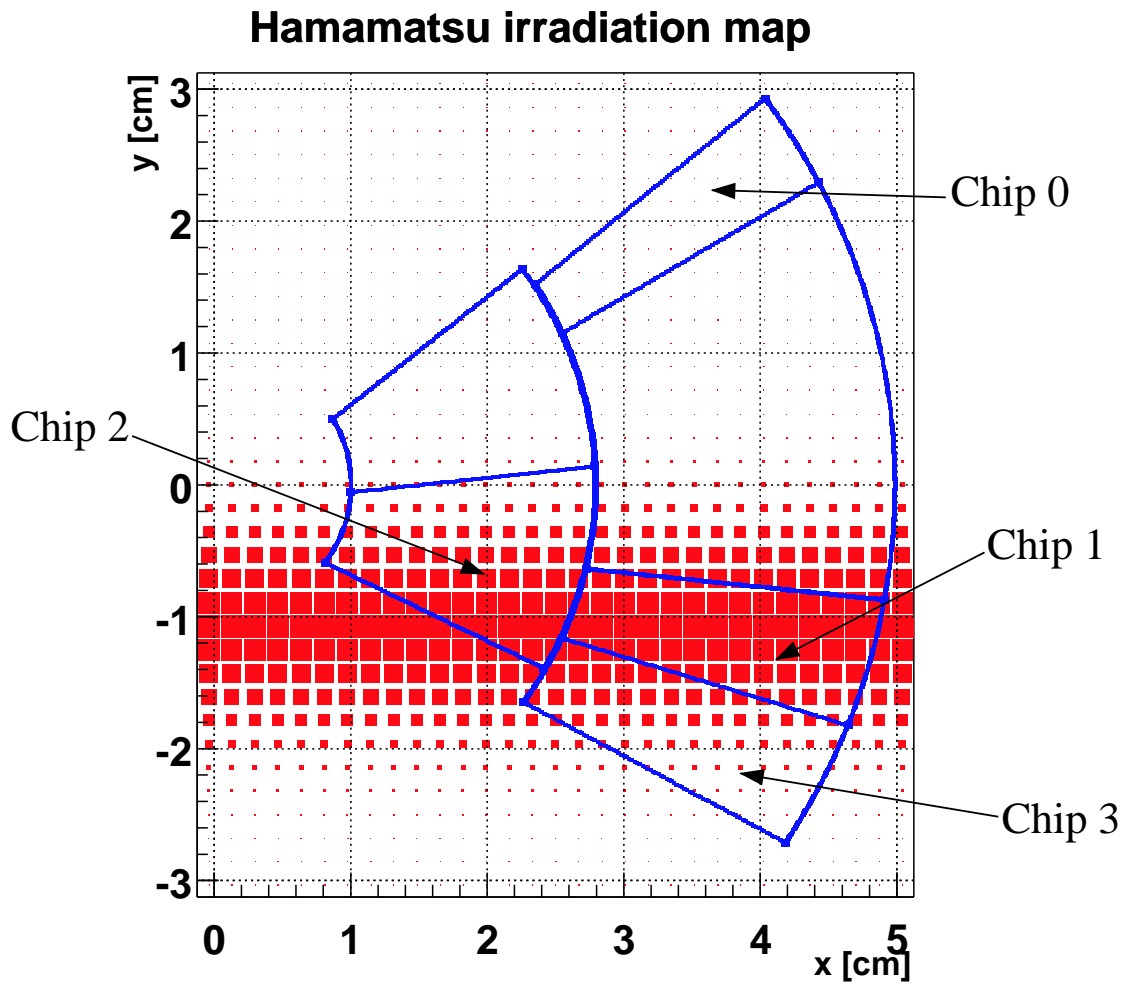


Figure 5.16: *Positions of the instrumented regions of the test detector with the received irradiation dose superimposed.*

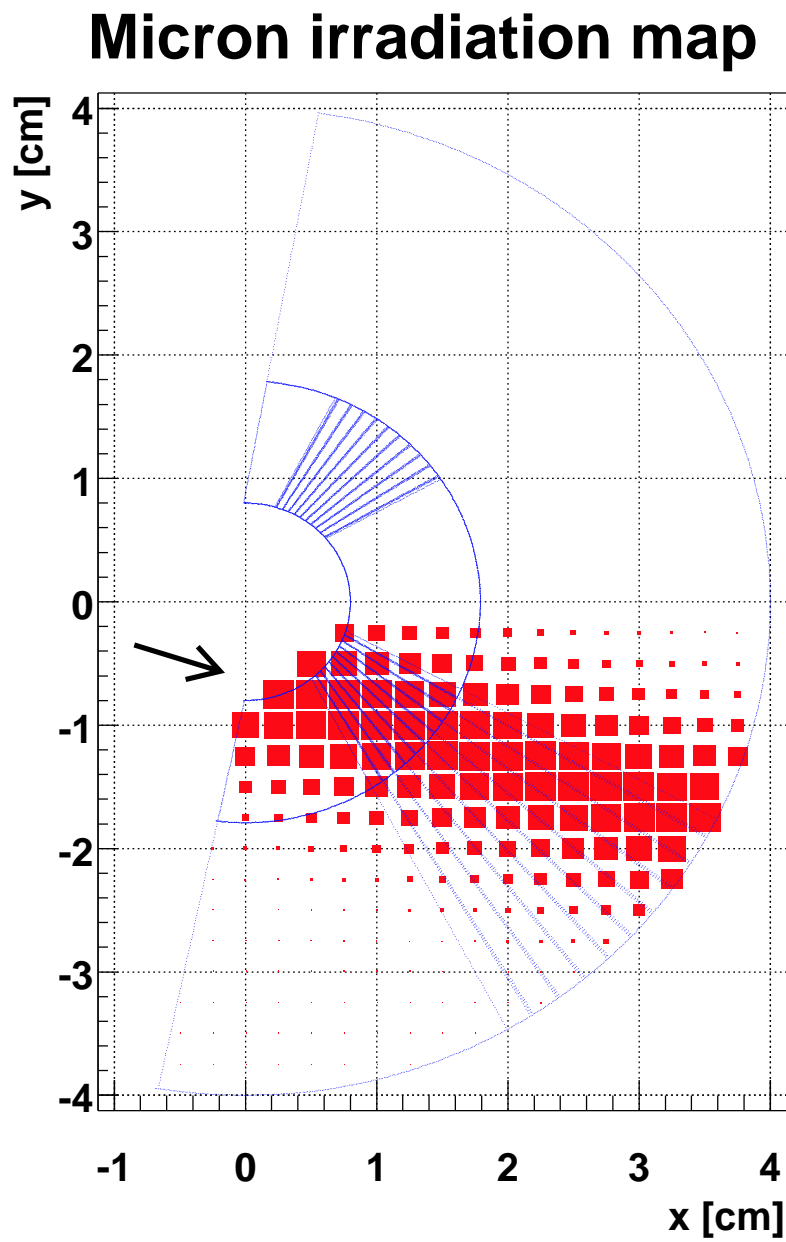


Figure 5.17: *The irradiation map of the Micron test sensor. Some strips are drawn in the region which were read-out.*

### 5.4.2 Performance measurements

To evaluate the performance of the sensors the following parameters were measured:

- charge collection efficiency (CCE),
- cluster finding efficiency,
- cluster shape,
- signal to noise ratio.

#### Hamamatsu detector

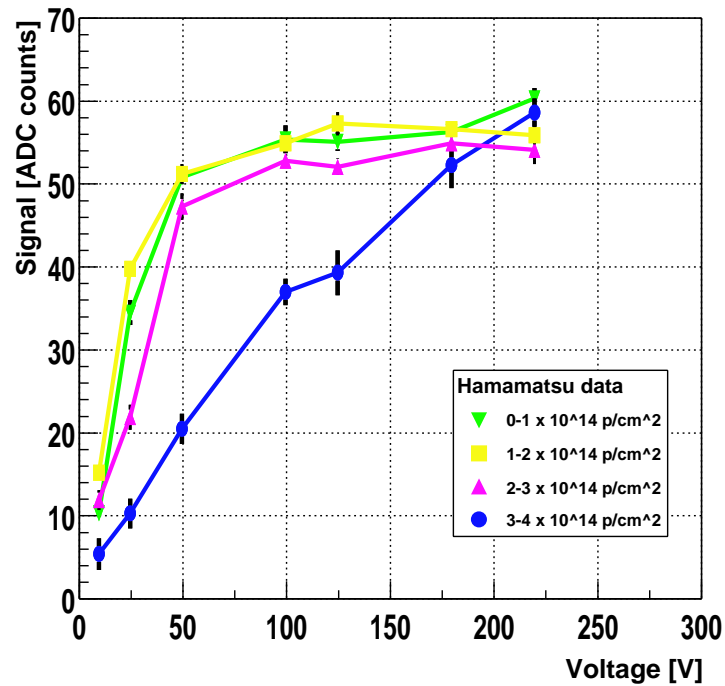


Figure 5.18: Charge collection efficiency of the Hamamatsu prototype as a function of the bias voltage for different radiation doses.

**Charge collection efficiency** The charge collected on the irradiated detector was measured by summing the signal in strips around the intercept point of an extrapolated telescope track. The CCE was measured both as a function of the

irradiation and of the voltage. As the second telescope station increased the precision on the extrapolation point only 5 strips were needed.

In the lowest irradiation region, the full charge collection was reached at 50 V volts and 220 V were needed for the high irradiation region. For the non irradiated region, no direct results were obtained as the read-out data exhibited strange properties: the signal shape was different and shifted by 10 ns, the amplitude lower and the noise was larger. As no explanation was found the data provided by the timing detector in the second telescope station was used to determine the maximum CCE. An average of  $58.5 \pm 3$  ADC counts from the peak of the Landau distribution was measured (the error includes the uncertainty on the chip gain).

**Cluster finding efficiency** The most relevant quantity is the efficiency with which a cluster can be reconstructed. The clusters are formed from the pedestal subtracted and common mode corrected data. The central strip must have a signal-to-noise greater than 1.5. Neighbouring channels with a signal-to-noise exceeding 10% of that of the central strip were added to the cluster. Up to two such strips on each side were included.

For the study, the reconstructed clusters were accepted if they were within 200  $\mu\text{m}$  of the position predicted by the telescope. For a cluster signal to noise cut of 3, the probability of accepting a fake cluster is approximately 20% and the full efficiency is obtained after only 50 V even for the most irradiated region.

**Cluster shapes** The intrinsic resolution of the detector is related to the division of charge between strips and thus to the cluster shape. The larger the spread, the lower the resolution.

Cluster were formed by summing the charges of the 2, 4, 6, 8, 10 or 12 strips closest to the extrapolated track intercept point. The data were divided into different levels of irradiation dose and only the part of the data corresponding to the finest pitch (down to reasonable statistics) was selected. To account for the different pitch size and make results comparable, the cluster extent was defined as the number of strips summed over multiplied by the mean pitch for the region studied.

Figure 5.19 shows that the cluster extent distribution as a function of the voltage is nearly flat for both the low and high irradiation region. Hence, it is concluded that the intrinsic resolution for this prototype detector is not degraded by the sharing between strips.

**Signal-to-noise performance** As the cluster finding relies on the signal to noise ratio to select interesting strips, its evolution under irradiation and depletion voltage is of great interest.

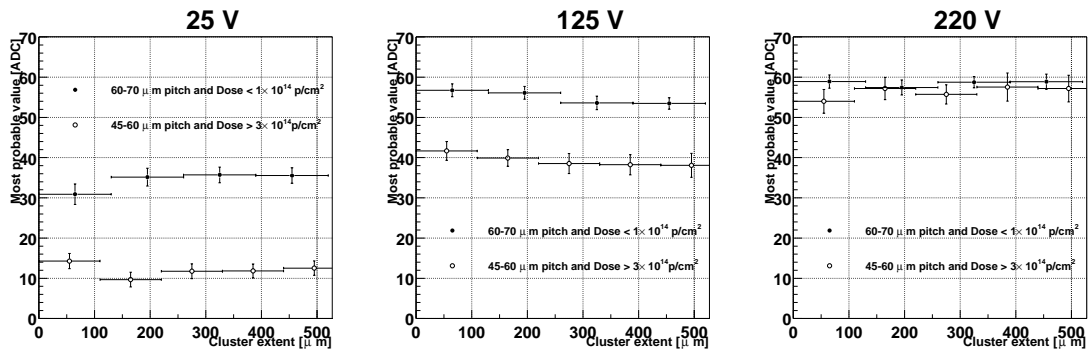


Figure 5.19: *The cluster extent of the Hamamatsu detector at different voltages: left 25 V, middle 125 V, right 220 V.*

The study was performed by selecting event within a  $\pm 1$  ns period from the estimated maximum signal point. The fit of a pseudo-Landau to the data collected at 220 V gives a most probable signal value of 58 ADC counts. The measured common-mode suppressed noise was 2.7 counts and was stable for all voltages. As a result, the signal-to-noise ratio for the over depleted detector was measured to be 21.5 ADC counts.

As no tracks passed in the region read-out by the chip 2, this region was not used for tracking. However, examining its noise was instructive. At a bias voltage of 100 V a group of 25 channels started to exhibit a large noise. Treating these channels separately didn't improve the common mode noise suppression, in both cases the whole chip was slightly more noisy. With the increase of the depletion voltage, the chip performance degraded.

The exact origin of this behaviour is unknown but similar problems have been observed in ATLAS *n-on-n* prototype detectors. This behaviour is attributed to certain strips exhibiting micro-discharge noise after irradiation. This is known to be a particular risk for the *n-on-n* detectors where the field develops from the segmented side of the detector after type inversion and high field regions can appear, for instance at the *p*-stops. There are various design techniques which can protect against this such as the use of *p*-spray and/or field plates. Also the presence of bad channel ("pin-hole") leading to a large current into the chip is not excluded at least for the block of very noisy channels.

**Conclusion** The results show that the *n-on-n* design will survive for at least 2 years in LHCb conditions with negligible deterioration. Due to the safety factor given by the fact that the sensor appears fully efficient even when at  $\sim 40\%$  under-depletion, 3-4 years operation could be safely envisaged.



### Micron detector

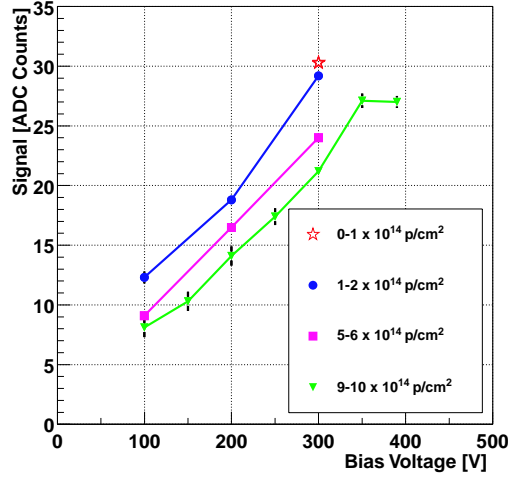


Figure 5.20: Charge collection efficiency of the Micron detector as a function of the bias voltage for different irradiation levels.

**Charge collection efficiency** The procedure for the measurement of the charge collection efficiency of the *p-on-n* Micron detector is slightly different from the one used for the Hamamatsu prototype. When the bias voltage is insufficient, the charges will recombine in the undepleted region before reaching the strips as the field is much weaker. The fact that this detector uses a second metal layer allows some charges to be collected by the routing lines instead of the strips, especially when the charges are located in the middle of two strips. So the measuring of the CCE was done by summing the charge from the 5 strips and the routing lines above them about the intercept point of the track.

On the non irradiated side, the maximum CCE was reached at 300 V and was of only 30.3 ADC counts. In comparison the Hamamatsu detector gave a signal of 58.5 counts. However the Micron detector is only 200  $\mu\text{m}$  thick instead of 300  $\mu\text{m}$  for the Hamamatsu detector, thus giving 40 ADC counts after re-scaling. The observed decreased performance of 25% is much larger than the 5% gain variation of the SCT128A and no other explanation has been yet found.

While the low irradiation region reached the maximum CCE at 300 V too, the most irradiated region reached 93% of the maximum CCE by 350 V.

**Cluster finding efficiency** The charge loss mentioned in the previous paragraph leads to a separate study of the cluster finding efficiency for the inner region

(without the second metal layer) and the outer region (with the second metal layer). In the inner region the efficiency reached a maximum of 97% for voltages above 350 V for a mean irradiation of  $9.5 \cdot 10^{14}$  protons/cm<sup>2</sup> and a cluster signal to noise cut of 3. It was still 95% at 300 V but falls rapidly at lower voltages. On the non-irradiated side of the detector the efficiency was  $98.6 \pm 0.3\%$ . In both region the fake cluster rate was 20%.

As expected by the charge loss to the routing lines, the efficiency on the outer region is worse. For the same irradiation as above the efficiency at 300 V is only 75%. Recovering for this charge loss by adding the routing lines to the algorithm could be possible. However the low charge picked up by the routing lines and the ambiguity with respect to the inner region would make it difficult to do.

**Cluster shapes** Figure 5.21 shows the cluster extent for the non-irradiated and irradiated region. The non-irradiated region exhibits a flat distribution while the irradiated region shows a clear dependence of the collected charge on the cluster extent for the three different voltages. This is evidence that in the irradiated region of the detector the resolution would degrade due to the charge not being focused within two strips.

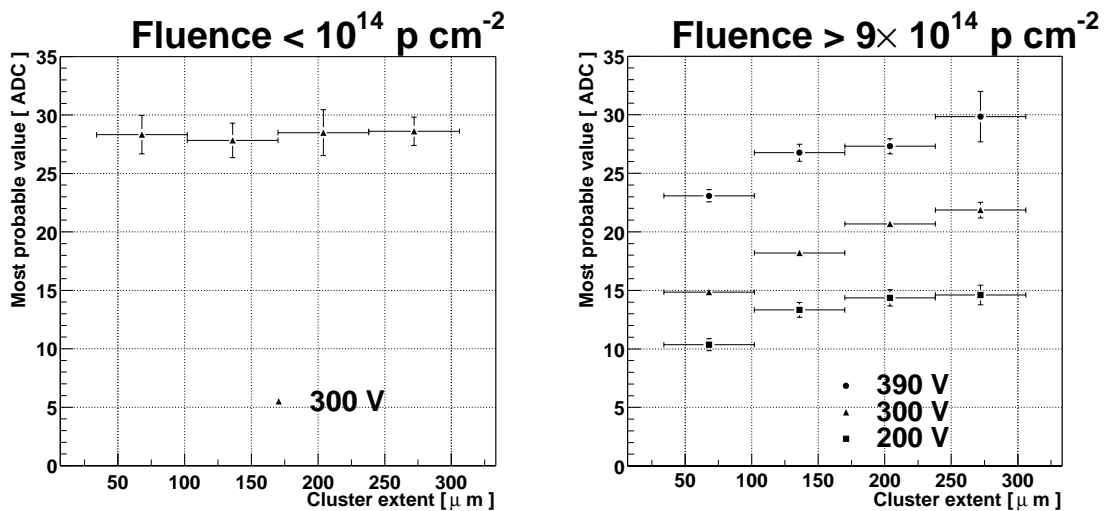


Figure 5.21: *The cluster extent of the Micron detector at different irradiation doses.*

**Signal-to-noise ratio** The maximum value of the signal recorded for the Micron detector when the routing lines are not included was  $27.1 \pm 2.6$  ADC counts and the common mode suppressed noise was 1.76 counts. Hence the measured signal to noise ratio for the fully depleted detector was estimated to be  $15.4 \pm 1.5$ .

The common mode suppressed noise was stable for all voltages in the irradiated side but it started to increase around 350 V for the non-irradiated side and reached 6 ADC counts at 390 V. This is consistent with micro-discharge around the  $p^+$  implants.

**Conclusion** The dangers of under-depleted  $p$ -on- $n$  detectors with double metal layers have been observed. The four main problems encountered with  $p$ -on- $n$  prototype are:

- the loss of charge to the routing lines and the spreading of the charge when underdepleted,
- the possible increase in noise due to micro-discharge in the least irradiated regions when over depleting the irradiated regions of the detector,
- the high depletion voltage for the detector at irradiation less than  $6 \cdot 10^{14}$  protons/cm<sup>2</sup> and
- the CCE is 25% less than expectation.



# Conclusion

The LHCb experiment, in its quest of a better understanding of CP violation, will require the ability to distinguish the production flavour of the B mesons.

This task will be fulfilled by a procedure which combines four (five) different signatures of the  $B^0$  ( $B_s^0$ ) flavour. For the  $B_s^0/\bar{B}_s^0$  it was shown that the  $s/\bar{s}$  quark which is produced together with the one in the  $B_s$  meson can be found in the event after hadronisation into a kaon. For all the B mesons, the muon, electron and/or kaon possibly produced by the decay of the other  $b/\bar{b}$  quark can also be extracted and used for tagging. Finally, it was shown that the sign of the charge of the other b hadron can be estimated by reconstructing a displaced vertex.

It was demonstrated that an effective tagging efficiency of  $6.2\pm 0.7\%$  can be obtained for  $B_s$  mesons and  $4.1\pm 0.6\%$  for the  $B_d$  mesons (averaged over the available data for the various channels studied). Some channel dependencies have been shown (detailed results are available in Table 4.20 on page 72).

The study of multiple interactions showed that the tagging was capable of surviving to the actual rate of such events. An acceptable reduction of the effective tagging efficiency of the order of 10% was observed for all events with respect to single interaction events.

Correlations between the trigger and the tagging have been exhibited. The trigger team is now also using the tagging information for its optimisation procedure.

Before any physics analysis can be done, data must be collected. The collection of these data turns out to be a challenging task for the detector.

In particular, the Vertex Locator will be exposed to a high level of radiation. In addition to this, the large bunch crossing rate imposed by the small production cross-section of the B mesons will require dedicated electronics to read-out the detector. For these reasons a careful choice of the technologies used to build the Vertex Locator of LHCb is very important. The many data collected during the various LHCb VELO testbeams made possible an enlightened decision on the technologies.

The efficiency and resolution of a  $300\ \mu\text{m}$  thick  $n$ -on- $n$  VELO prototype with slow readout electronics was studied. A safe point of operation was determined

to be reached at 90 V with an efficiency very close to 100%. The resolution of the detector was studied as a function of the incident angle and the charge sharing fraction was measured. The results compared favourably with the developed simulation.

The SCT128A, a radiation hard read-out chip designed for LHC speed operation, was tested with success. The measurement of its pulse shape showed that it was possible to limit the overspill to 30% while still collecting 94% of the signal of a heavily irradiated detector.

The test of both the *n-on-n* Hamamatsu prototype [47] and the *p-on-n* MICRON prototype [48] with LHC 40 MHz readout demonstrated that the *n-on-n* design had a better behaviour after irradiation despite its higher noise when compared to the *p-on-n* prototype. The LHCb experiment will thus use *n-on-n* sensors for its Vertex Locator.

# Appendix A

## Statistical error on the effective tagging efficiency

Given the number of correct tags  $r$ , the number of wrong tags  $w$  and the number of untagged event  $u$  such that  $n = r + w + u$  is the total number of events, we have for the tagging efficiency  $\epsilon = \frac{r+w}{n}$  and for the wrong-tag fraction  $\omega = \frac{w}{r+w}$  and thus for the effective tagging efficiency:

$$\epsilon_{\text{eff}} = \epsilon(1 - 2\omega)^2 = \frac{r + w}{n} \left(1 - 2\frac{w}{r + w}\right)^2 = \frac{(r - w)^2}{n(r + w)}$$

The error on  $\epsilon_{\text{eff}}$  can be obtained by assuming that  $r$ ,  $w$  and  $u$  are independent and by propagating the error quadratically. With

$$\sigma_r = \sqrt{r}, \quad \sigma_w = \sqrt{w}, \quad \sigma_u = \sqrt{u} \quad (\text{A.1})$$

we have

$$\sigma_\epsilon = \frac{\sqrt{un(r+w)}}{n^2} \quad (\text{A.2})$$

$$\sigma_\omega = \frac{\sqrt{rw}}{(r+w)^{3/2}} \quad (\text{A.3})$$

$$\sigma_{\epsilon_{\text{eff}}} = (1 - 2\omega) \sqrt{(1 - 2\omega)^2 \sigma_\epsilon^2 + 16\epsilon^2 \sigma_\omega^2} \quad (\text{A.4})$$

It is also possible to compute the error assuming  $n$  is fixed and  $r$ ,  $w$  and  $u$  follow a multinomial distribution. That way

$$\sigma_r = \sqrt{r \left(1 - \frac{r}{n}\right)}, \quad \sigma_w = \sqrt{w \left(1 - \frac{w}{n}\right)}, \quad \text{cov}_{r,w} = \sqrt{\frac{rw}{n}} \quad (\text{A.5})$$

and

$$\sigma_{\epsilon_{\text{eff}}} = \sqrt{\left(\frac{\partial \epsilon_{\text{eff}}}{\partial r}\right)^2 \sigma_r^2 + \left(\frac{\partial \epsilon_{\text{eff}}}{\partial w}\right)^2 \sigma_w^2 - 2 \left(\frac{\partial \epsilon_{\text{eff}}}{\partial r}\right) \left(\frac{\partial \epsilon_{\text{eff}}}{\partial w}\right) \text{cov}_{r,w}^2} \quad (\text{A.6})$$

$$= \frac{(1 - 2\omega)}{n} \sqrt{\frac{r^2 + 14rw + w^2}{r + w} - \epsilon_{\text{eff}}(r + w)} \quad (\text{A.7})$$

However, the two approaches give identical results once fully developed.



# Bibliography

- [1] The Particle Data Group of Lawrence Berkeley National Laboratory. The Particle Adventure. <http://particleadventure.org/>.
- [2] R. Antunes Nobrega et al. *Reoptimized Detector Design and Performance*. CERN, Genève, 2003. CERN/LHCC/2003-030.
- [3] Jan Kaplon <jan.kaplon@cern.ch>. SCTA128LC & SCTA128HC version 0.1, April 1998.
- [4] Paolo Bartalini et al. Measurements of the Signal Shape of a Silicon Strip Detector with SCTA Readout. LHCb-VELO 2000-098, October 2000.
- [5] K. Hagiwara et al. Review of Particle Physics. *Physical Review D*, 66:010001, 2002.
- [6] Elliot Leader and Enrico Predazzi. *An introduction to gauge theories and modern particle physics*, volume 3 and 4 of *Monographs on Particle Physics, Nuclear Physics and Cosmology*. Cambridge University Press, Cambridge, UK, 1996. ISBN 0 521 46840 X a,d ISBN 0 521 49951 8.
- [7] CERN Public web pages. <http://www.cern.ch>.
- [8] CERN Document Server. <http://cdsweb.cern.ch>.
- [9] The Large Hadron Collider Project. [http://lhc.web.cern.ch/lhc/general/gen\\_info.htm](http://lhc.web.cern.ch/lhc/general/gen_info.htm).
- [10] Alison Wright et al. LHCb Public Home Page. <http://lhcb-public.web.cern.ch/lhcb-public/default.htm>.
- [11] Gustavo C. Branco, Luís Lavoura and João P. Silva. *CP Violation*. The International Series of Monographs on Physics. Oxford University Press, Oxford, UK, 1999. ISBN 0 19 850399 7.

- [12] Ikaros I. Bigi and A. Ichiro Sanda. *CP violation*, volume 9 of *Monographs on Particle Physics, Nuclear Physics and Cosmology*. Cambridge University Press, Cambridge, UK, 2000. ISBN 0 521 44349 0.
- [13] Tatsuya Nakada. Physics of CP Violation and Rare Decays, 3rd Cycle Lecture. <http://nakada.home.cern.ch/nakada/lectures.htm>, 2001.
- [14] A. Abashian and others. Measurement of the CP violation parameter  $\sin 2\phi_1$  in  $B^0$  meson decays. *Phys. Rev. Lett.*, 86:2509–2514, 2001.
- [15] B. Aubert et al. Measurement of CP violating asymmetries in  $B^0$  decays to CP eigenstates. *Phys. Rev. Lett.*, 86:2515–2522, 2001.
- [16] K. Abe et al. Observation of large CP violation in the neutral B meson system. *Phys. Rev. Lett.*, 87:091802, 2001.
- [17] S.L. Glashow. Partial Symmetries of Weak Interactions. *Nucl. Phys.*, 22:579–588, 1961.
- [18] Steven Weinberg. A model of leptons. *Physical Review Letter*, 19:1264–1266, 1967.
- [19] Abdus Salam and R. Delbourgo and J. Strathdee. Weak and Electromagnetic Interactions. In N. Svartholm, editor, *Elementary Particle Theory, Proceedings Of The Nobel Symposium Held 1968 at Lerum, Sweden, Stockholm 1968*, pages 367–377. Almquist and Wiksells, Stockholm, 1968.
- [20] P.W. Higgs. Broken symmetries and the masses of gauge bosons. *Phys. Rev. Lett.*, 13:508, 1964.
- [21] Makoto Kobayashi and Toshihide Maskawa. CP violation in the renormalizable theory of weak interaction. *Prog. Theor. Phys.*, 49:652, 1973.
- [22] Nicola Cabibbo. Unitary Symmetry and Leptonic Decays. *Phys. Rev. Lett.*, 10:531–532, 1963.
- [23] S. L. Glashow and J. Iliopoulos and L. Maiani. Weak Interactions with Lepton – Hadron Symmetry. *Phys. Rev.*, D2:1285–1292, 1970.
- [24] Wolfenstein, Lincoln. Parametrization of the Kobayashi-Maskawa matrix. *Phys. Rev. Lett.*, 51:1945, 1983.
- [25] Patricia Ball et al. B decays at the LHC. In G. Altarelli and M.L. Mangano, editor, *Proceedings of the 1999 Workshop on Standard Model Physics (and more) at the LHC*, volume CERN 2000-004. CERN Organisation européenne pour la recherche nucléaire, 1999.

- [26] P.R. Barbosa Marinho et al. *LHCb VELO Technical Design Report*. CERN, Genève, 2001. CERN/LHCC/2001-0011.
- [27] S. Amato et al. *LHCb RICH Technical Design Report*. CERN, Genève, 2000. CERN/LHCC/2000-0037.
- [28] S. Amato et al. *LHCb Magnet Technical Design Report*. CERN, Genève, 1999. CERN/LHCC/2000-007.
- [29] P.R. Barbosa Marinho et al. *LHCb Outer Tracker Technical Design Report*. CERN, Genève, 2001. CERN/LHCC/2001-024.
- [30] A. Franca Barbosa et al. *LHCb Inner Tracker Technical Design Report*. CERN, Genève, 2002. CERN/LHCC/2002-029.
- [31] S. Amato et al. *LHCb Calorimeters Technical Design Report*. CERN, Genève, 2000. CERN/LHCC/2000-0036.
- [32] P.R. Barbosa Marinho et al. *LHCb Muon System Technical Design Report*. CERN, Genève, 2001. CERN/LHCC/2001-010.
- [33] R. Antunes Nobrega et al. *LHCb Trigger System Technical Design Report*. CERN, Genève, 2003. CERN/LHCC/2003-031.
- [34] M. Cattaneo et al. The GAUDI project. <http://proj-gaudi.web.cern.ch/proj-gaudi/>.
- [35] Torbjörn Sjöstrand. High-energy physics event generation with PYTHIA 5.7 and JETSET 7.4. *Comput. Phys. Commun.*, 82:74–90, 1994.
- [36] QQ — The CLEO Event Generator. <http://www.lns.cornell.edu/public/CLEO/soft/QQ>.
- [37] CERN. GEANT— Detector description and Simulation Tool. CERN Program Library Long Writeup W5013.
- [38] M. Cattaneo et al. Brunel - The LHCb Reconstruction Program. <http://lhcb-comp.web.cern.ch/lhcb-comp/Reconstruction/default.htm>.
- [39] Gloria Corti et al. DaVinci - The LHCb Analysis Program. <http://lhcb-comp.web.cern.ch/lhcb-comp/Analysis/default.htm>.
- [40] The technique used for combining different particle IDs. <http://lhcb-comp.web.cern.ch/lhcb-comp/Analysis/DaVinci/v8/combine.htm>.

- [41] Roger Forty. More info on the Particle ID. [http://lhcb-comp.web.cern.ch/lhcb-comp/Analysis/DaVinci/v8/ParticleID\\_M%oreInfo.htm](http://lhcb-comp.web.cern.ch/lhcb-comp/Analysis/DaVinci/v8/ParticleID_M%oreInfo.htm).
- [42] Marta Calvi, Olivier Dormond and Marco Musy. LHCb Flavour Tagging Performance. LHCb 2003-115, September 2003.
- [43] Paolo Bartalini et al. VELO telescope resolution and efficiency measurements. LHCb-VELO 2000-099, October 2000.
- [44] CERN ECP Division FEX Group Cascade Section. *CASCADE User's Guide*. CERN, Genève, March 1997. CERN ECP/FEX-CA 97-1.
- [45] F. Anghinoffi et al. SCTA – A Rad-Hard BiCMOS Analogue Readout ASIC for the ATLAS Semiconductor Tracker.
- [46] Ian Tomalin. Alignment of the 1998 VELO Test Beam Data. LHCb 99-032 VELO, August 1999.
- [47] Themis Bowcock et al. Performance of an irradiated  $n$ -on- $n$  Hamamatsu prototype VELO detector. LHCb 2001-039 VELO, May 2001.
- [48] Themis Bowcock et al. Performance of an irradiated  $p$ -on- $n$  MICRON prototype VELO detector. LHCb 2001-040 VELO, May 2001.
- [49] Vertex Locator Test Beam Group. Track Fit – Vertex Locator Test-Beam Software Description. LHCb 2001-038 VELO, June 2001.
- [50] Victoria Wright et al. Study of Resolution of VELO Test-Beam Telescope. LHCb-VELO 2000-103, November 2000.
- [51] K. Borer et al. Charge collection efficiency and resolution of an irradiated double-sided silicon microstrip detector operated at cryogenic temperatures, 2000.
- [52] K. Borer et al. Charge Collection Efficiency and Resolution of an Irradiated Double Sided Silicon Microstrip Detector Operated at Cryogenic Temperatures. LHCb 99-026 VELO, July 1999.
- [53] P.R. Barbosa Marinho et al. *LHCb Online System Data Acquisition & Experiment Control Technical Design Report*. CERN, Genève, 2001. CERN/LHCC/2001-40.
- [54] S. Amato and al. *LHCb Technical Proposal*. CERN, Genève, 1998. CERN-LHCC-98-4.

- [55] K. Kirsebom et al. *LHC-B Letter of Intent*. CERN, Genève, 1995. CERN-LHCC-95-5.
- [56] STDHEP — A common output format for Monte Carlo events. <http://www-pat.fnal.gov/stdhep.html>.
- [57] Patrick Koppenburg. *Contribution to the Development of the LHCb Vertex Locator and Study of Rare Semileptonic Decays*. PhD thesis, Université de Lausanne, 2002.
- [58] Stefania Saladino. *Study of Vertex Silicon Detector For LHC Experiments*. Dottorato di ricerca in fisica, Università degli Studi di Bari, 1999.